Lappeenranta
University of Technology

Matti Lahti

ATOMIC LEVEL PHENOMENA ON TRANSITION METAL SURFACES

Thesis for the degree of Doctor of Science (Technology) to be presented with due permission for public examination and criticism in the Auditorium of the Student Union House at Lappeenranta University of Technology, Lappeenranta, Finland on the 26th of August, 2011 at noon.

Acta Universitatis
Lappeenrantaensis 441

Supervisor Professor Matti Alatalo
Department of Mathematics and Physics
Lappeenranta University of Technology
Lappeenranta, Finland

Reviewers Professor Martti Puska
Department of Applied Physics
Aalto University School of Science and Technology
Espoo, Finland

Professor Kalevi Kokko
Department of Physics and Astronomy
University of Turku
Turku, Finland

Opponent Docent Karoliina Honkala
Department of Chemistry
University of Jyväskylä
Jyväskylä, Finland

ISBN 978-952-265-121-1
ISBN 978-952-265-122-8 (PDF)
ISSN 1456-4491

Lappeenrannan teknillinen yliopisto
Digipaino

Abstract

Matti Lahti
Atomic level phenomena on transition metal surfaces
Lappeenranta 2011
64 p.
Acta Universitatis Lappeenrantaensis 441
Diss. Lappeenranta University of Technology
ISBN 978-952-265-121-1, ISBN 978-952-265-122-8 (PDF), ISSN 1456-4491

In this study we discuss the atomic level phenomena on transition metal surfaces. Transition metals are widely used as catalysts in industry. Therefore, reactions occuring on transition metal surfaces have large industrial intrest. This study addresses problems in very small size and time scales, which is an important part in the overall understanding of these phenomena. The publications of this study can be roughly divided into two categories: The adsorption of an O_2 molecule to a surface, and surface structures of preadsorbed atoms. These two categories complement each other, because in the realistic case there are always some preadsorbed atoms at the catalytically active surfaces. However, all transition metals have an active d-band, and this study is also a study of the influence of the active d-band on other atoms.

At the first part of this study we discuss the adsorption and dissociation of an O_2 molecule on a clean stepped palladium surface and a smooth palladium surface precovered with sulphur and oxygen atoms. We show how the reactivity of the surface against the oxygen molecule varies due to the geometry of the surface and preadsorbed atoms. We also show how the molecular orbitals of the oxygen molecule evolve when it approaches the different sites on the surface. In the second part we discuss the surface structures of transition metal surfaces. We study the structures that are intresting on account of the Rashba effect and charge density waves. We also study the adsorption of suphur on a gold surface, and surface structures of it. In this study we use *ab-initio* based density functional theory methods to simulate the results. We also compare the results of our methods to the results obtained with the Low-Energy-Electron-Difraction method.

Keywords: *surface physics, adsorption, oxidation, metal surfaces, surface structures*
UDC 539.23:539.211:544.723

Preface

This thesis was prepared at Lappeenranta University of Technology, Department of Mathematics and physics, Laboratory of Applied Mathematics, under the guidance of Prof. Matti Alatalo during years 2006-2011.

I would like to thank my supervisor Matti Alatalo for the opportunity to work at the University, and for his attitude to encourage artistic and scientific thinking. I would also particularly like to thank two very important persons: Antti Puisto and Katariina Pussi. Without them this thesis would have never been completed. Antti assisted me to start using the sofware needed, and was crucial partner in the first publications. All recent publications are made in collaboration with Katariina. She has also given a lot of scientific guidance and help with this thesis. Many thanks also to Heikki Pitkänen for checking the language of this thesis, and for many absorbing discussions.

I would like to thank all my colleagues, who have worked in our group. I thank all of you guys for the scientific discussion during coffee breaks. Nelli and Arto I would like to thank for collaborative publications. Sami I would like to thank for personal collaboration.

I acknowledge the rewiewers Professor Martti Puska and Professor Kalevi Kokko for their comments. I am grateful for Docent Karoliina Honkala for her efforts as the opponent.

The work is supported by the National Graduate School in Materials Physics. I would like to thank CSC – IT Centre for Sciences Ltd. for computational resources.

Lappeenranta, August 2011

Matti Lahti

List of Publications

This thesis consists of an overview and the following publications

I M. Lahti, N. Nivalainen, A. Puisto, M. Alatalo, O_2 dissociation on Pd(211) and Cu(211) surfaces, Surface Science 601, 3774 (2007).

II M. Lahti, A. Puisto, M. Alatalo, T.S. Rahman, The role of preadsorbed sulphur and oxygen in O_2 dissociation on Pd(100), Surface Science 602, 3660 (2008).

III M. Lahti, K. Pussi, M. Alatalo, S.A. Krasnikov, A.A. Cafolla, Sulphur adsorption on Au{110}: DFT and LEED study, Surface Science 604, 797 (2010).

IV I.M McLeod, V.R Dhanak, A. Matilainen, M. Lahti, K. Pussi, K.H.L. Zhang, Structure determination of p($\sqrt{3} \times \sqrt{3}$)R30° Bi-Ag(111) surface alloy using LEED I-V and DFT analyses, Surface Science 604, 1395 (2010).

V K.H.L. Zhang, I.M McLeod, Y.H. Lu, V.R. Dhanak, A. Matilainen, M. Lahti, K.Pussi, R.G. Egdell, X.-S. Wang, A.T.S. Wee and W. Cheng, Observation of a surface alloying to de-alloying transition during growth of Bi on Ag(111), Physical Review B 83, 235418 (2011).

VI I.M. McLeod, V.R Dhanak, A. Matilainen, M. Lahti, K. Pussi, K.H.L. Zhang, LEED I-V and DFT Structure determination of p($\sqrt{3} \times \sqrt{3}$)R30° Pb-Ag(111) surface alloy, Journal of Physics: Condensed Matter. 23, 265006 (2011).

VII M. Lahti, K. Pussi, E. McLoughlin, A.A. Cafolla, The structure of Cu{100}-p(2×6)-2mg-Sn studied by DFT and LEED, Surface Science 605, 1000 (2011).

Author's contribution. In Publication I the author has performed most of the simulations. In Publication II the author has performed all simulations, and in publications III-VII the author has performed all DFT simulations. The author has actively participated in the writing of Publications I-IV and VI, VII.

Abbreviations

a_o	Bohr radius
DFT	Density Functional Theory
DOS	Density Of States
E	Energy
e	Elementary charge
FCC	Face Centered Cubic
GGA	Generalized Gradient Approximation
ϵ_i	Energy eigenvalue
ϵ_{xc}	Exchange correlation energy per electron
$\hat{H}$	Hamiltonian operator
$\hbar$	Planck constatnt
LCAO	linear combination of atomic orbitals
LDA	local density approximation
LEED	Low-Energy-Electron-Difraction
m	mass
PES	Potential energy surface
r	distance
SIESTA	Spanish initiative for Electronic Simulations with Thousands of Atoms
T	kinetic energy
V	potential field
VASP	Vienna $Ab-initio$ Simulation Package
PAW	Projector Augmented Wave
ε_0	Vacuum permittivity
ψ_i	Wave function
Ψ	Manybody wave function
ϕ_x	Atomic orbital
ϕ	Molecular orbital
∇	Differential operator

Contents

Chapter 1

Introduction

Understanding of the atomic level phenomena occuring on surfaces is considered as one of the most important parts of physics of the past few decades. Previously, research was often performed only for academic interest. However, those results are nowdays found useful for the development of technological applications. In many sectors technology has reached a level where developing it further demands for knowledge of atomic level phenomena. On the other hand, developing more environmental friendly technology is today a great challenge to scientists and engineers. In many cases replacing old tecnology with new, more environmentally friendly technology demands for a new way of thinking. Atomic level phenomena have a lot of potential for solving the old problems in a new way. However, research of those phenomena is very challenging, not only for technolocical reasons. It also tests the ability of the researcher to think in a different way than one would think when addressing problems in human size scale. Quantum mechanics is the tool for understanding and studying atomic size problems. Using the theories of quantum mechanics one can calculate the behaviour of atoms.

Several intresting atomic size phenomena occur at the surface or near the surface of metals. Surface science is a meeting ground of physics, chemistry and engineering. The theoretical tools come from physics, but the questions that are asked are very chemical: What is the structure of the surface, how it affects, e.g., a molecule on the surface and how we can change it. Of course the main goal is often somewhere in the engineering science, and the engineering sciences are the ones that bring us actual technological applications. The phenomena are small, fast and theoretically complicated. It is impossible to get results only with a pen and paper. A surface scientist needs a very accurate and elegant instrument for experiments and /or a very fast computer for theoretical work. In many cases it is impossible to find a reliable solution to an atomic level problem only using one method to study it. That is why the comparison of results that are acquired using different methods gives an opportunity to reach better results.

The study of adsorption is of central importance in the field of surface science. Adsorption processes are involved in almost all technical processes that involve surfaces. Oxygen molecules are everywhere around us, and oxygen is one of the most reactive elements in our atmosphere. So the wanted or unwanted adsorption of oxygen is one of the most important and common adsorption processes. To discover a way to control it is one the most important parts of surface science. On the other hand, many chemical reactions that involve oxygen and some other compound on a metal surface start with the dissociation of the oxygen molecule. In many applications the dissociation occurs on the surface of a catalyst metal. Also the oxidation of metallic surfaces starts with the dissociation of the molecule. There exists a lot of research of this process on many metallic surfaces, but there are still several unknown issues on the way to the complete understanding of the dissociation of oxygen molecule on metallic surfaces. The computational study is the best way to research the dynamics of the reactions, because the reactions occur too rapidly on the time scale for the experimental study. Ideally, a good catalyst should have strong reactivity toward dissociation of the oxygen molecule and a weak binding capacity toward an oxygen atom. So the reaction makes the atoms available for other reactions. However many metallic surfaces build up an oxide film upon the surface. After its formation, this film slows down the dissociation processes.

The results presented in this thesis are calculated using quantum mechanics based *ab initio* software packages. Some of the results are also compared with Low-Energy-Electron-Difraction (LEED) calculations that are carried out by my collaborators. The publications of this study can be roughly divided to two parts: the adsorption of the oxygen molecule to a surface and surface structures of preadsobed atoms. As we construed before, both of the phenona complement each other. In Chapter 3 we also state some new aspects of the results of the publications of this study.

Chapter 2

Theory

2.1 Introduction to quantum mechanics

In quantum mechanics the starting point for solving any system is usually the time-independent Schrödinger equation. It is frequently written in the very compact form,

$$\hat{H}\Psi = E\Psi, \tag{2.1}$$

where $\hat{H}$ represents the Hamiltonian operator, and E is the total energy of the system. The function Ψ is called the eigenfunction of $\hat{H}$ corresponding to the eigenvalue E. The Hamiltonian for the single particle can be written as

$$\hat{H} = -\frac{\hbar^2}{2m} \bigtriangledown^2 + V(\mathbf{r}), \tag{2.2}$$

where m represents the mass of the particle, and $V(\mathrm{r})$ represents a potential field. For a system of nuclei and electrons the Hamiltonian can be described by a well-defined form

$$H = T_{\text{nucl}} + T_{\text{el}} + V_{\text{nucl}-\text{nucl}} + V_{\text{nucl}-\text{el}} + V_{\text{el}-\text{el}}, \tag{2.3}$$

where T_{nucl} and T_{el} are the kinetic energy terms of nuclei and electrons, $V_{\text{nucl}-\text{nucl}}$ and $V_{\text{el}-\text{el}}$ are the Coulombic repulsion terms between nuclei and between electrons, and $V_{\text{nucl}-\text{el}}$ is the Coulombic attraction term between nuclei and electrons. This representation neglects the effect of spin. When we try to solve a system with electrons and nuclei, some approximations are needed. One of the basic level approximations is the Born-Oppenheimer approximation [1]. It is based on the fact that the nuclei are much more massive than the electrons ($M/m_e \gg 10^3$). Because of this difference, the electrons can respond almost instantaneosly to displacement of the nuclei. Therefore it is possible to fix the nuclei in their positions, and solve the Schrödinger equation for the electrons in the static electronic potential. The positions of the nuclei can then be modified, and the Hamiltonian for the electrons can be solved again.

Now we can define the electronic hamiltonian H_{el} for fixed nuclear coordinates $\{\mathbf{R}\}$ as follows

$$H_{\mathrm{el}}(\{\mathbf{R}\}) = T_{\mathrm{el}} + V_{\mathrm{nucl-nucl}} + V_{\mathrm{nucl-el}} + V_{\mathrm{el-el}}, \tag{2.4}$$

The Schrödinger equation for the electrons for a given fixed configuration of the nuclei is then

$$H_{\mathrm{el}}(\{\mathbf{R}\})\Psi(\mathbf{r}, \{\mathbf{R}\}) = E_{el}(\{\mathbf{R}\})\Psi(\mathbf{r}, \{\mathbf{R}\}). \tag{2.5}$$

The nuclei are assumed to move according to the atomic Schrödinger equation

$$\{T_{\mathrm{nucl}} + E_{\mathrm{el}}(\mathbf{R})\}\Lambda(\mathbf{R}) = E_{\mathrm{nucl}}\Lambda(\mathbf{R}). \tag{2.6}$$

Often the quantum effects in atomic motion are neglected and the classical equation of motion are solved for the atomic motion

$$M_{\mathrm{I}}\frac{\partial^2}{\partial t^2}\mathbf{R}_{\mathrm{I}} = -\frac{\partial}{\partial \mathbf{R}_{\mathrm{I}}}E_{\mathrm{el}}(\{\mathbf{R}\}). \tag{2.7}$$

We can evalute the force acting on atoms by using the Helmann-Feynman theorem [2][3]

$$F_{\mathrm{I}} = -\frac{\partial}{\partial \mathbf{R}_{\mathrm{I}}}E_{\mathrm{el}}(\{\mathbf{R}\}) = \langle\Psi(\mathbf{r}, \{\mathbf{R}\})|\frac{\partial}{\partial \mathbf{R}_{\mathrm{I}}}H_{el}(\{\mathbf{R}\})|\Psi(\mathbf{r}, \{\mathbf{R}\})\rangle. \tag{2.8}$$

Now we can express the data obtained from the calculation in many ways depending on the case. For example, in the case of a molecule consisting of two atoms we can plot the total energy of the system versus the bond length. From this curve we can easily see the optimum bond lenght (the point lowest in energy). Next we have to consider how we can find a solution to the function Ψ. Let us start from the easiest case.

$$\hat{H} = -\frac{\hbar^2}{2m}\bigtriangledown^2 \tag{2.9}$$

is the Hamiltonian of a free particle. Constraining the particle to move in one dimension, the time independent Schrödinger equation becomes

$$-\frac{\hbar^2}{2m}\frac{\partial^2}{\partial x^2}\psi = E\psi \tag{2.10}$$

or

$$-\frac{\partial^2\psi}{\partial x^2} + \frac{2mE\psi}{\hbar^2} = 0. \tag{2.11}$$

There are two solutions to this differential equation, namely

$$\psi_1 = A\mathrm{e}^{\mathrm{i}\sqrt{2mE}x/\hbar} \tag{2.12}$$

and

$$\psi_2 = A\mathrm{e}^{-\mathrm{i}\sqrt{2mE}x/\hbar}. \tag{2.13}$$

2.2 Bonds

In order to understand the structures of molecules and solid state materials, one has to know the basic theory of atomic bonding. There are five primary types of bonds:

1. Van der Waals attraction leads to weak bonds between atoms, between molecules or between molecules and solids. It is typical on rare gases, which can compose bulk-like structures via the van der Waals bonds.

2. Ionic bond. A crystal can be composed of atoms with a large difference in electronegativity. In this case, the electrons transfer from one atom to another and thus positive and negative ions are formed. The Coulomb attraction keeps the atoms together. Nevertheless it is not possible to identify charges uniquely associated with ions. There are no free electrons in an ionic crystal and therefore it is an insulator with an energy gap.

3. In metallic systems the bonds are formed by a homogeneous electron gas between ions. Metallic solids have no energy gap for electronic excitation when the bands are partially filled. This is why metal atoms can easily accept different number of electrons, leading to the ability to form alloys among atoms with different valency. This is also the reason why metals can adopt close packed structures. Because of the electron gas, metals are good conductors.

4. In covalent bonding the orbitals of an atom are mixed with those belonging to the atoms next to it. The atoms compose common orbitals and share electrons.

5. Hydrogen bonding is a very weak type of bonding. Hydrogen is a special case, because it is the only chemically active element with no core electrons. For example, in the case of the water molecule, the hydrogen atoms share their only electron with the oxygen atom. Then the hydrogen end of the water molecule becomes more electronically positive than the side of the oxygen atom. So the hydrogen end of the molecule and the oxygen end of the molecule form dipole-dipole attraction.

The bonding in real materials is often a combination of some of the above mentioned bond types.

2.3 Short theory of molecular structure

In this chapter we discuss briefly the covalent bonding in a quantum mechanical way. If one cannot understand the forces that keep atoms together in molecules, one cannot understand why surfaces can cause the dissociation of molecules. This is why it is important to obtain a simple model which explains the nature of the chemical bonds. In this chapter we construct a very simple model and discuss what we can learn from it. Later we shall adapt some parts of it in order to explain bonds between a molecule and a surface. Let us take the easiest example: The positive hydrogen molecule ion, which consists of two protons and one electron. Unfortunately we can not solve it analytically before we do some approximations. Three moving particles and interactions between them is too hard a problem to be solved analytically. To overcome this difficulty we adopt the Born-Oppenheimer approximation [1]. This approximation takes advantage of the great difference of the masses between electrons and protons, which allows us to solve the Hamiltonian by using fixed nuclei. Now the Hamiltonian for the problem is

$$H = -\frac{\hbar}{2m_e} \bigtriangledown^2 + V(\mathbf{x}\mathbf{X_1}\mathbf{X_2}), \tag{2.14}$$

where $V(\mathbf{x}\mathbf{X_1}\mathbf{X_2})$ is the potential energy, $\mathbf{x}$ is the location of the electron, and $\mathbf{X_1}$, $\mathbf{X_2}$ are the locations of the two nuclei. In this case the potential energy can be written as

$$V(\mathbf{x}\mathbf{X_1}\mathbf{X_2}) = -\frac{e^2}{4\pi\varepsilon_0 \mathbf{r}_A} - \frac{e^2}{4\pi\varepsilon_0 \mathbf{r}_B} + \frac{e^2}{4\pi\varepsilon_0 \mathbf{R}}, \tag{2.15}$$

where r_A is the distance from the electron to the nucleus A, r_B is the distance from the electron to the nucleus B and R is the distance between the nuclei. So the final term represents the repulsive interaction between the two nuclei. The first and the second term represent attraction between the electron and the nuclei, which is the force that keeps the molecule together. The Schödinger equation is

$$H\Psi = E\Psi. \tag{2.16}$$

The energy of the system can be solved the hard way in elliptical coordinates, but we use another method that explains more about the physics of the system and wave functions. At the beginning we introduce ground state wave functions of the electron bound to one or the other of the protons. If we locate the nuclei to the points R/2 , -R/2 and the electron to the point r=0, we can write

$$\phi_1(\mathbf{r}, \mathbf{R}) = (\frac{1}{\pi a_0^3})^{1/2} \mathrm{e}^{-|\mathbf{r}-\mathbf{R}/2|/a_0} \tag{2.17}$$

and

$$\phi_2(\mathbf{r},\mathbf{R}) = (\frac{1}{\pi a_0^3})^{1/2}\mathrm{e}^{-|\mathbf{r}+\mathbf{R}/2|/a_0}. \tag{2.18}$$

As we have the wave functions, we can form a combination ϕ, by the theory of linear combination of atomic orbitals (LCAO) [4]:

$$\phi = \sum_{\mathbf{r}} c_{\mathbf{r}}\phi_{\mathbf{r}}, \tag{2.19}$$

In order to find the optimum values of the coefficients we have to solve the secular equations:

$$\sum_{\mathbf{r}} c_{\mathbf{r}}(H_{\mathbf{r}s} - ES_{\mathbf{r}s})\Phi_{\mathbf{r}} = 0, \tag{2.20}$$

where $H_{\mathbf{r}s}$ is a matrix element of the Hamiltonian and $S_{\mathbf{r}s}$ is an overlap matrix element. These secular equations have non-trivial solutions if

$$\det|H_{\mathbf{r}s} - ES_{\mathbf{r}s}| = 0. \tag{2.21}$$

Now we need to choose a basis to represent the situation. To make the example easier we choose that only the 1s orbitals represent the hydrogen atoms. In this case the basis is sufficiently good. In this case the linear combination is a combination of the $1s_A$ and $1s_B$ orbitals. In order to make progress with finding the roots of the secular determinant, we need to evaluate the relevant matrix elements. We shall use the following notations and values:

$$S_{AA} = S_{BB} = 1, \tag{2.22}$$

$$S_{AB} = S_{BA} = S, \tag{2.23}$$

$$H_{AA} = H_{BB} = \alpha, \tag{2.24}$$

and

$$H_{AB} = H_{BA} = \beta. \tag{2.25}$$

Above S is the overlap integral

$$S = \langle\phi_1|\phi_2\rangle, \tag{2.26}$$

α is the molecular Coulomb integral

$$\alpha = \langle\phi_1|H|\phi_1\rangle, \tag{2.27}$$

and β is the resonance integral

$$\beta = \langle\phi_1|H|\phi_2\rangle. \tag{2.28}$$

The secular determinant then becomes

$$\begin{vmatrix} \alpha - E & \beta - ES \\ \beta - ES & \alpha - E \end{vmatrix} = 0.$$

The roots of this equation are

$$E_{\pm} = \frac{\alpha \pm \beta}{1 \pm S}. \tag{2.29}$$

Now we can solve the integrals by using the ellipsoidial coordinates:

$$S(\mathbf{R}) = \iiint \phi_1(\mathbf{r}, \mathbf{R})\phi_2(\mathbf{r}, \mathbf{R})\mathrm{d}^3\mathbf{r} = \frac{1}{\pi a_0^3} \iiint \mathrm{e}^{-|\mathbf{r}-\mathbf{R}/2|/a_0}\mathrm{e}^{-|\mathbf{r}+\mathbf{R}/2|/a_0}\mathrm{d}^3\mathbf{r}$$

$$= (1 + \frac{\mathbf{R}}{a_0} + \frac{\mathbf{R}^2}{3a_0^2})\mathrm{e}^{-\mathbf{R}/a_0}, \tag{2.30}$$

and

$$\alpha = \iiint \phi_1^*(\mathbf{r}, \mathbf{R})$$

$$\times (\frac{\hbar}{2m_e} \bigtriangledown^2 - \frac{e^2}{4\pi\varepsilon_0|\mathbf{r} - \mathbf{R}/2|} - \frac{e^2}{4\pi\varepsilon_0|\mathbf{r} + \mathbf{R}/2|} + \frac{e^2}{4\pi\varepsilon_0\mathbf{R}})\phi_1(\mathbf{r}, \mathbf{R})\mathrm{d}^3\mathbf{r}$$

$$= E_1 + \frac{e^2}{4\pi\varepsilon_0} \iiint \frac{|\psi_1(\mathbf{r}, \mathbf{R})|^2}{|\mathbf{r} + \mathbf{R}/2|}\mathrm{d}^3\mathbf{r} + \frac{e^2}{4\pi\varepsilon_0\mathbf{R}}. \tag{2.31}$$

Here the term E_1 is the energy of a single hydrogen atom and the last term is the proton-proton repulsion. So the integral can be evaluated:

$$\alpha = E_1 + \frac{e^2}{4\pi\varepsilon_0\mathbf{R}}(1 - (1 + \frac{\mathbf{R}}{a_0})\mathrm{e}^{-2\mathbf{R}/a_0}). \tag{2.32}$$

Similarily we find that:

$$\beta = \iiint \phi_1^*(\mathbf{r},\mathbf{R})(E_1 - \frac{e^2}{4\pi\varepsilon_0|\mathbf{r}+\mathbf{R}/2|} + \frac{e^2}{4\pi\varepsilon_0\mathbf{R}})\phi_2(\mathbf{r},\mathbf{R})\mathrm{d}^3\mathbf{r}$$

$$= E_1 \iiint \phi_1^*(\mathbf{r},\mathbf{R})\phi_2(\mathbf{r},\mathbf{R})\mathrm{d}^3\mathbf{r} + \frac{e^2}{4\pi\varepsilon_0\mathbf{R}} \iiint \phi_1^*(\mathbf{r},\mathbf{R})\phi_2(\mathbf{r},\mathbf{R})\mathrm{d}^3\mathbf{r}$$

$$+ \frac{e^2}{4\pi\varepsilon_0 R} - \frac{e^2}{4\pi\varepsilon_0} \iiint \frac{|\phi_1^*(\mathbf{r},\mathbf{R})\phi_2(\mathbf{r},\mathbf{R})|}{|\mathbf{r}+\mathbf{R}/2|}\mathrm{d}^3\mathbf{r}$$

$$= (E_1 + \frac{e^2}{4\pi\varepsilon_0\mathbf{R}})S(\mathbf{R}) - \frac{e^2}{4\pi\varepsilon_0 a_0}(1+\frac{\mathbf{R}}{a_0})\mathrm{e}^{-\mathbf{R}/a_0}. \tag{2.33}$$

Now we can substitute the solved integrals to the equation of the total energy, and write both of the roots in a more clean way:

$$E_+ = E_1 + \frac{e^2}{4\pi\varepsilon_0\mathbf{R}} - \frac{j+k}{1+S} \tag{2.34}$$

$$E_- = E_1 + \frac{e^2}{4\pi\varepsilon_0\mathbf{R}} + \frac{j-k}{1-S}, \tag{2.35}$$

where

$$j = \frac{e^2}{4\pi\varepsilon_0\mathbf{R}}(1-(1+\frac{\mathbf{R}}{a_0})\mathrm{e}^{-2\mathbf{R}/a_0})) \tag{2.36}$$

$$k = \frac{e^2}{4\pi\varepsilon_0 a_0}((1+\frac{\mathbf{R}}{a_0})\mathrm{e}^{-\mathbf{R}/a_0}). \tag{2.37}$$

Now we can clearly observe that the repulsion between the nuclei has an effect on all cases. The energy curves of both cases are printed in Fig. 2.1. From the figure we can also see the repulsion energy of the protons and the binding energy of the electron, when it is on the bonding state. This model is quite poor, and it can not be used as a starting point of a real calculation, but in this case it yields to information on the true phenomena that occur inside the molecule. From this model we can clearly see, that the combination of the orbitals produce two different electronic states. In the figure the y-axis represents the energy of the separated hydrogen atom and the hydrogen ion. When the curve is beneath the x-axis the H_2 ion is energetically more favourable than the separated parts. In this case the electron composes a molecular state and the protons bind together. Also from Fig. 2.1 we can see that if the electron is on the other state the separated parts are more energetically favourable. Due to the influence of repulsion of the protons the antibonding state is more repulsive than the bonding state is binding.

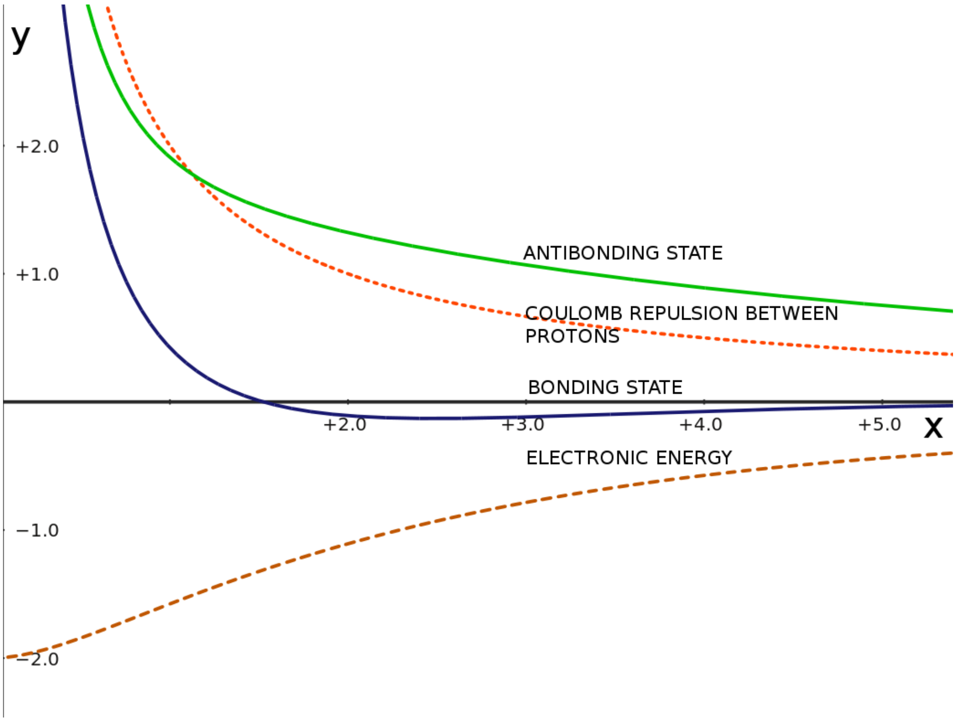

Figure 2.1: The energy of molecular states, the repulsion between the protons, and the binding energy of the electron. The x-axis represents the relative distance between the protons. One unit represents one Bohr radius. The y-axis represents the relative energy. Zero is the combined energy of separated hydrogen atom and ion. So when the curve is beneath the x-axis, it is energetically more favorable to form the combined H_2 ion.

In the case of more complex molecules it is harder to find a descriptive model, but the guide lines from the former models are analogous. Overlapping states split into bonding and antibonding states and the antibonding state is more antibonding than the bonding state is bonding. However, if we consider the next simplest molecule H_2 we have to take into account the spin of the electrons. Electrons in the same state have to have opposite spins. This requirement makes the model a bit more complex. From this requirement arises also one feature of the states: when the bonding state is full the Pauli type repulsion forces the next electrons to the antibonding state.

If the bonding and the antibonding states are full, the molecule is not stable. This is why there is no He_2 molecule. There should be two electrons in both bonding and antibonding states. Molecular orbitals can be detected by using an energy level diagram. From the diagram we can see the names of molecular states, occupation of the states, and states which will fill next if the molecule obtains extra electrons. From the diagram we can also see which states are bonding and which states are antibonding. Usually the symbol * after the name of an orbital tells that the orbital is of antibonding type. In Fig. 2.2 we can see the energy level diagram of an H_2 molecule and an O_2 molecule. In the case of the H_2 molecule there are two electrons on the σ state, with opposite spins. If we try to make a He_2 molecule both σ and σ^* become fully occupied. So the sum of states is more antibonding than bonding and the molecule splits. [5][6][7][8]

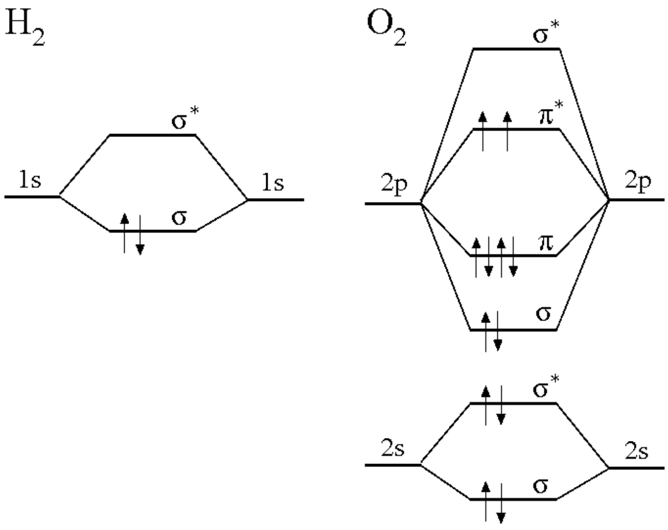

Figure 2.2: The energy level diagram of the H_2 and O_2 molecules. It is worth noticing that each π orbital is split to the π_x and π_y orbitals, so there can be four electrons on the same energy level, and in the case of oxygen molecule it is enegetically favourable, that on the π^* orbital there is one electron on the π_x^* and one on the π_y^* orbital. Therefore in the oxygen molecule there are two electrons with parallel spins on the π^* orbital. This causes the magnetic moment of the molecule.

2.4 Chemisorption and d-band theory

The term chemisoption means that the adsorbed atom or molecule creates a true chemical bond between itself and the substrate. As we learned before, a chemical bond requires overlapping and combination of orbitals. In this section we discuss the chemisorption of a molecule with the help of some examples. Those examples give guidelines for understanding also the adsorption of other kinds of molecules. This section also shows in a simple way why surface can cause dissociation of the adsorbed molecule. Almost all catalytically intresting metals are metals with an active d-band. Therefore it is good to know the effect of the d-band to the reactivity of the surface. The so-called d-band theory explains many features of the metals, for example why gold is the noblest of all metals [9]. And why the metals next to it in the periodic table are different from gold. Now we examine the effect of the d-bands to an approaching hydrogen molecule. The hydrogen molecule is very simple, and thus we can view the effect easily. We have also examined the molecule very closely in the preceding section. There is also a very good model for the adsorption of an H_2 molecule on d-band metals, suggested by Hammer and Nørskov [9][10].

Our study starts when the s-band of the molecule overlaps with the d-band of the surface. Similarly to the case of a molecule when the atomic bands overlap, joint states which can be of bonding, antibonding or non-bonding type are composed when the bands of the molecule and the surface overlap. similarly to the case of a molecule a molecule the joint state splits into the bonding state and the antibonding state which is higher in energy. Splitting into the antibonding and bonding orbitals is not symmetrical however. The up-shift of the antibonding state is larger than the down-shift of the bonding state. This asymmetry arises from the orthogonalization of the states and from The Pauli repulsion. Also the repulsion between the nuclei rises the repulsive energy. Thus if both bonding and antibonding states are fully occupied, the total energy is raised which leads to repulsion. We can now use the way of thinking introduced by the interaction diagram to discuss how molecules interact with surfaces.

In Fig. 2.3 we can see the possible cases of interactions. It is good to know that the surface states interact in the same way with the molecular antibonding states as they interact with molecular bonding states. So the interaction with a filled surface state and with an unfilled molecular antibonding state causes the charge to move to the empty state which causes weakening of the molecular bond. [11]

In the case of an H_2 molecule and a surface of a d-band metal, we have to consider the occupied σ state and unoccupied $\sigma*$ state of the molecule, which is a molecular antibonding state. When the molecule approaches the surface both states overlap

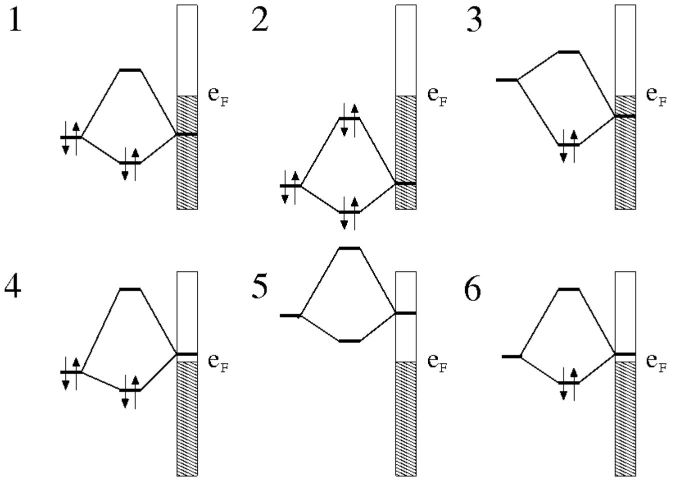

Figure 2.3: An illustrative example of possible interactions between the electronic states of the approaching molecule and the surface. In the diagrams, e_F represents the Fermi level. In each subfigure, the states on the far left represent the states of the molecule before any interaction with the surface (overlapping of the molecular states and surface states). The bar on the far right represents the band structure of the surface, and the states in the middle represent the joint states: the lower state in the energy is the bonding state and the upper state is the antibonding state. Arrows represents electrons. In the cases 1,3,4,6 the interaction is attractive. In the case 2, it is repulsive, and in the case 5 there is no direct consequence.

with the d-band of the metal and split into the bonding and antibonding states. The strongest interaction is between the $\sigma*$ state and the d-band. This interaction is always attractive, because the antibonding part is always above the Fermi level. This interaction also weakens the bond between the atoms inside the molecule. Also the interaction between the d-band and the σ state produces a bonding state which is always beneath the Fermi level. The antibonding part of this interaction is the key to explain the difference between the d-band metals. In interaction with the noble metals the antibonding part is under the Fermi level and in interaction with transition metal the antibonding part is above the Fermi level. In Fig. 2.4 we can see a schematic presentation of these cases. [9][10]

However the case is not so simple: Pre-adsorbed atoms on the transition metal surface can shift the center of the d-band of the surface atoms down in energy, which causes a wider adsorption barrier [12]. Also publication II gives the same results. Also the different surface structures can cause downshift or upsihift of the center of the d-band in energy. Shifting the center of the d-band down in the energy shifts also shared states down in energy, so that the antibonding part of the shared σ

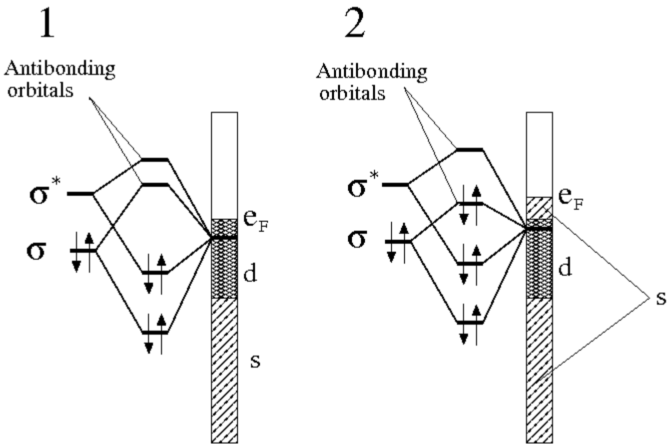

Figure 2.4: The schematic energy diagram of split states between a H_2 molecule and the metal surface. In case 1 the molecule is adsorbed on the transition metal surface. In this case the strongest interaction is attractive interaction between empty σ^* and the d-band. This interaction gives also charge to molecular σ^* and so causes weakening of the bonding between the atoms in the molecule. In this case the splitted antibonding states stay empty, because they stay above the Fermi level. So the molecule is dissociated without barrier on a transition metal surface. In case 2 the molecule is adsorbed on a noble metal surface. Because of higher Fermi level the first split antibonding state in now below the Fermi level, so the surface is not so reactive towards the molecule.

state can go below the Fermi level. It is worth of noticing that the real states are not narrow lines like in the schematic pictures. In the realistic case the states are much more expanded. Also the orthogonalization energy cost increases monotonically with the expansion of the d-band. That is why gold with a full 5d-band is less reactive toward the H_2 molecule than copper with a full 3d-band. The center of the d-band with both metals are about in the same position, but the 5d-band is more extended than the 3-band. That is why gold is the noblest metal of all [9][10].

2.5 Potential energy surface

It is often important to know the energy of a molecule approaching the surface at a defined points, and to know the energy barrier for dissociation of the molecule in that site. To define the energy we can calculate the two-dimensional cut through the six dimensional potential energy surface (PES). The calculation of the whole PES yields information on the adsorption sites and energies, vibrational frequencies of the adsorbate and the existence of a barrier for the adsorption. However it carries so much information, that handling a visualization of it is almost impossible. Also the calculation of the whole PES uses lot of computational resources. So we have to make some approximations and calculate only a two-dimensional plot. During the calculation we shift the molecule from a fixed distance towards the surface at a fixed site. At the same time we modify the intermolecular bond length. At the fixed points, we calculate the total energy of the system and plot a map of the energies. This map tells clearly the energies of the channel, but it does not reveal whether the molecule is at the most energetically favorable direction, or if the site is favorable at all. To calculate the right directions and sites on the surface one needs the knowledge of molecular entrance channels near the surfaces. The energies arise from hybridization of atomic orbitals, therefore the knowledge of orbitals assists on understanding molecular behavior. Also the study of similar situations gives a hint of most favorable sites and channels. In the PES calculation the surface atoms are kept frozen. We have performed a couple of PES calculations with free surface atoms. In those cases we keep the positions of atoms of the molecule fixed and let the surface atoms relax to the energetically favorable positions. However, in many cases this kind of calculation is not close to the realistic case, because in many cases the adsorption is much faster than the modification of the surface. Because the adsorbent atoms are much lighter than the atoms in the surface the speed of the adsorbants is much faster. Also that kind of calculations use a lot more computational resources. The result of our test was that the PES plot did not change radically. This issue is discussed more thoroughly in publication II.

From the PES plot one can see the adsorption energy, and the adsorption barrier. One can also identify whether the dissociation is possible at a particular site, and how much energy it needs (endothermic) or how much energy it releases (exothermic). In some cases one can also conclude whether the adsorption energy turns into dissociative energy or, on the other hand, if the dissociation of the molecule needs external vibrational energy. In our PES plot pictures the horizontal axis represents the inter molecular bond length, and the vertical axis represents the molecular center of mass distance from the surface. Rising contours represent the increasing energy of the molecule. Fig. 2.5 shows some features of PES plots. Dots on the figure represent the calculated locations of the atoms in molecule, in other words which pair of intermolecular bonding lengths and distances between the surface and the molecule we have used to compose the PES plot. Since the calculation for any one point takes a mentionable cost in computational resources, one tries to achieve good results using the smallest possible set of points. That is why the density of simulated points is very scarce outside adsorptioni channel (in Fig. 2.5) and much denser inside the channel. In Fig. 2.6 one can see examples of different kinds of PES plots. We can use those plots to explain how to interpret two-dimensional PES plots. In the subfigure 1 one can see the PES of the adsorption site where the molecule seems to dissociate spontaneously, and gets a about 1.8 eV extra energy. In the subfigure

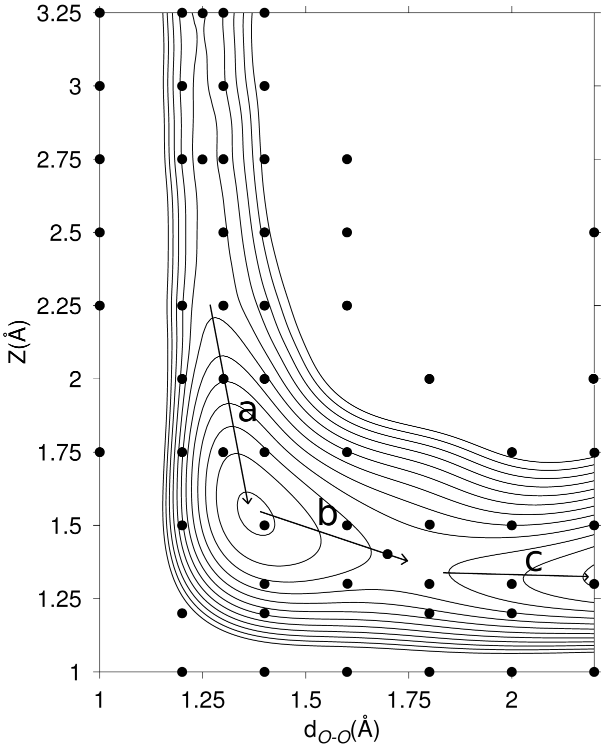

Figure 2.5: An example of a contour plot along two-dimensional PES cuts through the six-dimensional space of O_2 approaching a metal surface, also called an elbow plot. The horizontal axis represents the intra molecular bond-length, and the vertical axis represents the molecular centre of mass distance from the surface. The dots represent the calculated points. Typically the dots are not plotted in the figure, but in this case they are shown to explain the way the PES calculations are performed. The arrow a in the figure shows the entrance channel and the increasing energy of the molecule when it arrives to the molecular adsorption site. In this case the increasing in the energy is 0.7 eV, because the contour spacing is 0.1 eV. The arrow b represents the dissociation barrier, and arrow c represents the dissociation energy.

2 one can see the PES to a repulsive site. The O_2 loses energy when it approaches the site. The cost in energy is about 1.5 eV. If we calculate a PES plot to a certain site and a certain orientation, and see that it is not a reactive site, yet we know that the surface is reactive towards that molecule, we can deduce that the reaction will happen in some other site (or anohter orientation). In the subfigure 3 one can see a case where there is clear molecular adsorption site. The barrier to the dissociation is about 1.5 eV so it is not probable that dissociation occurs on this site. It is possible

that the molecule drifts to another site, and dissociates there. In the subfigure 4 one can see a very attractive site with only 0.2 eV dissociation barrier. It is probable that the molecule dissociates at this site almost immediately.

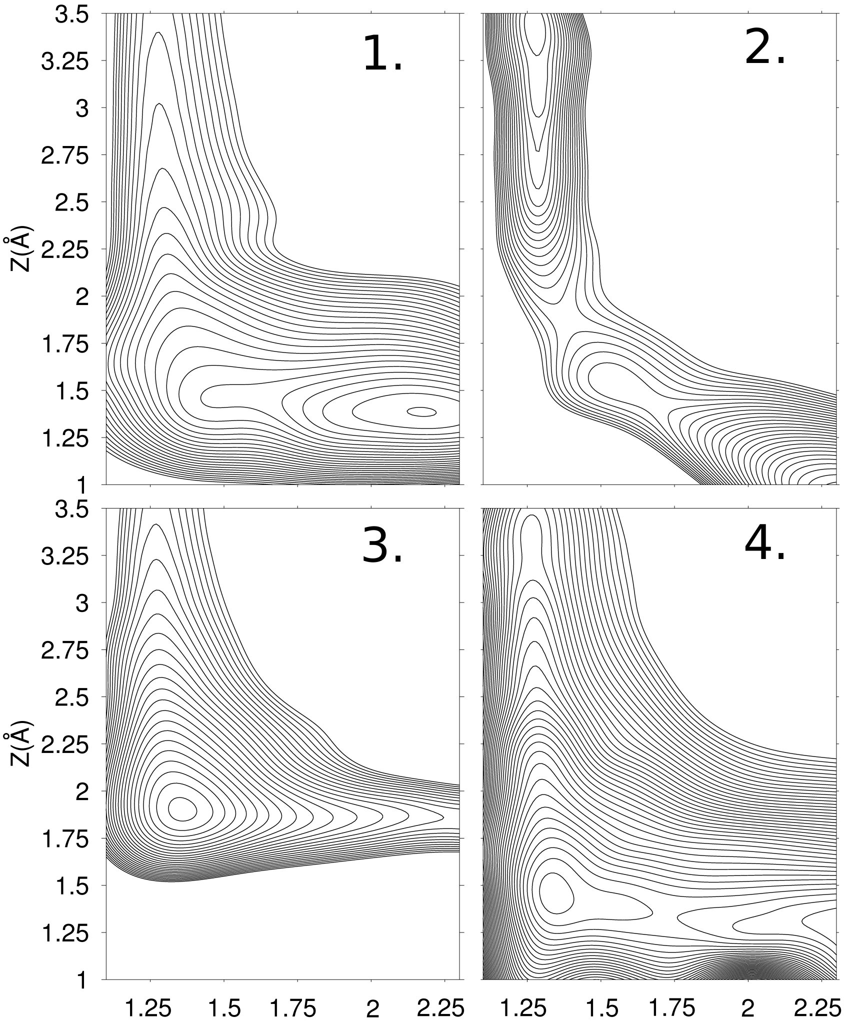

Figure 2.6: Examples of different kind of PES. The contour spacing in all cases is 0.1 eV. 1. The molecule diccosiates spontaneously without any barrier. 2. The approaching of a molecule to a surface in this orientation reqiures extra energy, and is not probable. 3. Molecular adsorption site, the dissociation of the molecule is not probable in this orientation. 4. Molecular adsorption site and minor barrier to dissociation.

2.6 Computational Methods

In *ab initio* calculations, there are many choices to the as to which kinds of functions one uses to represent the set of single electron wave functions. In this study we have used Vienna $Ab-initio$ Simulation Package (VASP) [13][14][15][16], which uses plane waves, and Spanish initiative for Electronic Simulations with Thousands of Atoms (SIESTA) code [17][18], which uses localized orbitals of different symmetry to describe the wavefunctions of the electrons [19][20][21]. Both methods have their strenghts and weaknesses. Most of the calculations for this thesis were performed by using VASP with Projector Augmented Wave (PAW) potentials [22], but in one publication we made calculations using the SIESTA code. In publication I we used SIESTA code to calculate PES figures and molecular dynamics, and in publications III-VII we compared our VASP calculations to LEED calculations performed by my collaborators. LEED is a widely used diffraction based method. In this method, to form a view of the surface structure, the experimentally measured data is compared to the theoretically simulated LEED intensities. Within both DFT methods (SIESTA and VASP), the Monkhorst-Pack [23] method is used to sample the Fourier space in the first Brillouin zone.

The PAW method used in VASP is a general approach to the solution of the electronic structure that reformulates the Orthogonalized Plane Waves method (OPW) method introduced by W. C. Herring in 1940 [24]. The PAW method adds to to the OPW method modern tecniques for calculation of total energy, forces, and stress. The PAW method introduces projectors and auxiliary localized functions. It also defines a functional for the total energy that involves auxiliary functions and it uses advances in algorithms for efficient solutions of the generalized eigenvalue problem. Mathematically a functional is a transformation that maps a function to a (real or complex) scalar. Another difference between the PAW and pseudopotential methods is that the PAW method keeps the full all-electron wavefunction. However, near the nuclei where the wavefuction varies rapidly all integrals are evaluated as a combination of integrals of smooth functions extending throught space plus localized contributions evaluated by radial integration over muffin-tin spheres [25].

The reason to choose the plane-wave based VASP for most of the studies is that the quality of a basis composed of atom-centered local orbitals depends on the relative atomic positions, whereas the quality of the plane-wave basis is independent of the topology of the system [26]. The VASP package also offers a complete and thoroughly tested set of PAW potentials for all elements. However, SIESTA is faster than VASP, so in some cases it is a better choice. A good example of this kind of situations are the molecular dynamics calculations, which require a lot of computational resources and wall clock time.

In the atomic structure relaxation calculations with VASP we use a quasi-Newton [27] algorithm to relax the ions into their instantaneous groundstate. The forces and the stress tensor are used as search directions to find the equilibrium position. Total energy is not taken into account. Forces on the atoms and stresses in unit cell are derivatives of the free energy with respect to the ionic positions and the shape of the unti cell. The derivatives of free-energy contain Hellmann-Feynman [2][3] and Pulay [28] contributions [26]. In the atomic relaxation the first part of the ionic step is the calculation of the electronic structure. The electronic structure is then used to obtain information on the size and a direction of the forces and the stress tensor. As a final step, based on the forces and directions, the sofware package moves the ions (taking pre-defined restriction in to account). Then the ionic loop starts again. This is continued until the convergence criterion is reached. More information on the computational details can be found in the corresponding papers.

2.6.1 Density functional theory

The original density functional theory of quantum systems is the method L. H. Thomas [29] and E. Fermi [30] proposed in 1927. In the original method the kinetic energy of the electrons of the system is approximated as an explict functional of density, idealized as non-interacting electron in a homogenous gas with density equal to the local density any given point. The Thomas-Fermi theory was quite useful for describing some qualitative trends, e.g., for total energies of atoms, but on the other hand it was almost useless : for example it did not lead to any chemical binding [31]. In the homogenous electron-gas, in the presence of a constant external potential V_{ext} the chemical potential μ can be expressed as

$$\mu = \frac{\hbar^2}{2m}(3\pi^2 n(\mathbf{r}))^{2/3} + V_{\mathrm{ext}}(\mathbf{r}). \tag{2.38}$$

In 1930 P. A. M. Dirac [32] expanded the theory of Thomas and Fermi by formulating the local approximation for exchange. It leads to the energy functional $E[n]$ for electron in an external potential $V_{\mathrm{ext}}(\mathbf{r})$

$$\begin{aligned} E[n] =& C_1 \int \mathrm{d}^3\mathbf{r} n(\mathbf{r})^{5/3} + \int \mathrm{d}^3\mathbf{r} V_{\mathrm{ext}}(\mathbf{r}) n(\mathbf{r}) + C_2 \int \mathrm{d}^3\mathbf{r} n(\mathbf{r})^{4/3} \\ &+ \frac{1}{2}\int \mathrm{d}^3\mathbf{r}\mathrm{d}^3\mathbf{r}' \frac{n(\mathbf{r})n(\mathbf{r}')}{|\mathbf{r}-\mathbf{r}'|}, \end{aligned} \tag{2.39}$$

where the the first term is the local approximation for the kinetic energy with

$$C_1 = \frac{3}{10}(3\pi^2)^{2/3} \tag{2.40}$$

in the atomic unit cell. The third term is the local exchange with

$$C_2 = -\frac{3}{4}(\frac{3}{\pi})^{1/3}, \tag{2.41}$$

and the last term is the classical electronic Hartree energy. The ground state density and energy can be found by minimizing the functional $E[n]$ for all possible $n(r)$.

However, the real starting point of modern DFT was the Hohenberg-Kohn formulation of DFT [31]. The basic lemma of the formulation was: The ground-state density $n(\mathbf{r})$ of a bound system of interacting electrons in some external potential $v(\mathbf{r})$ determines this potential uniquely. [33]

Density functional theory is the most widely used method today for electronic structure calculations because of the approach proposed by Kohn and Sham [34]. The Kohn-Sham approach is to replace the difficulties related with the Hamiltonian with a different auxiliary system that can be solved more easily [35]. The ansatz assumes that the ground state density of the original interacting system can be replaced by a chosen non-intercting system, where all the difficult many-body terms are incorporated into an exchange-correlation functional of the density. The Kohn-Sham ground state energy $\mathrm{E_{ks}}$ can be found by using the equation

$$E_{\mathrm{ks}} = T_{\mathrm{s}}[n] + \int \mathrm{d}\mathbf{r} V_{ext}(\mathbf{r})n(\mathbf{r}) + E_{\mathrm{Hartree}}[n] + E_{\mathrm{II}} + E_{xc}[n], \tag{2.42}$$

where T_{s} is the kinetic energy of the independent particle, $V_{\mathrm{ext}}(\mathbf{r})$ is the external potential due to the nuclei and any other external fields, and E_{II} is the interaction between the nuclei. $E_{\mathrm{Hartree}}[n]$ is the classical Coulomb interaction energy of electron density $n(\mathbf{r})$ interacting with itself. It is defined as

$$E_{\mathrm{Hartree}}[n] = \frac{1}{2}\int \mathrm{d}^3\mathbf{r}\mathrm{d}^3\mathbf{r}' \frac{n(\mathbf{r})n(\mathbf{r}')}{|\mathbf{r}-\mathbf{r}'|}. \tag{2.43}$$

The E_{xc} is the exchange-correlation energy. Several different schemes have been developed in order to approximate it. The main source of errors in DFT usually arises from the approximation of E_{xc}. One way to approximate it is to use the local density approximation (LDA) [35][36][37], i.e.

$$E_{\mathrm{xc}} = \int n(\mathbf{r})\epsilon_{\mathrm{xc}}[n(\mathbf{r})]\mathrm{d}\mathbf{r}, \tag{2.44}$$

where the $\epsilon_{\mathrm{xc}}[n(\mathbf{r})]$ is the exchange correlation energy per electron in a homogeneous electron gas of constant density. In a hypotetical homogenous electron gas, an infinite number of electrons travel through a space of infinite volume in which there is a uniform and continuouns distribution of positive charge to retain electroneutrality. This expression for the exhange-correlation energy is clearly an approximation because neither positive charge nor electronic charge are uniformly distributed in the real atomic system. Usually LDA shows over binding, and it fails in many cases [38]. Therefore usually a better way to approximate E_{xc} is the Generalized Gradient Approximation (GGA) [39][40][41][42][43], it is

$$E_{\mathrm{xc}} = \int n(\mathbf{r})\epsilon_{\mathrm{xc}}[n(\mathbf{r}), | \bigtriangledown n(\mathbf{r})|]\mathrm{d}\mathbf{r}. \tag{2.45}$$

Now there a is gradient of the density included in the approximation.

For calculations of the Kohn-Sham ground state it is possible to distinguish two categories of methods. In methods of the first category one tries to determine the minimum of the Kohn-Sham total energy functional directly. Those methods are based on the work of Car and Parrinello [44]. They founded their work to the fact that the Kohn-Sham energy functional is minimal at the electronic ground state. The second category of methods are iterative methods for the diagonalization of the Kohn-Sham Hamiltonian in conjunction with an iterave improvement. For VASP and large systems it has been found that the most efficient iterative method is the “residual vector minimization scheme-direct inversion in the iterative subspace” (RMM-DIIS) [27][45]. [14]

Chapter 3

Review of the calculations

The purpose of my research was to better understand the atomic level phenomena of catalytically active transition metal surfaces, for example the dissociation of the oxygen molecule. For my research I have used calculation packages based on quantum mechanics, which can calculate the electronic structure of surfaces and molecules without any experimental data. However, in many cases the results are compared to experimental results, with good correlation. The purpose of this study is not only to better understand the atomic level phenomena, but also to find a way to control them. The controlling of the surface phenomena demands in many cases modification of the surface where the reaction occurs. For that reason I have also studied the modification of the surfaces.

3.1 Adsorption and dissociation of an oxygen molecule

3.1.1 Palladium (211) surface

While studying real catalytic processes on metal surfaces, one needs to keep in mind that the real surfaces consist of several different lattice planes, and that there are defects. Usually there are also some preadsorbed atoms on the surface. For that reason a study can not be limited to smooth surfaces. It is also generally considered to be known that the reactivity of stepped surfaces is higher compared to low index surfaces. This is because the ledges of steps have a lot of broken bonds, which increases the reactivity of the surfaces. The FCC-metal surface with Miller index (211) is very simple and known to be stable [46]. For the aforementioned reasons, and because we assume it to be very reactive, we decided this to be a suitable choice for our study. Publication I contains studies for the reactivity of palladium and copper(211) surfaces. The (211) surface is composed of (100)-surfaces (ledges of steps), and (111) microfacets. Since we know that the Cu/Pd (111) surface is not very reactive, we can omit the (111) microfacets from the study. We can still assume the reactivity to be high, because the (100)-microfacets of Cu/Pd are quite reactive. It will also be interesting to compare the results obtained on the (100)-microfacets to those of a smooth (100) surface.

In Publication I we study the reactivity by using several PES calculations. The result of the study is that the (211) ledge of the step is far more reactive on both metals (Cu and Pd) than the smooth surface. The reactivity of smooth Cu(100) can be found in Refs. [47][48][49], and the PES calculation for the O_2 approaching the hollow site of the smooth Pd(100) surface can be found in Publication II. In Publications I and II, the approach and dissociation of an oxygen molecule is studied mostly from the perspective of the surface. Another way to study those reactions is to examine what happens to the molecular orbitals of O_2. Shortly, we discuss the results of publications I and II from this perspective. It clears up some points made in the publications and gives deeper insight to the results. When a spin polarized oxygen molecule is approaching a palladium or a copper surface it loses its spin polarisation, as we will show later. To observe what the effect of this modification can be we must first discuss the free molecule briefly. The O_2 molecule posesses a very unique configuration, which leads to a very versatile chemistry. The free oxygen molecule has three ground state forms: one triplet state and two metastable singlet states. In Fig. 2.2, a schematic presentation of the molecular orbitals of an oxygen molecule is shown. It represents the triplet state because there are two electrons with parallel spins on the π^* orbital. Consistently on the singlet states there are electrons with opposite spins on the π^* orbital. Now there are two possible ways to locate the electrons on the orbital. Both electrons can be on the π_x^* orbital or the other electron can be on the π_y^* orbital (On the triplet mode both electrons can not be on the π_x^* orbital because of the Pauli rule). In experiments it has been found that the singlet states are energetically 0.98 eV and 1.63 eV higher than the triplet state, [50], so we can assume that the lack of spin polarisation weakens the bond between oxygen atoms significantly. The singlet oxygen has been shown to be important in biological chemistry [51][52]. In order to use the information of the energy level diagram, and to analyze local density of states plots in the case of the surface and molecule, we show the orbitals from the calculated local DOS of free oxygen molecule. They are shown in Fig. 3.1.

Now we can examine the local DOS of O_2 approaching different surfaces. Next we show some local DOS and electron density figures in the case of palladium (211) surface. These calculations are performed using VASP [13][14][15][16] including the PAW potentials [22]. A kinetic energy cut-off of 450 eV was applied for the plane waves. For the exchange correlation potential the GGA of the Perdew-Wang 91 flavor [54] was employed. For the k-point sampling, the $8 \times 8 \times 1$ Monkhorst-Pack [23]

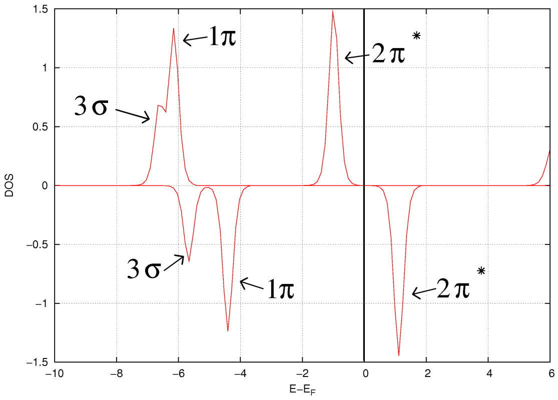

Figure 3.1: The local DOS of a O_2 molecule plotted for the electrons originally at the p-orbitals of an oxygen atom. The names of the orbitals are shown in the Fig. [53]. The figure is calculated by using VASP and PAW potentials. The peaks above the zero line represent the spin up states, and the peaks below the zero represent the spin down states.

mesh was used, and the size of the super cell was the same as in publication I. In Fig. 3.3 one can see how the local DOS of the oxygen molecule changes when the molecule is approaching the hollow site on the ledge of a step on the palladium (211) surface. Schematic figures show the orientaion of the molecule(Fig. 3.2). Distances between the molecule and the surface are measured from the center of the mass of the molecule to the center of the hollow site. The DOS plots shown in Fig. 3.3 are from the distances of 1.5 Å, 1.75 Å, 2 Å, 2.5 Å and 3 Å. The internuclear distance between the atoms in the molecule is 1.3 Å in every case, except in the last one, where it is 1.5 Å.

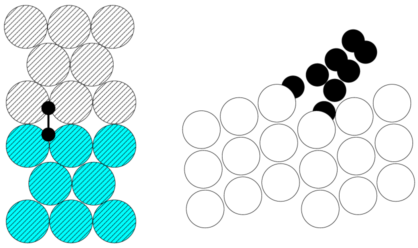

Figure 3.2: Schematic top and side view of the calculated adsorption site and adsorption channel.

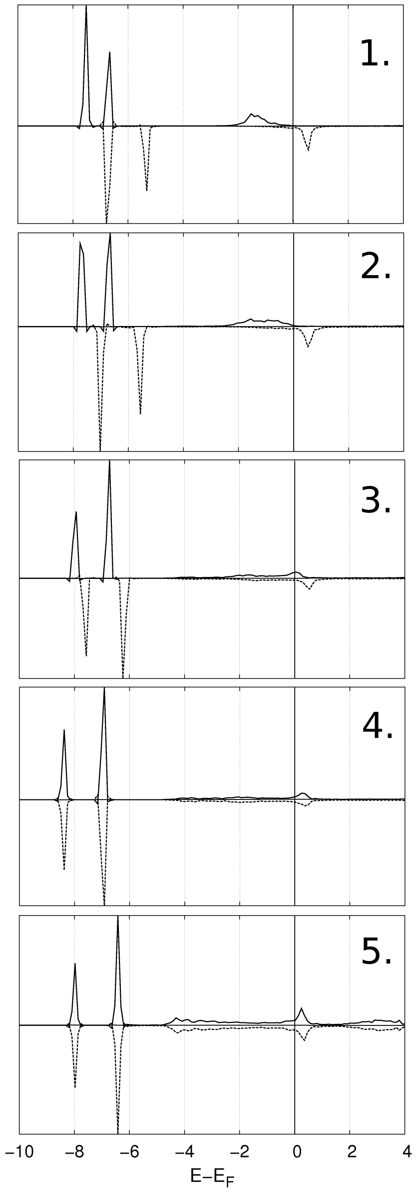

Figure 3.3: Local densities of states of an O_2 molecule approaching the hollow site on the palladium (211) surface ledge of step. Orientation of the molecule can be seen in Fig. 3.2. Heights from the surface and intermolecular bonding lenghts are in Ångstroms : 1: (3.00, 1.30), 2: (2.50, 1.30), 3: (2.00, 1.30), 4: (1.75, 1.30), 5: (1.50, 1.50).

In Fig. 3.3 we can clearly see that the spin polarisation of O_2 disappears, and the half empty antibonding orbital $2\pi^*$ interacts strongly with the surface states. If we compare the DOS of a free O_2 molecule and the local DOS of an O_2 molecule 3.0 Å above the surface, we can see that there is alredy mixing of the molecular orbitals and the surface states. This observation supports the PES plot of the same situation, which can be seen in Fig. 3.4. The PES plot is originally from publication I, and it is calculated by using SIESTA. Exact information on the calculation method can be found in publication I. In the PES plot one can see that the downhill (in energy) of the molecule starts already at the height of 3.0 Å. In other words: for a molecule at that distance from the surface it is energetically more favourable to approach the surface than to drift away from the surface. Also the molecular orbitals 1π and 3σ have interaction with the surface. However, this interaction is not as strong as the interaction with the $2\pi^*$ orbital. Charge transfer from the surface to the molecule is still quite minor. Pader analysis [55][56][57] found that 0.6 electrons transfer from the surface to the molecule when the distance between the molecule and the surface is 1.75 Å, and 0.8 electrons transfer from the surface to the molecule when the distance is 1.5 Å. Qi *et al.* have found in Ref. [58] that the amount of electrons transfered from a Pt surface to an oxygen molecule is always less than 1.3. Their observation supports our study, as Pt is not as reactive as Pd.

Let us next take a 3-dimensional analysis of the orbitals of the oxygen molecule above the surface. This analysis, however, has to begin by looking at the partial charge density of the free O_2 molecule. We calculated the molecule with VASP and plotted the charge density in different energy values by using different colours. The image is plotted by using the VMD software [59]. In Fig. 3.5 one can see the π^* orbital (energies 0...-2 eV below the Fermi level), π orbital (energies -3...-5 eV spin down and -6...-6.5 spin up), and σ orbital (energies -5...-6 eV spin down and -6.5...-7 spin up). These energies can be compared to the local DOS plot of an oxygen atom in the O_2 molecule in the same situation. The π^* orbital is plotted in gray. From the figure we can clearly see that the π^* orbital is of antibonding type, because the charge is accumulated to the ends of the molecule and in the middle of the molecule there is no charge. The π orbital, plotted in blue, and the σ orbital, plotted in red, are clearly bonding type orbitals, because the charge is mainly in the center of the molecule. The nuclei are not plotted in the figure, but they are located on the narrow points of the σ orbital.

The 3-dimensional orbital view of the oxygen molecule alone does not give any new information about what we have discussed before. However, now we can plot the partial charge density in the same way in the cases where something interesting occurs in the molecule. In Fig. 3.6 the partial charge density of the O_2 molecule above the hollow site of the ledge of a step on Pd(211) surface is plotted. The orientation

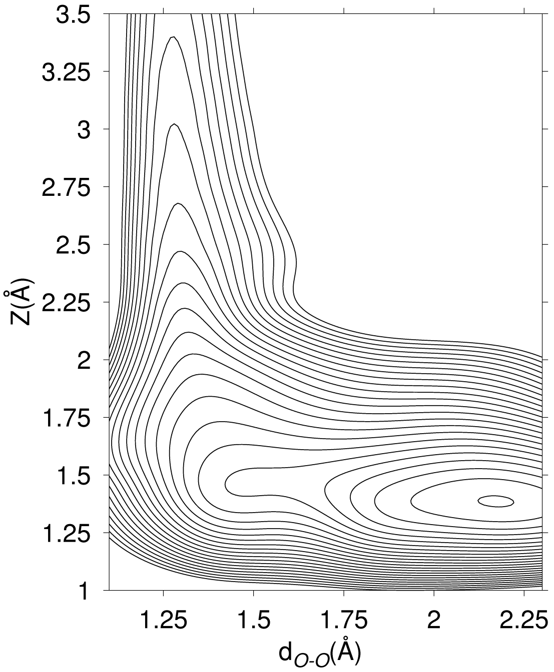

Figure 3.4: The calculated 2-D cuts of the PES on Pd(211) surface with the O_2 molecule approaching the hollow site on the (100) microfacet. The orientation of the molecule can be seen in Fig. 3.2. The contour spacing in the figure is 0.1 eV.

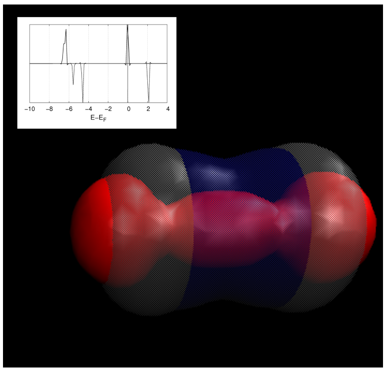

Figure 3.5: The local DOS of an oxygen molecule and a 3-dimensional plot of partial charge density of oxygen molecule orbitals calculated with VASP and PAW potentials. In the figure grey colour represents the π^* orbital, blue colour represents the π orbital and red colour represents the σ orbital.

of the molecule is the same as in the DOS plot part 4 in Fig. 3.3. The distance between the center of mass of the molecule and the center of the hollow site is 1.75 Å, and the distance between the oxygen atoms is 1.5 Å. The π^* is plotted orbital in gray (energies between 0...-5 eV below the Fermi level), the π orbital in blue (energies between -6...-8 eV below the Fermi level), and the σ orbital in red (energies between -8...-10 eV below the Fermi level). In Fig. 3.6 one can see that binding between the surface and the molecular states is strongest in the case of the π^* state (molecular antibonding state). One can see that the other states bind to the surface also. That supports the observation from the DOS plots. One can also see that there is no antibonding between the molecule and the surface. The σ orbital, which in the case of the free molecule calculated with VASP looks like dumbbell, is now bent towards the bridge sites of the palladium surface. The π orbital looks like it is drawn to the palladium atoms. It also binds to the nearest palladium atom on the terasse. That is why it appears to be drawn towards it. Pader analysis yields that the charge of the oxygen atom, the lower one in the picture, is 0.05 electrons more than the upper one in the picture. The difference is quite small but it proves that the difference seen in the picture is real. The PES plot on the publication II corresponds to the observation of this chapter: There is strong bonding between the molecule and the surface and a lack of antibonding states between the molecule and the surface. In the PES plot there is a downhill of 1.8 eV without a dissociation barrier.

By using the information from the 3-dimensional partial charge density plot and local DOS plots we can construct the schematic energy level diagram by using theory from Section 2.4 . This diagram can be seen in Fig. 3.7 . In this case there is nothing exceptional about the diagram, but we can use it for comparing it with other cases later on.

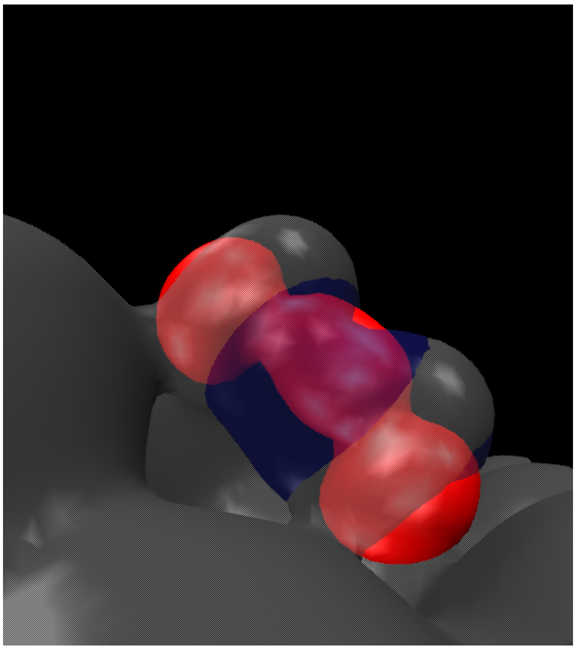

Figure 3.6: Partial charge density of the oxygen molecule on the hollow site of Pd(211) surface's (100) microfacet. The distance between the center of mass of the molecule and the center of the hollow site is 1.75 Å, and the distance between the oxygen atoms is 1.3 Å.

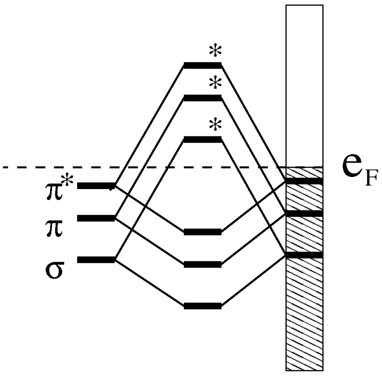

Figure 3.7: A schematic energy level diagram for the interaction of oxygen molecular orbitals and surface states in the case where the O_2 molecule approaches the hollow site of the palladium (211) surfaces on the ledge of the step.

3.1.2 Sulphur and oxygen precovered palladium (100) surface

In this section we present some results that expand the results of Publication II and bring those results to the same context as the theories of sections 2.4 and 3.1.1. All calculations in this section are performed in the same way as in Publication II.

In Publication II we studied the dissociation of an oxygen molecule on sulphur and oxygen precovered Pd(100) surfaces. The methods that we used previously to give more information about the dissociation of an O_2 molecule on palladium (211)-surface can also be useful to examine what occurs inside the molecule in the case of a surface with preadsorped atoms. It is interesting to know how the molecular orbitals evolve. Let us start with the local DOS of the oxygen molecule approaching the hollow site of the palladium surface next to a preadsoped sulfur atom. In publication II the local DOS of the d-band of a surface palladium atoms with different sulfur coverage can be seen. The center of the d-band shifts down because of the influence of the sulfur atoms. With d-band theory this action should make the surface less reactive, and this can be seen in the PES plots of the Publication II.

The most interesting case is the one with the smallest coverage of sulfur atoms (0.125 ML). There we can observe how a small change of the center of the d-band of the surface palladium atoms can modify the orbitals of the oxygen molecule. From the PES plot where the molecule approaches the hollow site next to an S atom (Fig. 3.9), it can be seen that there is a downhill of 0.8 eV, and dissociation barrier of 0.3 eV, whereas on the clean surface on the same site there is downhill of 1.4 eV and a dissociation barrier of 0.1 eV. Based upon the d-band theory we can assume that an antibonding state is formed between the surface and the molecule. In Fig. 3.8 one can see local DOS plots showing how the oxygen states evolve when the molecule approaches the surface. The distances between the surface and the center of mass of the molecule, and the inter molecular bond lenghts in the DOS plots are: 1: (3.0 Å, 1.3 Å), 2: (2.5 Å , 1.3 Å), 3: (2.0 Å , 1.3 Å), 4: (1.75 Å, 1.3 Å), 5: (1.5 Å, 1.5 Å). From the PES plot in fig. 3.9 it can be seen that in the case of DOS plot 5, the molecule is on the molecular adsorption site. If we compare the DOS plots with shortest distance from the surface to the DOS plots of the (211) surface with the same distances from the surface, we can see that there is no significant difference near the Fermi level. From this we can deduce that the reasons for the change in reactivity are located somewhere else in the orbitals. The partial charge density with different energy from last partial DOS plot can be seen in Fig. 3.10. The grey area is clearly the π^* orbital, which is bonded with the surface states, as in the case of clean (211) surface. In the DOS plot on this energy interval one can see several peaks, but in the charge density plots the peaks do not seem to matter; the whole energy interval seems to be distributed similarly. For that reason we have plotted that energy interval with the same color (gray). The blue area is clearly the π orbital, and it also bonds with the surface states. But the bond seems to be weak, and the whole orbital looks smaller than in the case on the clean (211) surface, even if it was plotted at the same isosurface value. However we can not make

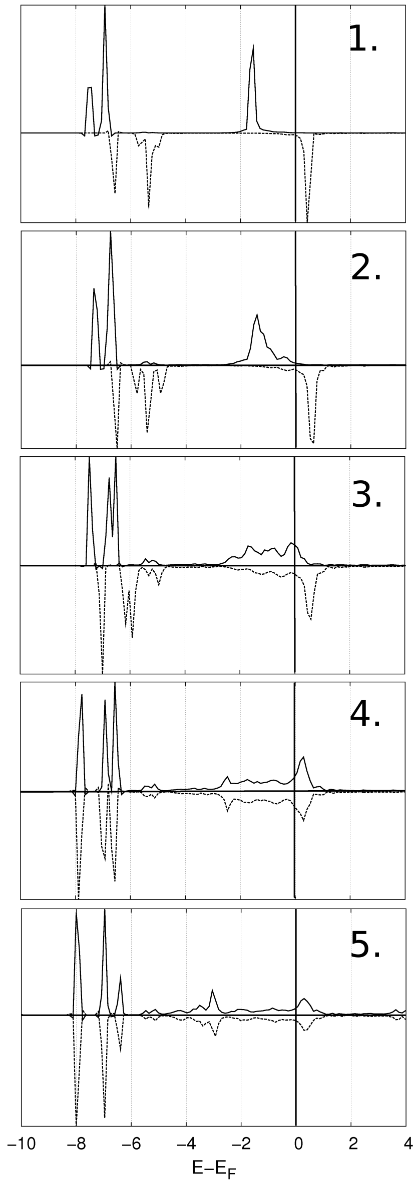

Figure 3.8: Local DOSes of O_2 molecule approaching the hollow site next to the preadsorbed sulphur atom on the palladium (100). The coverage of sulphur atoms is 0.125 monolayer. Heights from the surface and intermolecular bonding lenghts are in Ångstroms : 1: (3.00, 1.30), 2: (2.50, 1.30), 3: (2.00, 1.30), 4: (1.75, 1.30), 5: (1.50, 1.50).

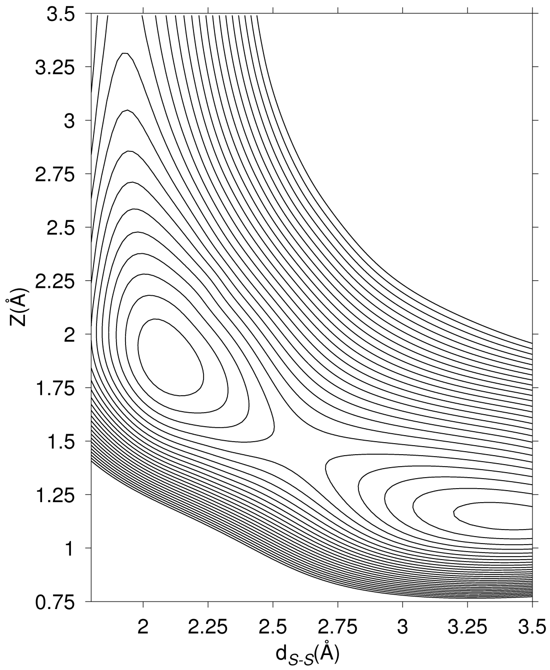

Figure 3.9: The calculated 2-D cuts of the PES for 0.125 ML sulphur precovered Pd(100) surface when the O_2 molecule approaches the hollow site next to an S atom. The contour spacing in the figure is 0.1 eV.

any conclusions from that. The red area is formed by two different orbitals. The energy values -7.25...-8.25 eV below the Fermi level compose the σ orbital, which is clearly bondend with the surface, as in the case of the clean (211) surface (the area that looks like a dumbbell with its ends bent towards the surface). The other part of the red area (energies between -6...-6.6 eV below the Fermi level) looks like the bonding σ orbital in the case of Pd(211), but the heads are curved away from the surface. This orbital seems to be an antibonding state between the surface and the molecule. Now, by using the d-band theory, we can compose the energy level diagram, which can be seen in Fig. 3.11. We can see that the σ orbital is split to bonding and antibonding states. This observation fits well to the theory and results from publication II.

However, if we observe more clearly the DOSes from Fig. 3.8, it seems that the electrons come to the antibonding states from the π orbital. The orbital seems to be split into two states, which is possible because it consists of two parts, so the

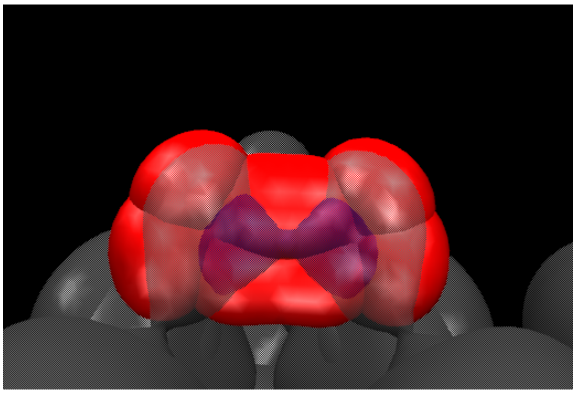

Figure 3.10: 3-dimensional plot of the partial charge density of the oxygen molecule on the hollow site next to preadsorped sulphur atom on Pd(100) surface. The colors in the figure represent the following energy values: grey: energies 0...-6 eV below the Fermi level, blue: -6.6...-7.25 eV below the Fermi level, red: -6...-6.6 and -7.25...-8.25 eV below the Fermi level.

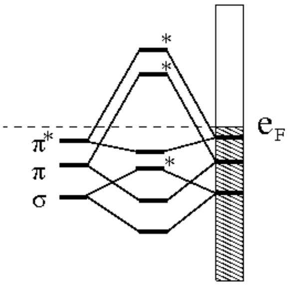

Figure 3.11: Schematic energy level diagram of the states between the oxygen molecule and the surface in the case of 0.125 monolayer surface coverage on the palladium (100) surface.

antibonding state between the surface and the molecule seems to be part of the π orbital. However, in the VASP calculations it looks like the σ orbital. In subfigure 1 (distance between the molecule and the surface is 3.0 Å) the spin down part of the π orbital starts to split to three parts. In subfigure 2 (distance between the molecule and the surface is 2.5 Å) the splitting of the orbital can be cearly seen. In subfigure 3 (distance between the molecule and the surface is 2.0 Å) also the spin up part of the π orbital is already split to the bonding and the antibonding parts. So the splitting of the spin up part of the π orbital occurs when the distance between the molecule and the surface is between 2.5-3 Å. This observation explains why the π orbital looks smaller, and the σ orbital looks the same as in the case of clean (211) surface. More studies are needed to explain in more detail how the molecular orbitals evolve in this case. The σ state (the one which looks like a dumbbell with its ends bent away from surface in Fig. 3.10) is clearly an antibonding state between the molecule and the surface. In order to be sure that this is not due to any errors in our calculations or any error in plotting the figures, we chose to study the case further by examining a similar situation, but with preadsorbed oxygen. In the following, we will refer to this state as ”the extra peak“.

We choose the same coverage as in the case of sulfur (0.125 ML) and study the adsorption of the molecule to the hollow site next to the preadsorped oxygen atom. In Fig. 3.12 one can see the 2-dimensional PES plot at the site. In fig. 3.13 one can see the local DOS plot of the molecule in the molecular adsorption site (distance between the center of mass of the atom and the center of the hollow site is 1.5 Å and the bond length of the oxygen molecule is 1.5 Å). The distances are the same as in the case of precovered sulfur, which makes comparison between the cases more fruitful. The DOS plot is very similar to the case of preadsoped sulfur. In this case also, one can see the state to which we refer as ”the extra peak”. It is worth noting, that no such state is there in the case of the clean (211) surface.

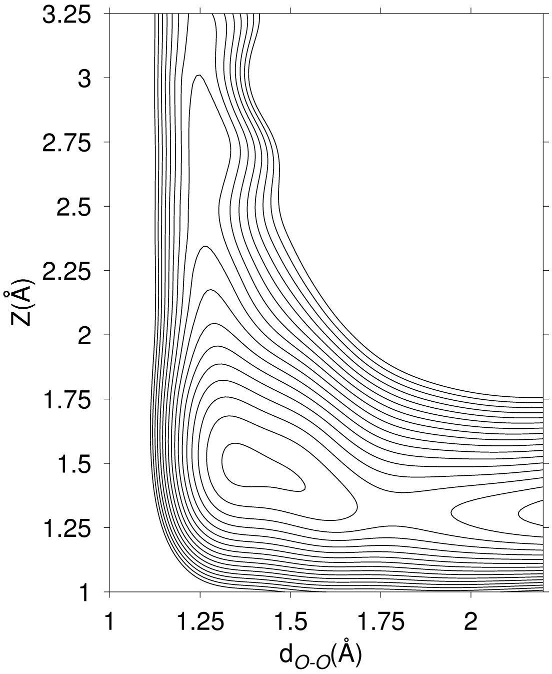

Figure 3.12: The calculated 2-D cuts of the PES for oxygen 0.125 ML precovered Pd(100) surface with the O_2 molecule approaching the hollow site next of the of O atom. The contour spacing in the figure is 0.1 eV.

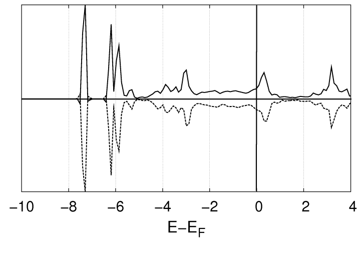

Figure 3.13: Local DOS of the O_2 molecule 1.5 Å above the hollow site next to the preadsorbed oxygen atom on the Pd (100). The coverage of the preadsorbed oxygen atoms is 0.125 monolayer. The intermolecular bonding lenght of the oxygen atoms is 1.5 Å.

Now we can observe the extra peak with the 3 dimensional partial charge density plot, shown in Fig. 3.14. In the figure we plot only the energies in the energy interval -5.5...-8 eV below the Fermi level, because now we can see more clearly the three last peaks in the DOS plot. Now the energies between -8 and -7 eV are plotted in red, the energies between -7 and -6.1 eV are plotted in blue and energies between -6.1 and -5.5 eV below the Fermi level are plotted in gray. The green spheres represent the places of palladium atoms. The σ orbital (energies -8...-7 eV) is again bent towards the surface atoms. The π orbital (energies -7...-6.1 eV) looks the same as in the case of preadsorbed sulphur. Now, looking at the extra peak (energies -6.1...-5.5 eV, plotted in gray), we can see that again it looks like the σ orbital (plotted in red), but it is bent to the opposite way (away from the surface). Also when looking at the situation from above, one can see that the σ orbital is as thin along the axis of the O_2 molecule as the extra peak, whereas the π orbital is much wider, having protruding blobs ballooning to the sides from the positions of the O atoms. With the present tools, it seems evident that the extra peak looks like the σ orbital, not the π orbital, even if the electrons seem to have moved to this state from the π orbital.

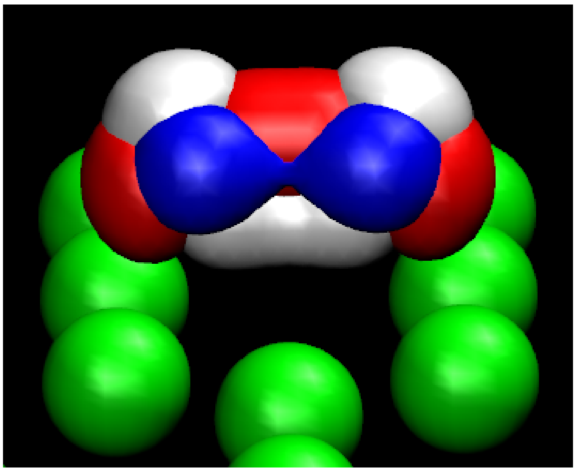

Figure 3.14: 3-dimensional plot of the partial charge density of the oxygen molecule on the hollow site next to a preadsorped sulphur atom on Pd(100) surface. The colours in the figure represent the following energy values: grey: energies -5.5...-6.1 eV below the Fermi level, blue: -6.1...-7 eV below the Fermi level, red: -7...-8 eV below the Fermi level. Energies between 0...-5.5 are not plotted in the figure because with this choice we can see the σ orbital, the π orbital, and the extra peak more clearly. The green spheres represent the location of the palladium atoms.

3.2 First steps of thin film growth

As we can see in section 3.1 and in Publication II, preadsorbed atoms on the surface affect significantly the reactivity of the surface towards oxygen. When adatoms adsorp on a metal surface, the adatoms assume a certain structure, which depends on the species of the surface, on the species of the adatoms, and on the structure the surface had before any adatoms were introduced. Before we can study the reactivity of the surface with adatoms, we have to know the structure of the surface. In real life the catalyst metal surface always has some adatoms. Thus the study of the surface stuctures is a very important part of studying and analysing the reactivity of the surface.

The second purpose of my study is to examine the starting point of the thin film growth. At first, it seems to be a very different subject compared to the study of oxygen catalysis, but if we think it more thoughtfully we can observe that there are many links between these two subjects. Thin metallic films on metallic substrates posses many new features compared to a clean metal surface, and these systems are of intrest from the view point of many technological applications. The growth of thin films is a very complicated process and the starting point of it is a surface covered with adatoms. Many thin films also consist of a metal oxide. In these films the dissociation of the O_2 molecule could be a part of the growth process of a thin film. Thin film growth and the study of surface structures are a good area for observing how well the experimetal results agree with calculated DFT ones.

The most commonly used experimental techniques to probe a surface structure in atomic scale involve photons, electrons, atoms or ions as probes. One of the main diffraction based experimental methods is Low-Energy-Electron-Diffraction (LEED). It is a surface sensitive method. LEED exploits the interaction of elastic low-energy (typically 30-500 eV) electrons with atoms. Structure determinations are achieved by comparing the experimentally measured and theoretically simulated LEED intensities. In Publications III-VI our VASP calculations are compared with LEED calculations performed by my collaborators. Since the LEED method is based on the experimental results, getting convergent results with VASP and LEED gives more importance to both results. Both methods, LEED and DFT, also complement each other in the surface structure calculations. In LEED experiment the periodicity and symmetry of the surface structure is seen [60]. This symmetry information can be used to guide the process of selecting model structure for DFT calculations. On the other hand, with DFT calculations one can eliminate energetically worst structures from a group of possible test geometries, which makes it faster to find the best structure with LEED analysis. LEED is a method of 'trial and error' with relatively small convergence radius. This means that depending of the system studied the number of trial geometries needed can be huge. In contrast to LEED, DFT cover much larger parameter space during 'one run'. The LEED calculations in the publications are done by using the Barbieri/Van Hove SATLEED package [61].

3.2.1 Cu{100}-p(2×6)-2mg-Sn studied by DFT and LEED

In Publication VII we studied the structure of Cu{100}-p(2×6)-2mg-Sn by DFT and LEED. The interaction between the Cu(100) surface and tin is an intresting case because it is a good example of a metal-on-metal epitaxial growth. The large lattice mismatch between tin and copper contributes to complex yet well defined series of ordered phases. Even below the monolayer coverage, at room temperature there are five ordered phases of the Cu(100)-Sn system [62]. However, the exact structures of those phases are not clear. Hence an analysis of surface structures of Sn on the Cu(100) surface yield important knowledge on the first steps of thin film growth. The atomic level knowledge of thin film growth is required in order to develop better thin films for advanced microelectronics, optical and magnetical devices [63]. Another intresting phenomenon related to metal deposited on top of another metal is the charge-density wave (CDW), caused by the phonon by the electron-phonon interaction. A low-dimensional metallic state is unstable because of this interaction and the charge is periodically modulated in CDW ground state [64][65].

In the Publication VII we calculate the total energy of five possible models. Three of those models are suggested in reference [66] and two of the models are proposed by us. With VASP we analyze the surface structures in a way where we put Sn atoms at the defined sites and let the structure relax to the total energy minimum. One can see the energetically best structure in Fig. 3.15. There is a very good agreement between the geometrical parameters extracted from LEED and DFT analyses.

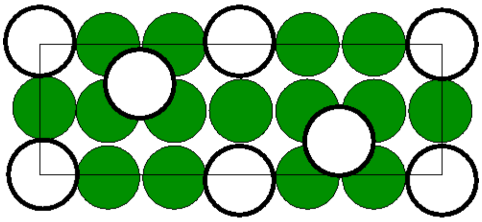

Figure 3.15: Top view of the best model of Cu{100}-p(2×6)-2mg-Sn surface structure.

3.2.2 Structure analysis of bi-metallic surfaces; Rashba effect

In Publications IV-VI we present a detailed analysis of bi-metallic surface structures using LEED I-V measurements together with DFT calculations. The structures studied were p($\sqrt{3} \times \sqrt{3}$)R30° Bi-Ag(111) and p($\sqrt{3} \times \sqrt{3}$)R30° Pb-Ag(111). Both Bi and Pb on the Ag surface take this structure at coverage 1/3 ML. Both cases are very similar and can be easily compared. These cases are good examples of the growth of a semi-metallic overlayer. The observed ($\sqrt{3} \times \sqrt{3}$)R30° is of particular interest as a new class of materials because the two-dimensional alloy structure in both cases appears to behave like a 2-D electron gas with quantum confinemet leading to the Rashba effect, which has implications for spintronic applications such as spin transistor [67][68][69]. The reason why metal surfaces can produce 2-D electron gas like states is the presence of the crystal surface. In some circumstances, it can cause arising of bulk forbidden electronic single-particle states, leading to formation of a band in the corresponding projected bulk band gap [70][71]. These so-called surface states are higly localized perpendicular to the surface [72]. The Rashba effect is a spin-orbital splitting phenomenon without magnetic field, where the electric field acts like a magnetic field. The Rashba Hamiltonian can describe the spin-orbit interaction of an electron, moving with momentum in an electric field oriented along the z axis e$_z$

$$H_R = \alpha_R(\mathbf{e_Z} \times \mathbf{k}) \cdot \mathbf{s}, \tag{3.1}$$

where α_R is the so-called Rashba parameter, which is proportional to the electric field and depends on the spin-orbit coupling strength [73][74]. This phenomenon is originally discovered by E. I. Rashba in 1960 [75]. Controlling the spin degree of freedom of the electron lies at the heart of spintronics [76]. One possibility of manipulating the electron spin without the need of any external magnetic field is the Rashba effect [73]. It is clear that the large conductivity of the Ag substrate short-circuits possible spin currents, so it takes more study to find a material suitable for technological applications. And the exact knowledge of the surfaces where the effect is known to exist gives more possibilities to develop better models for the applications. It is also known that Rashba energies can be tuned with small changes in surface composition and structure. So the study of those surfaces is of great scientific interest.

In our surface structure analysis of p($\sqrt{3} \times \sqrt{3}$)R30° -Bi/Pb on Ag(111), we found that the energetically most favourable adsorption geometry is the surface alloy structure. That means that a Bi or Pb atom replaces one top layer Ag atom per unit cell. The DFT calculations were done using VASP and PAW potentials. More detailed calculation parameters can be found in publications IV-VI. The adsorption energy was calculated by using a method where we let the surface with the preadsorbed atoms on the defined sites relax to the total energy minima. In Fig. 3.16 one can see the surface structure of p($\sqrt{3} \times \sqrt{3}$)R30° Pb-Ag(111). The places of atoms are calculated with VASP and the figure is plotted by using VMD. There is a very good agreement between the geometrical parameters extracted from LEED I-V and DFT analyses for both Ag/Bi Ag/Pb. However, in the case of Bi the DFT calculations can not find a difference between the surface alloy and the faulted surface alloy structures while the LEED analysis unambiguosly favour the unfaulted surface alloy (The faulted surface structure means that all atoms at the topmost layer are moved into hcp hollow sites). The possible reason why our DFT calculations fail to distinguish between the two structures is the use of the finite size of the slab (6 layers).

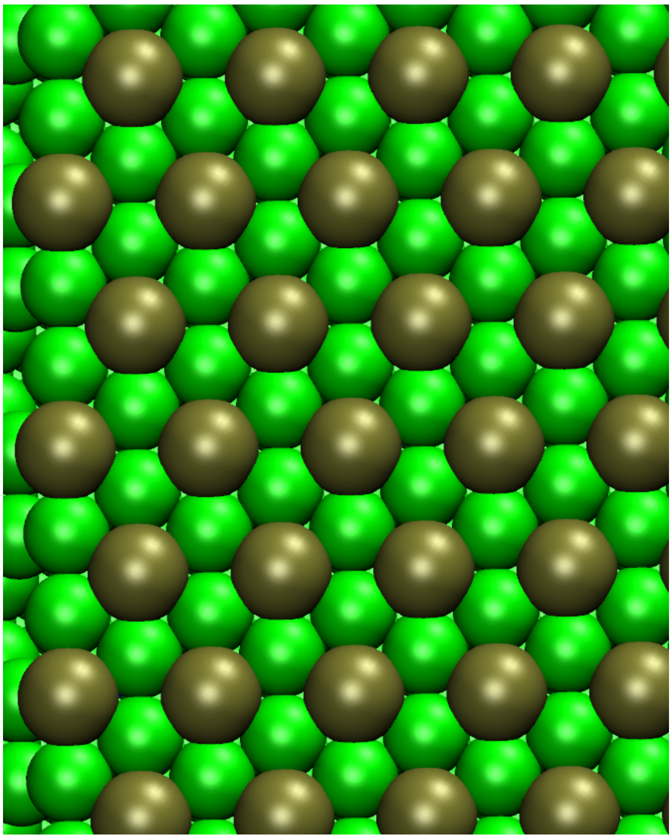

Figure 3.16: The surface structure of p($\sqrt{3} \times \sqrt{3}$)R30° Pb-Ag(111).

3.3 Sulphur adsorption on Au{110}: DFT and LEED study

In Publication III we studied sulphur adsorption on the reconstructed gold {110}-(1 × 2) surface. We also studied a surface structure of Au{110} with preadsorbed sulphur with the coverage of 0.13 ML. In section 3.2 we discuss the surface structures of the smooth surfaces. From this point we now move forvard and discuss a rather simple stepped surface. The methods we still use include VASP and the Barbieri/ Van Hove SATLEED packages. In this Publication we also use a less widely used method for the study of the adsorption of sulphur: We calculated 2-dimensional PES plots. S_2 molecules were deposited on the gold surface in a similar manner as in Ref. [77]. In many cases where the d-band metals act as catalysts, sulphur is an unwanted poison and its adsorption to the surface needs to be limited or controlled. For that purpose it is important to know the adsorption dynamics of sulphur atoms, molecules, and compounds. In this Publication one can see that 2-dimensional PES plots of the S_2 molecule can be calculated as in the case of 2-dimensional PES plots of the O_2 molecule. In Fig. 3.19 one can see an example of the 2-dimensional PES plots of the S_2 molecule approaching the gold {110} surface. The Au{110} surface is known to reconstruct to the missing-row structure. The structure has been studied by LEED and medium-energy-electron scattering methods in Refs [78] [79]. In Fig. 3.17 one can see the missing-row structure and the normal (110) structure. In the missing-row structure every second row of the topmost atoms are missing.

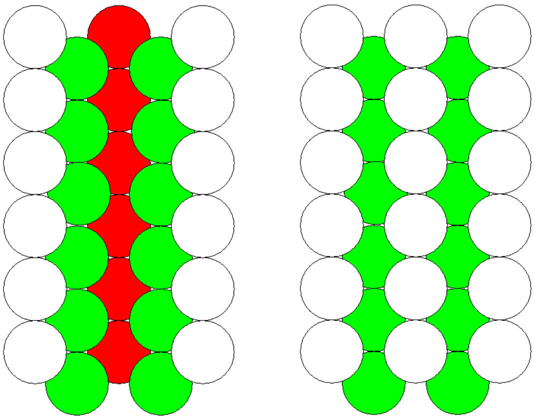

Figure 3.17: The missing-row structure and the nonreconstructed (110) structure.

With VASP we analyzed the surface with two ways: we calcutated 2-dimensional PES plots to the assumed adsorption sites and calculated the adsorption energy of one sulphur atom at the assumed adsorption sites. The adsorption energy was calculated by using a method where we let the surface with one preadsorbed sulphur on the defined site relax to the total energy minimum. This energy was compared to the energy of the relaxed clean surface and to the total energy of the S_2 molecule by using the following formula:

$$E_{\mathrm{ads}} = \frac{1}{N_{\mathrm{S}}} \times (E_{\mathrm{tot}} - E_{\mathrm{clean}} - \frac{N_{\mathrm{S}}}{2} \times E_{\mathrm{S}_2}), \tag{3.2}$$

where E_{tot} is the total energy of a relaxed Au/S supercell, E_{clean} is the total energy of the relaxed clean Au slab N_{S} is the number of the sulphur atoms and E_{S_2} is the total energy of an S_2 molecule. In Fig. 3.18 one can see the S_2 molecules orientation for the 2-dimensional PES plots, and calculated adsorption sites of sulphur atoms.

From the VASP calculations we found the S_2 molecules orientation 9 from Fig. 3.18 to be the energetically most favourable molecular adsorption site. However, with the dissociation barrier of about 1 eV, it is not a probable orientation for dissociation. The bond breaking is much more favourable after a rotation of 90 degrees to orientation 2. After the rotation the dissociation barrier is only about 0.4 eV. The most favourable atomic adsorption site was found to be the site number 3 in Fig. 3.18. Thus the S atoms are after dissociation on the best adsortion site. The same atomic adsorption site was also found to be the most favourable with the LEED method. Thus it gives more reliability to the results.

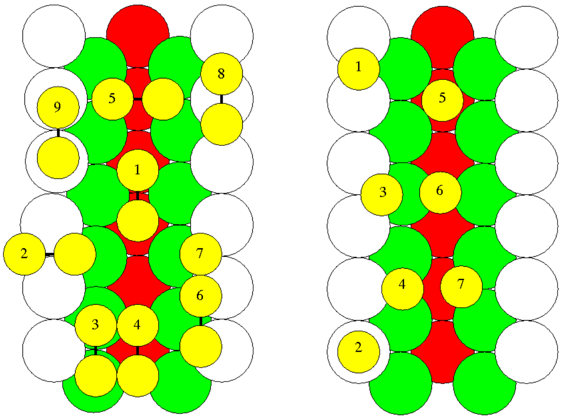

Figure 3.18: The S_2 molecule's orientation for the 2-dimensional PES plots (left), and calculated adsorption sites of sulphur atoms (right).

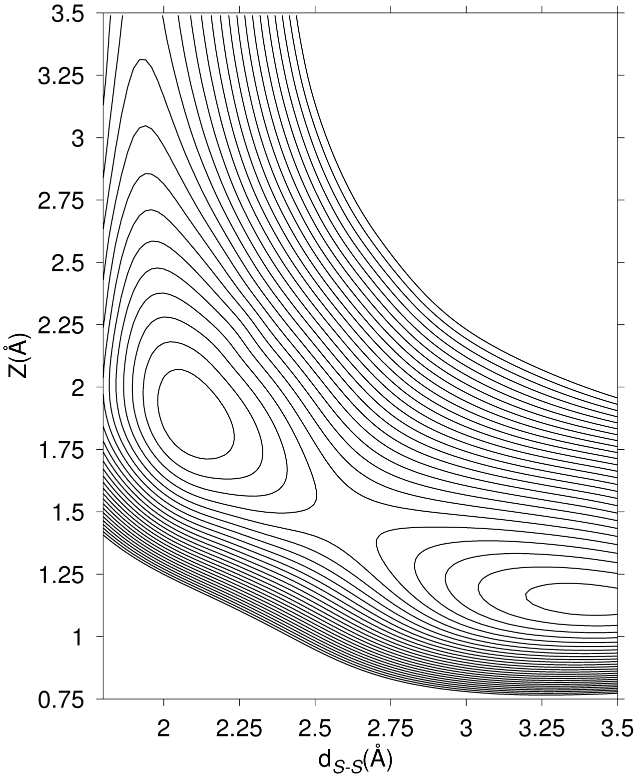

Figure 3.19: An example of calculated 2-D cuts of the PES on Au(110) surface with the S_2 molecule approaching the bridge site. The adsorption site of the molecule is the orientation 2 in figure 3.18. The contour spacing in the figure is 0.1 eV.

Chapter 4

Concluding remarks

As long as mankind has known metals, rust and corrosion have been a subject of amazement. Also in theoretical surface science these phenomena have been a very important topic of research, even if many other topics have emerged as the developement of science has progressed. These topics have also been an important part of this study. The study of oxidation has generated good specific results, which can be generalized to many similar cases. Also in the study of surface structure we have obtained good results. However, one of the most important accomplishments of this study has been the testing and comparison of the results of the VASP code. We have done it in the Publications, but also in Section 3.1, where we also add new aspects to the results of Publications I and II. In Puplication I we calculated the results by the SIESTA package. However, for Section 3.1 we have performed part of the calculations again with the VASP code in order use a complementary method to analyze the results. The VASP and SIESTA results agree well. Also the analyze of the molecular orbitals, calculated with VASP, gives compatible results with 2-dimensional PES plots calculated with SIESTA. In Publications III-VII we compare the VASP results to results calculated with LEED and there we find a very good agreement between the geometrical parameters extracted from LEED I-V and DFT analyses.

In Publications I and II we study the adsorption and dissociation of an oxygen molecule on the stepped Pd and Cu (211) surfaces and a smooth Pd(100) surface with S and O as preadsorbed atoms. As we assumed, we found that the stepped Cu and Pd (211) surfaces are very reactive, and the most reactive site is the hollow site of the (100) microfacet. At the smooth surface we found that the preadsorbed atoms affect the reactivity of the surface. This decrease of reactivity is not only a direct effect between the preadsorbed atoms and the oxygen molecule, but the preadsorbed atoms also affect the palladium atoms of the surface in a way that reduce the reactivity. Sulphur is found to have a stronger influence than oxygen. In Section 3.1 we discuss in more detail about the Publications and we also study the developement of the molecular orbitals of the oxygen molecule when the molecule approaches the defined sites of the defined surfaces. This developement of the molecular orbitals of the oxygen molecule can be compared to the devlopement of the molecular orbitals of the hydrogen molecule which are discussed in Section 2.4 and in References [9][10]. In Section 3.1 one can see that the oxygen molecule approaching the most reactive site does not form an antibonding type bond between the molecule and the surface. Also we found that the bond between the molecule and the surface is not only from the π^* orbital but the bond between the π^* orbital and the surface is stronger than bonds between the other orbitals and surfaces. Also because the π^* orbital is a molecular antibonding orbital the bond between the π^* orbital and the surface weaken the bond between the atoms in the molecule. However, this weakening is minor, because the molecule get only 0.8 extra electrons from the surface. In the case of the preadsorbed atoms when the oxygen molecule approaches the hollow site next to the preadsorbed atoms a σ type antibonding orbital arises between the molecule and the surface. The evolution of the molecular orbitals of the oxygen molecule that approaches a surface needs more investigation; this is left for future work.

In Publication III we study the adsorption of the S_2 molecule to a reconstructured Au(110) surface and the surface structure of S on the surface with coverage 0.13 ML. With VASP we analyzed the surface in two ways: we calculated 2-dimensional PES plots to the assumed adsorption sites and calculated the adsorption energy of one sulphur atom at the assumed adsorption sites. The PES calculations are a method that is less frequently used to calculate sulphur adsorption to the surface. However, the method yields information that can be used examine the first part of the formation of the surface structure. In this Publication we show that the 2-dimensional PES plots are an acceptaple method to study the adsorption of sulphur molecules. We also discovered a surface structure which is energetically the most favourable calculated with both the LEED and DFT methods.

In Publications IV-VII we study the surface sturcture of preadsorbed metal on metal surfaces. These studies give knowledge on the steps of thin film growth, which is important in certain high technology. Below one monolayer the coverage of a metal on a metal surface adds new intresting attributes to the surface properties. Charge density waves are a very special effect. Better knowledge of the surface structures of the defined materials yield information that is important when studying this phenomenon. This is only one example of the intresting phenomena that take place on the surface. Second example, which posseses great possibility to be the base of a new epochal technology, is the Rashba effect. Certain surface structures behave like 2-D electron gas with quantum confinemet leading to the Rashba effect. In Publications IV-VI we study two examples of this kind of surfaces: p$(\sqrt{3} \times \sqrt{3})$R30° Bi-Ag(111) and p($\sqrt{3} \times \sqrt{3}$)R30° Pb-Ag(111) surfaces. We study the surface structures by using two different methods: VASP and LEED. So we can get reliable results in order to study the Rashba effect.

Many details from little thigns have been clarified. However the work must go on, since one scientist's contribution is but a drop in a river. Almost all phenomena around us arise at the atomic level, so it is appropriate to conclude this work with the words of an ancient Greek philosopher. Democritus said “By convention hot, by convetion cold, but in reality atoms and void” and “In reality we know nothing, for the truth is in the depths” [80].

Bibliography

[1] M. Born and J. R. Oppenheimer, “Zur quantentheorie der molekaln,” *Ann. Physik.*, vol. 84, p. 457, 1927.

[2] H. Hellman, “Einführung in die Quantenchemie,” *Deuku, Leipzig*, 1937.

[3] R. P. Feynman, “Forces in molecules,” *Phys. Rev.*, vol. 56, p. 340, 1939.

[4] C. C. J. Roothaan, “New Developments in Molecular Orbital Theory,” *Rev. Mod. Phys.*, vol. 23, p. 69, 1951.

[5] P. W. Atkins and R. S. Friedman, “Molecular Quantum Mechanics,” *New York: Oxford University Press Inc.*, 1997.

[6] S. Gasiorowicz, “Quantum Physics,” *New York: John Wiley & Sons, Inc*, 1995.

[7] P. W. Atkins and J. de Paulo, “Atkins’ Physical Chemistry,” *New York: Oxford University Press Inc.*, 2002.

[8] J. P. Lowe, “Quantum Chemistry,” *New York: Academic Press, Inc*, 1978.

[9] B. Hammer and J. K. Nørskov, “Why gold is the noblest of all the metals,” *Nature*, vol. 376, p. 238, 1995.

[10] B. Hammer and J. K. Nørskov, “Electronic factors determining the reactivity of metal surfaces,” *Surface Science*, vol. 343, p. 211, 1995.

[11] R. Hoffmann, “A chemical and theoretical way to look at bonding on surfaces,” *Rev. of Mod. Phys.*, vol. 60, p. 601, 1988.

[12] B. Hammer, “Coverage dependence of N_2 dissociation at an N, O, or H precovered Ru(0001) surface investigated with density functional theory,” *Phys. Rev. B*, vol. 63, p. 205423, 2001.

[13] G. Kresse and J. Hafner, “Norm-conserving and ultrasoft pseudopotentials for first-row and transition metals,” *J. Phys. Condens. Matter*, vol. 6, p. 8245, 1994.

[14] G. Kresse and J. Furthmüller, “Efficiency of ab-initio total energy calculations for metals and semiconductors using a plane-wave basis set,” *Comput. Mat. Sci*, vol. 6, p. 15, 1996.

[15] G. Kresse and J. Furthmüller, “Efficient iterative schemes for ab-initio total energy calculations using a plane-wave basis set,” *Phys. Rev. B*, vol. 54, p. 11169, 1996.

[16] G. Kresse and J. Furthmüller, “From ultrasoft pseudopotentials to the projector augmented-wave method,” *Phys. Rev. B*, vol. 59, p. 1758, 1999.

[17] J. M. Soler, J. G. E. Artacho, J. J. A. García, P. Ordejón, and D. Sánchez-Portal, “The SIESTA method for ab initio order-N materials simulations,” *J. Phys. Condens. Matter*, vol. 14, p. 2745, 2002.

[18] D. Sánchez-Portal, P. Ordejón, E. Artacho, and J. M. Soler, “Density-functional method for very large systems with LCAO basis sets,” *Int. J Quantum Chem.*, vol. 65, p. 453, 1997.

[19] E. Artacho, D. Sánchez-Portal, P. Ordejón, A. García, and J. M. Soler, “Linear-scaling ab-initio calculations for large and complex system,” *Phys. Stat Sol. b*, vol. 215, p. 809, 1999.

[20] J. Junquera, D. Sánchez-Portal, and E. Artacho, “Numerical atomic orbitals for linear-scaling calculations,” *Phys. Rev. B*, vol. 64, p. 235111, 2001.

[21] E. Anglada, J. M. Soler, J. Junquera, and E. Artacho, “Systematic generation of finite-range atomic basis sets for linear-scaling calculations,” *J. Phys. Condens. Matter*, vol. 66, p. 205101, 2002.

[22] P. E. Blöchl, “Projector augmented-wave method,” *Phys. Rev. B*, vol. 50, p. 17953, 1994.

[23] H. Monkhorst and J. Pack, “Special pointa for brillouin-zone integrations,” *Phys. Rev. B.*, vol. 13, p. 5192, 1978.

[24] W. C. Herring, “A new method for calculating wave functions in crystals,” *Phys. Rev*, vol. 57, p. 1169, 1940.

[25] R. M. Martin, “Electronic Structure: Basic Theory and Practical Methods,” *Cambridge University Press, Cambridge*, 2004.

[26] J. Hafner, “Ab-Initio Simulations of Material Using VASP: Density-Functionl Theory and Beyound,” *J. Comput. Chem.*, vol. 29, p. 2004, 2008.

[27] P. Pulay, “Convergence acceleration of iterative sequences. the case of scf iteration,” *Chem. Phys. Lett.*, vol. 73, p. 393, 1980.

[28] P. Pulay, “Ab initio Calculation of Force Constants and Equilibrium Geometries,” *Molec. Phys.*, vol. 17, p. 197, 1969.

[29] L. H. Thomas, “The calculation of atomic fields,” *Proc. Cambridge Phil. Roy. Soc.*, vol. 23, p. 542, 1927.

[30] E. Fermi, “Un metodo statistico per la determinazione di alcune priorieta dell’atome,” *Rend. Accad. Naz. Lincei*, vol. 6, p. 602, 1927.

[31] W. Kohn, “Nobel Lecture: Electronic structure of matter - wave functions and density functionals,” *Rev. Mod. Phys.*, vol. 71, p. 1253, 1999.

[32] P. A. M. Dirac, “Note on exchange phenomena in the Thomas-Fermi atom,” *Proc. Cambridge Phil. Soc.*, vol. 26, p. 542, 1930.

[33] P.Hohenberg and W. Kohn, “Inhomogeneus electron gas,” *Phys. Rev.*, vol. 136, p. B864, 1964.

[34] E. Gross and R. Reizler, “Density Functional Theory,” *NATO ASI Series, Series B: Physics vol. 337, Plenum Press, New York*, 1995.

[35] W. Kohn and L. Sham, “Self-consistent equation including exhange and correlation effect,” *Phys. Rev.*, vol. 140, p. A1133, 1965.

[36] D. M. Ceperley and B. J. Alder, “Ground state of the electron gas by a stochastic method,” *Phys. Rev. Lett.*, vol. 45, p. 566, 1980.

[37] J. P. Perdew and A. Zunger, “Self-interaction correction to density-functional approximations for many-electron systems,” *Phys. Rev. B*, vol. 23, p. 5048, 1981.

[38] A. Groß, “Theoretical Surface Science: A Microscopic Perspective,” *Berlin, Springer*, 2003.

[39] D. C. Langreth and J. P. Perdew, “Theory of nonuinform electronic system. i. analysis of the gradient approximation and a generalized that works,” *Phys. Rev. B*, vol. 21, p. 5469, 1980.

[40] C. P. Langerth and M. J. Mehl, “Beyond the local density approximation in calculations of ground-state electronic properties,” *Phys. Rev. B*, vol. 28, p. 1809, 1983.

[41] A. D. Becke, “Density-functional exhange-energy approximation with correct asymptotic behavior,” *Phys. Rev. A*, vol. 38, p. 3098, 1988.

[42] J. P. Perdew, J. A. Chevary, S. H. Vosko, K. A. Jackson, M. R. Pederson, D. J. Singh, and C. Fiolhais, "Applications of the generalized approximation for exhange and correlation," *Phys. Rev. B*, vol. 48, p. 4978, 1993.

[43] J. P. Perdew, K. Burke, and M. Ernzerhof, "Generalized gradient approximation made simple," *Phys. Rev. Lett*, vol. 77, p. 3865, 1996.

[44] R. Car and M. Parrinello, "Unified Approach for Molecular Dynamics and Density-Functional Theory," *Phys. Rev. Lett.*, vol. 55, p. 2471, 1985.

[45] D. Wood and A. Zunger, "A new method for diagonalising large matrices," *J. Phys. A.*, vol. 18, p. 1343, 1985.

[46] J. Kollár, L. Vitos, B. Johansson, and H. Skriver, "Metal surfaces: Surface, step and kink formation energies," *Physica status solidi*, vol. 217, p. 405, 2000.

[47] A. Puisto, H. Pitkänen, M. Alatalo, S. Jaatinen, P. Salo, A. S. Foster, T. Kangas, and K. Laasonen, "Adsorption of atomic and molecular oxygen on Cu(100)," *Catalysis today*, vol. 100, p. 403, 2005.

[48] M. Alatalo, A. Puisto, H. Pitkänen, A. S. Foster, and K. Laasonen, "Adsorption dynamics of O_2 on Cu(100)," *Surf. Sci.*, vol. 600, p. 1574, 2006.

[49] M. Ahonen, M. Hirsimaki, A. Puisto, S. Auvinen, M. Valden, and M. Alatalo, "Adsorption dynamics of O_2 on Cu(100): The role of vacancies, steps and adatoms in dissociative chemisorption of O_2," *Chem Phys. Lett.*, vol. 456, p. 211, 2008.

[50] T. G. Slanger and P. C. Cosby, "O_2 spectroscopy below 5.1 eV," *J. Phys. Chem*, vol. 92, p. 267, 1988.

[51] C. S. Foote, "Free radicals in biology," *New York: Academic Press, Inc*, vol. vol. II, 1976.

[52] C. Schweitzer and R. Schmidt, "Physical Mechanisms of Generation and Deactivation of Singlet Oxygen," *Chemical Reviews*, vol. 103, p. 1685, 2003.

[53] A. Hellman, B. Razaznejad, and B. I. Lundqvist, "Trends in sticking and andsorption of diatomic molecules on the Al(111) surface," *Phys. Rev. B*, vol. 71, p. 205424, 2005.

[54] J. P. Perdew and Y. Wang, "Accurate and simple analytic representation of the electron-gas correlation energy," *Phys Rev B*, vol. 45, p. 13244, 1992.

[55] W. Tang, E. Sanville, and G. Henkelman, "A grid-based bader analysis algorithm without lattice bias," *J. Phys.: Condens. Matter*, vol. 21, p. 084204, 2009.

[56] E. Sanville, S. D. Kenny, R. Smith, and G. Henkelman, "An improved grid-based algorithm for bader charge allocation," *J. Comp. Chem.*, vol. 28, p. 899, 2007.

[57] G. Henkelman, A. Arnaldsson, and H. Jónsson, "A fast and robust algorithm for bader decomposition of charge density," *Comput. Mater. Sci.*, vol. 36, p. 254, 2006.

[58] L. Qi, X. Qian, and J. Li, "Near Neutrality of Oxygen Molecule Adsorbed on a Pt(111) surface," *Phys. Rev. Lett.*, vol. 101, p. 146101, 2008.

[59] W. Humphrey, A. Dalke, and K. Schulten, "VMD - visual molecular dynamics," *J. Molec. Graphics*, vol. 14, p. 33, 1996.

[60] F. Jona, "LEED crystallography," *J. Phys. C.*, vol. 11, p. 4271, 1978.

[61] M. A. V. Hove, W. Moritz, H. Over, P. Rous, A. Wander, A. Barbieri, N. Materer, U. Starke, and G. Somorjai, "Automated determination of complex surface structures by LEED," *Surf. Sci. Rep.*, vol. 19, p. 191, 1993.

[62] H. Yoshida, A. Okamoto, S. Mizuno, and H. Tochihara, "Structure determination of the Cu(0 0 1)–c(4× 4)-Sn surface by low-energy electron diffraction," *Surf Sci.*, vol. 604, p. 535, 2010.

[63] Z. Zhang and M. G. Lagally, "Atomic processes in the early stages of thin-film growth," *Science*, vol. 276, p. 377, 1997.

[64] R. E. Peierls, "Quantum theory of solids," *Clarendon, Oxford*, 1955.

[65] W. L. McMillan, "Microscopic model of charge-density waves in 2H-TaSe$_2$," *Phys. Rev. B*, vol. 16, p. 643, 1977.

[66] J. Lallo, L. Goncharova, B. Hinch, S. Rangan, R. Bartynski, and D. Strongin, "Structural studies of sub monolayer Sn/Cu(0 0 1) structures," *Surf. Sci.*, vol. 602, p. 2348, 2008.

[67] F. Meier, H. Dil1, J. Lobo-Checa, L. Patthey, and J. Osterwalder, "Quantitative vectorial spin analysis in angle-resolved photoemission: Bi/Ag(111) and Pb/Ag(111)," *Phys. Rev. B*, vol. 77, p. 165431, 2008.

[68] C. R. Ast, A. E. J. Henk, L. Moreschini, M. C. Falub, D. Pacilé, P. Bruno, K. Kern, and M. Grioni, "Giant Spin Splitting Through Surface Alloying," *Phys. Rev. Lett.*, vol. 98, p. 186807, 2007.

[69] K. He, T. Hirahara, T. Okuda, S. Hasegawa, A. Kakizaki, and I. Matsuda, "Spin Polarization of Quantum Well States in Ag Films Induced by the Rashba Effect at the Surface," *Phys. Rev. Lett.*, vol. 101, p. 107604, 2008.

[70] S. Davidon and M. Steslicka, “Basic Theory of Surface States,” *Oxford unversity press, New York*, 1992.

[71] E. Bertel and M. Donath, “Electronic Surface and Interface States on Metallic Systems,” *Oxford unversity press, New York*, 1992.

[72] T. Hsieh, T. Miller, and T. Chiang, “Probing the Wave Function of a Surface State in Ag(111): A New Approach,” *Phys. Rev. Lett.*, vol. 55, 1985.

[73] Y. A. Bychkov and E. I. Rashba, “Properties of a 2D electron gas with lifted spectral degeneracy,” *JETP Lett.*, vol. 39, p. 78, 1984.

[74] O. Krupin, G. Bihlmayer, K. Starke, S. Gorovikov, J. E. Prieto, K. Döbrich, S. Blügel, and G. Kaindl, “Rashba effect at magnetic metal surfaces,” *Phys Rev B*, vol. 71, p. 201403, 2005.

[75] E. I. Rashba and F. Tverd *Sov. Phys. Solid State*, vol. 2, p. 1109, 1960.

[76] S. A. Wolf, D. D. Awschalom, R. A. Buhrman, J. M. Daughton, M. L. R. S. von Molnár, A. Y. Chtchelkanova, and D. M. Treger, “Spintronics: A Spin-Based Electronics Vision for the Future,” *Science*, vol. 294, p. 1488, 2001.

[77] S. A. Krasnikov, G. Hughes, and A. A. Cafolla, “Sulphur overlayers on the Au(1 1 0) surface: LEED and TPD study,” *Surf. Sci*, vol. 601, p. 3506, 2007.

[78] W. Moriz and D. Wolf, “Multilayer distortion in reconstructed (110) surface of Au,” *Surf. Sci. Lett.*, vol. 163, p. L655, 1985.

[79] M. Copel and T. Gustafsson, “Structure of Au determined with medium-energy-ion scattering,” *Phys. Rev. Lett.*, vol. 57, p. 723, 1986.

[80] C. C. W. Taylor, “The Atomists Leucippus and Democritus,” *Unversity of Toronto Press, Toronto*, 1999.

Publication I

M. Lahti, N. Nivalainen, A. Puisto, M. Alatalo

"O_2 dissociation on Pd(211) and Cu(211) surfaces" Reprinted from Surface Science, 601, 3774 ©(2007) with permission from Elsevier.

Available online at www.sciencedirect.com

ScienceDirect

Surface Science 601 (2007) 3774–3777

SURFACE SCIENCE

www.elsevier.com/locate/susc

O_2 dissociation on Pd(2 1 1) and Cu(2 1 1) surfaces

M. Lahti *, N. Nivalainen, A. Puisto, M. Alatalo

Lappeenranta University of Technology, Department of Electrical Engineering, P.O. Box 20, FIN-53851, Finland

Abstract

We have performed *ab initio* Density Functional Theory (DFT) based calculations to observe the reactivity of the Pd(2 1 1) and Cu(2 1 1) surfaces towards O_2. In order to properly address the adsorption dynamics, the static potential energy surface calculations have been complemented with first principles molecular dynamics calculations, which reveal interesting steering effects that complicate the dissociation dynamics. We have found that on both surfaces the step microfacets are very reactive and the dissociation of the O_2 molecule at room temperature occurs mostly on those sites.

Keywords: Adsorption; Copper; Density functional calculations; Defects; Molecular dynamics; Oxidation; Palladium

1. Introduction

The dissociation of O_2 on metal surfaces is the first reaction on many catalytic processes varying from low temperature water gas shift to the oxidation of carbon monoxide. The reactivity of stepped surfaces is generally considered superior over the low index surfaces, because of the larger amount of broken bonds on stepped surfaces creating an upshift of the d-band density of states [1,2]. In addition, the broken symmetry of the stepped surfaces leads to new geometrical configurations [3] that are not present for the adsorbants on smooth surfaces, thus affecting the adsorption and dissociation processes. These phenomena have led to a great deal of theoretical and experimental research effort concentrated on studying the reactivity of steps and the adsorption of diatomic molecules on stepped surfaces.

We chose to compare Cu and Pd surfaces because currently, Cu is a very widely used metal with somewhat average catalytic properties and, on the other hand, Pd being chemically very reactive is a material of great technological interest. Furthermore, both materials have very similar valence electron structure with the Pd d-band slightly closer to the Fermi level, making these materials very interesting to compare.

There exists several studies concerning the stability of different step surfaces composed of different transition metals. One of the perhaps most thorough study is the one by Kollár et al. [4], who have investigated the stability of several different step surfaces. They compared their *ab initio* results to a simpler nearest neighbor model and found that the trends of the stability of stepped surfaces can be well explained by the broken bond model. For Cu and Pd they found that (1 0 0) × (1 1 1) (in the present study the (2 1 1) surface represents this kind of cut) is a very stable cut giving confidence on the practical relevance of these calculations.

The adsorption of diatomic molecules on the Pd(2 1 1) surface has been studied by several authors. Hammer and Nørskov performed density functional calculations for nitric oxide on Pd(2 1 1) [5] to find the stable chemisorption sites. They found that at low coverages the three fold hollow sites over the (1 1 1) terrace are favoured, while the most favourable site for NO is the step bound configuration where the N is bound to the bridge site on the step edge, and the O points away from the surface. A comparative DFT study concerning the CO adsorption on Ni(2 1 1), Pt(2 1 1), and Pd(2 1 1) was performed by Orita et al. [6], who observed that the adsorption site preference

---

* Corresponding author.
E-mail address: matti.lahti@lut.fi (M. Lahti).

0039-6028/$ - see front matter © 2007 Elsevier B.V. All rights reserved.
doi:10.1016/j.susc.2007.04.052

varies a great deal depending on the substrate material. Their calculations showed that the preferable adsorption site on the Ni and Pd surfaces is the bridge site on the step edge, whereas in the case of Pt the most favourable site was the top site on the step edge with only rather weak site selectivity. In this case, as the so-called d-band model by Hammer and Nørskov [2] suggests the most reactive adsorbate was Pt.

In the present paper we have compared two different materials, Cu and Pd, as catalysts for the dissociation of O_2 in the purpose to establish more information on the properties of materials that effect the process. We have chosen to perform the calculations on a (2 1 1)-stepped surface, because of the well known fact that the stepped metal surfaces are more reactive than the smooth ones. On the other hand, this surface is quite simple and easy to construct, with quite high density of steps making it a suitable candidate for periodic supercell calculations.

2. Computational methods

To perform the calculations we used the Spanish Initiative for Electronic Structure with Thousands of Atoms (SIESTA) package with numerical atomic orbital basis [7,8]. We used Troullier–Martins type of pseudopotentials [9] with Generalized Gradient Approximation (GGA) of Perdew–Burke–Ernzerhof flavor [10]. In the pseudopotentials we had the valence configurations of $4d^9\ 5s^1$, $3d^{10}\ 2s^1$ and $2s^2\ 2p^4$ for Pd, Cu, and O, respectively. We used a standard double zeta basis with polarization orbitals for Pd with the energy shift of 15 meV. For O and Cu we used optimized basis including d-orbitals for O to account for the polarization effects caused by the surface. In the simulation supercell we had 12 atomic layers with nine surface atoms with the total amount of 36 atoms in the simulation cell. We applied Monkhorst-Pack mesh of $8 \times 8 \times 1$ resulting in 40 irreducible k-points in all of the simulations. The quantum molecular dynamics calculations were performed with the following parameters: the surface temperature was fixed to 300 K using the Nosé thermostat [11,12], the approaching molecule was assigned with the kinetic energy of 25 meV towards the surface, and the ionic moves were performed with the interval of 1 fs.

3. Results

For both materials, we calculated two dimensional cuts of the potential energy surface (PES) for trajectories shown in a schematic map in Fig. 1. In the following subsections the PES figures are referenced according to the numbering scheme used in the figure.

3.1. Pd(2 1 1)

We wanted to map out the reaction paths of the O_2 dissociation on the surface. The easiest and by far the most popular way to do this is to calculate two dimensional cuts

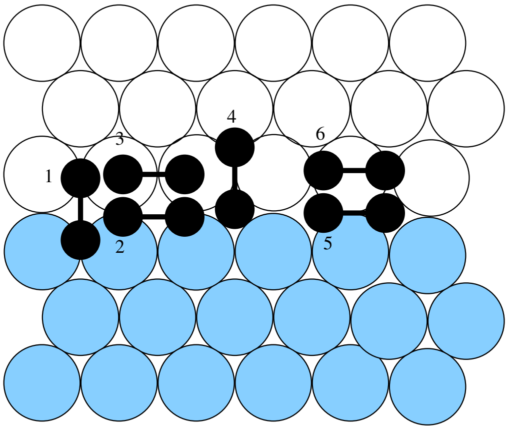

Fig. 1. The calculated trajectories shown as a schematic map of the step edge. In the figure black white and grey circles represent oxygen, Pd atoms on upper terrace, and Pd atoms on lower terrace, respectively. On the trajectories (1), (2), and (5) the molecules approach the surface along the normal vector of (1 0 0) microfacet, whereas on the rest of the trajectories the molecule approaches the surface along the normal vector of the (1 1 1) terrace.

through the six dimensional potential energy surface and compare the calculated trajectories to find the dissociative sites, and the deep wells of the potential energy surface. We have calculated several trajectories for O_2 on the sites with the highest symmetry. The PES figures corresponding to the calculated trajectories are shown in Fig. 2. The PES figures reveal that the deepest molecular adsorption site is on the step edge at the top-bridge-top site (which corresponds to 3 in the current numbering scheme) with the depth of 1.9 eV. On the other hand, the dissociation barrier through that trajectory is the highest of the calculated trajectories. The most dissociative site is the hollow site at the (1 0 0) microfacet (1 in the schematic figure), which also has a rather intense downhill at the entrance channel showing the tendency to draw the incoming molecules towards the trajectory. The step edge bridge site (4) and the microfacet's bridge site (5) show only a small barrier for the dissociation, but the trajectories lie so high in the energy scale that already at the height of 2.5 Å the incoming molecules have a strong tendency to be steered towards more favourable trajectories such as (1), (2) and (3). Also, the step edge top site (6) has a strong minimum at the height of 2 Å which could be interpreted to be a molecular adsorption site, but as the depth of the minimum in the energy scale is smaller than the one on trajectory (1) it is not the global minimum on the surface and therefore, the incoming molecules will experience a strong steering towards the sites lower in energy.

We performed quantum mechanical molecular dynamics (MD) calculations starting from several different initial orientations to get a feeling of the intensity of the steering involved and, on the other hand, to complement the static

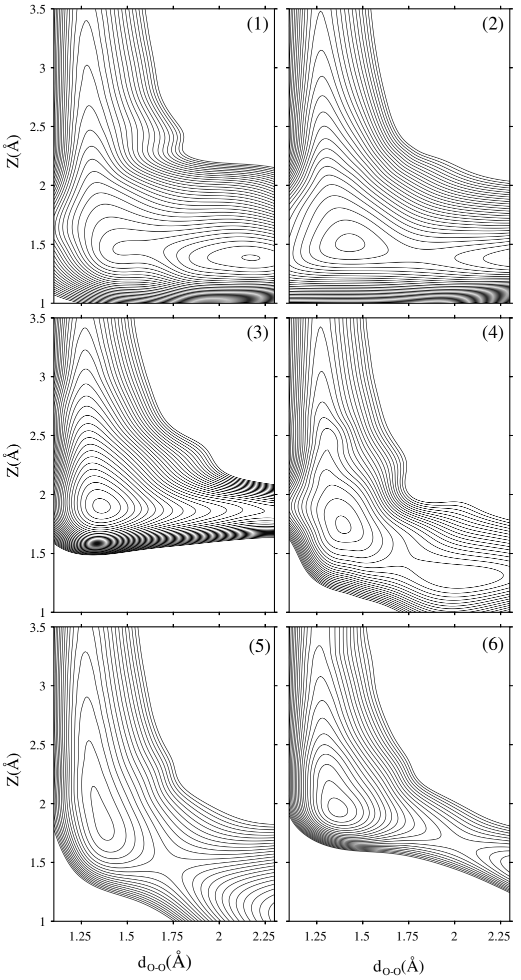

Fig. 2. The calculated 2-D cuts of the PES on Pd(2 1 1) as a function of the O_2 bond length $d_{O–O}$ and the height of the molecule z from the surface. The numbering scheme corresponds to that in Fig. 1. The contour spacing is 0.1 eV.

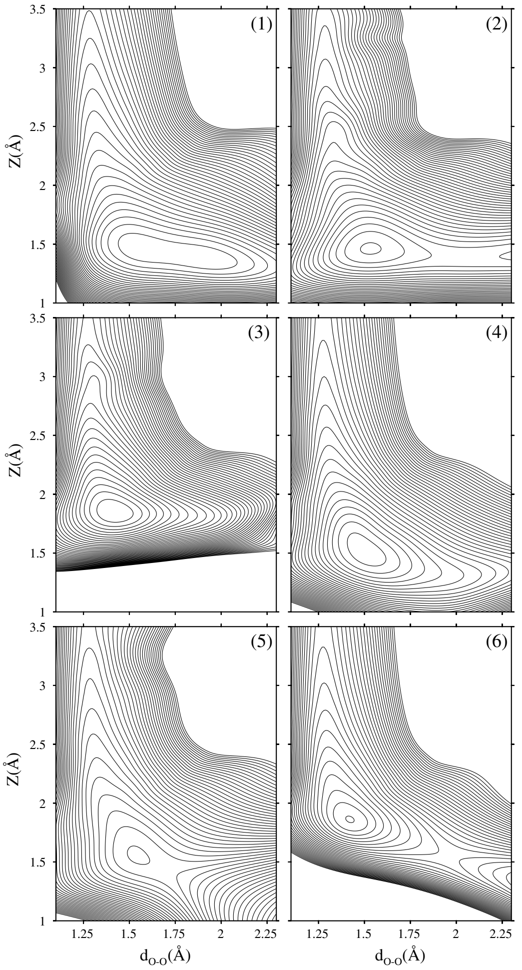

Fig. 3. The calculated PES experienced by O_2 approaching the Cu(2 1 1) surface. The order of the plots is consistent with the ordering of Fig. 2. The contour spacing is 0.1 eV.

PES calculations which might miss some important trajectories as it is impossible to calculate the whole six dimensional PES using just the static two dimensional calculations. As suggested by the results of the PES calculations, we chose the trajectories (1)–(4) for the MD calculations. There was an interesting distortion on the route of the molecule starting from initial position (1). At the distance of 1.8 Å the molecule turned parallel to the (1 1 1) terrace over the hcp site and started approaching the hollow site of the (1 0 0) microfacet with the molecular axis pointing towards the hollow site. As the molecule entered the hollow site, it turned parallel to the (1 0 0) microfacet, the position corresponding to the calculated PES trajectory (1), from which it spontaneously dissociated and the oxygen atoms adsorped to the fcc and hcp sites of the (1 1 1) terrace. The calculations starting from the initial orientations (2), (3) and (4) all ended up to the molecular state over the bridge site on the step edge (3). Interestingly, the molecule starting from orientation (2) also drifted over orientation (1) without dissociating, but this gives no reason to suspect that this should happen if the calculation is reperformed with different initial velocities for the molecule, as the dissociating trajectory over site (1) is very sensitive to the orientation of the molecule. Judging by the molecular dynamics trajectories the molecular adsorption site (3) shows to be very attractive for the molecules, whereas the hollow site (1) acts as dissociative center while being almost as attractive as sites (2) and (3). From the MD calculations one can also notice that there is no barrier for the molecule to move from site (2) to site (3).

3.2. Cu(211)

To compare Cu and Pd, we performed PES calculations also for O_2 approaching Cu(211) through the same trajectories as we calculated in the case of Pd(211). The PES plots are shown in Fig. 3. When looking at the PES figures one very noticeable feature for almost all the plots is the fact that on every site there exists an appreciable downhill in energy scale at the entrance channel. As in the case of the Pd surface, the (100)-microfacet's hollow site appears to be the most dissociative with only small late barriers in both directions (trajectories (1) and (2)). The step edge bridge sites ((3) and (4)) are very attractive sites, but the dissociation is prohibited with somewhat large late barrier indicating a tendency for steering. The (100)-microfacet's bridge (5) site shows up also as quite dissociative, whereas the step edge top site (6) is less attractive and has larger barrier in the late channel. While comparing the energetics of each site as a function of the distance from the surface, we see that the most attractive sites are the four fold hollow site on the (100)-microfacet (1) and the bridge site on the step edge (3) as was the case with the Pd(211) surface. This will naturally affect the approaching molecules by giving them a strong tendency to steer from the less attractive sites towards these two trajectories. The most favourable molecular site is the one over the microfacet's hollow site (2) with the adsorption energy of 1.9 eV.

4. Conclusions

On both Pd(211) and Cu(211) surfaces we see no early barrier for molecular sticking and they appear highly attractive for the incoming O_2 molecules. Both Pd and Cu exhibit deep molecular minima and low (in some sites nonexisting) energy barriers for the dissociation. On both surfaces the O_2 molecule favours the (100) microfacet's hollow sites over the (111) terrace sites. On the (211) surface the step edge is not particularly reactive, but the edge enhances the reactivity of the (100) microfacet compared to the smooth (100) surface [13] regardless of the material. We have gathered the calculated molecular adsorption energies and barriers for the dissociation in Table 1. The results should also be compared to the results of the smooth (111) surface [14,15], where the dissociation is prohibited by intermediate barriers and rather weak precursor sites are found.

Table 1
The calculated dissociation barriers and molecular adsorption energies for O_2 on Pd(211) and Cu(211)

Surface	Site	E_{ads} (eV)	Barrier (eV)
Pd(211)	1	1.3	NA
	2	1.6	0.2
	3	1.9	ND
	4	1.0	0.5
	5	0.4	0.5
	6	1.0	1.3
Cu(211)	1	1.6	NA
	2	1.9	0.3
	3	1.5	ND
	4	1.4	ND
	5	1.0	0.1
	6	1.0	0.9

In the table, NA denotes nonactivated dissociation and ND a nondissociative trajectory (*i.e.* one with a prohibitively large barrier).

One of the reasons that affects the difference seen in trajectory (1) (the hollow site of the (100) microfacet) is the fact that Pd has a larger lattice constant, which has the effect that as the O atoms reach the bridge sites, the bond between the O atoms is already broken and therefore there is no barrier in the late channel. If we consider the situation of the same trajectory on Cu, the O atoms still have stronger interaction between each other at the bridge sites raising the energy as the bondlength is further increased. On the step surfaces the steering effects are even more pronounced than on the smooth surfaces, and thus molecular dynamics is a very important tool for mapping out the most attractive sites and the various adsorption routes which are in many cases very complicated. On the whole, the (211) surface of either material is very reactive compared to any smooth surface of the same material.

Acknowledgements

We acknowledge the generous computer resources of CSC – Scientific Computing Ltd., Espoo, Finland. This work has been partly supported by TEKES through the SURFOX program. We also acknowledge the support of the Finnish Cultural Foundation.

References

[1] B. Hammer, J.K. Nørskov, Surf. Sci. 343 (1995) 211.
[2] B. Hammer, J.K. Nørskov, Nature 376 (1995) 238.
[3] B. Hammer, O.H. Nielsen, J.K. Nørskov, Catal. Lett. 46 (1997) 31.
[4] J. Kollár, L. Vitos, B. Johansson, H.L. Skriver, Phys. Stat. Sol. B 217 (2000) 405.
[5] B. Hammer, J.K. Nørskov, Phys. Rev. Lett. 79 (1997) 4441.
[6] H. Orita, N. Itoh, Y. Inada, Surf. Sci. 571 (2004) 161.
[7] P. Ordejón, E. Artacho, J.M. Soler, Phys. Rev. B 53 (1996) R10441.
[8] J.M. Soler, E. Artacho, J.D. Gale, A. Garcia, J. Junquera, P. Ordejón, D. Sánchez-Portal, J. Phys.: Condens. Matter 14 (2002) 2745.
[9] N. Troullier, J.L. Martins, Phys. Rev. B 43 (1991) 1993.
[10] J.P. Perdew, K. Burke, M. Ernzerhof, Phys. Rev. Lett. 77 (1996) 3865.
[11] S. Nosé, J. Chem. Phys. 81 (1984) 511.
[12] S. Nosé, Mol. Phys. 52 (1984) 255.
[13] M. Alatalo, S. Jaatinen, P. Salo, K. Laasonen, Phys. Rev. B 70 (2004) 245417.
[14] K. Honkala, K. Laasonen, J. Chem. Phys. 115 (2001) 2297.
[15] Y. Xu, M. Mavrikakis, Surf. Sci. 494 (2001) 131.

Publication II

M . Lahti, A. Puisto, M. Alatalo, T.S. Rahman ”The role of preadsorbed sulphur and oxygen in O_2 dissociation on Pd(100)“ Reprinted from Surface Science, 602, 3660 ©(2008) with permission from Elsevier.

Surface Science 602 (2008) 3660–3666

Contents lists available at ScienceDirect

Surface Science

journal homepage: www.elsevier.com/locate/susc

The role of preadsorbed sulphur and oxygen in O_2 dissociation on Pd(100)

M. Lahti [a,*], A. Puisto [a], M. Alatalo [a], T.S. Rahman [b]

[a] *Department of Electrical Engineering, Lappeenranta University of Technology, P.O. Box 20, FIN-53851, Lappeenranta, Finland*
[b] *Department of Physics, University of Central Florida, Orlando, Florida 32816, USA*

ARTICLE INFO

Article history:
Received 18 January 2008
Accepted for publication 16 September 2008
Available online 1 October 2008

Keywords:
Adsorption
Density functional calculations
Oxidation
Molecule-solid reactions
Palladium
Sulphur

ABSTRACT

We have performed a density functional study for the poisoning of oxidation reaction of the Pd(100) surface by preadsorbed sulphur and oxygen. We find that the mechanism for this effect is due to (i) the physical blocking of the reactive sites, (ii) Coulombic charging caused repulsion between the incoming molecule and the poison, and (iii) the Pauli repulsion caused by the mixing of the electronic states of O_2 and the preadsorbents. The strength of the mechanisms (ii) and (iii) vary between the preadsorbed species. In addition, we have studied the effect of sulphur and oxygen coverage dependence on the poisoning of the dissociation of O_2. It is also observed that preadsorbed sulphur affects the electronic structure of the metal atoms only locally and has therefore only a small effect on molecules adsorbing to the clean parts of the surface.

1. Introduction

During the recent years, lot of work has been devoted to the study of the reactivity of metallic surfaces. Most often the driving force behind these studies has been the will to understand catalysis, which is used abundantly in modern technology. On the other hand, unwanted phenomena such as corrosion also depend on the reactivity of the materials used. In both cases, the key to the improvement of the process by either enhancing the desired reaction or suppressing the harmful one is the detailed understanding of the reactions on the atomistic level. From the computational point of view this knowledge can be obtained using first principles calculations which provide information on both the atomic configurations and the details of the electronic structure.

Sulphur is a well-known poison, which has a harmful effect, for example, in catalytic converters used in cars. Several earlier studies have been devoted to the poisoning action of sulphur on Pd surfaces [1–4]. Most of the computational studies have addressed the sulphur induced modification of the surface electronic structure and its effect on the reactivity. Also model reactions such as the dissociation of hydrogen molecules have been considered [2,5]. Pd(111) has already been shown to be reactive towards O_2 dissociation [6], a reaction which has direct consequences for catalysis. To our knowledge the effect of sulphur or preadsorbed oxygen on O_2 dissociation on Pd(100) has been studied neither experimentally nor theoretically. Such data, however, exists for some other metallic surfaces. For instance, Arabczyk et al. found that oxygen sticking on the Fe(111) surface decreases with increasing sulphur coverage and that the effect of sulphur is much larger than that of the preadsorbed oxygen [7]. In the case of Cu(100), preadsorbed oxygen has been shown to be clearly repulsive towards the O_2 molecules, leading to a large reduction of the sticking coefficient at the saturation coverage [8]. A similar effect has been observed for Fe(110) whereas on Fe(100) the effect of preadsorbed oxygen on the oxygen sticking is small [9]. In contrast, on the reconstructed Au(111) surface the preadsorbed oxygen has been shown to *enhance* O_2 dissociation [10].

In earlier works, several details of the poisoning effect of sulphur have been addressed in the cases of, e.g. Pt and Rh. For instance, the validity of the *d*-band model has been questioned in the case of Pt(111) and Pt_3Ni(111) surfaces [11]. Likewise, it has been shown by Zhang et al. that the poisoning effect of sulphur on the CO methanation reaction on Rh(111) is unlikely to be long-ranged [12]. Moreover, the charge transfer between S and the surface metal atoms has been discussed in the case of Pt(111) [13]. However, all these details depend on the surface reaction in question and the general understanding of trends is still lacking. Therefore, in order to gain more generic understanding, it is useful to address these details in the case of a yet unstudied surface reaction such as O_2 dissociation on Pd(100). In a similar way, the saturation of the oxygen dissociation depends on not only the material but also surface orientation, as shown e.g. by Blonski et al. in the case of O_2 on Fe(100) and Fe(110) [9].

In this paper we present results for the effect of preadsorbed sulphur and oxygen on the dissociation of O_2 molecules on Pd(100). We have used first principles methods to calculate the energetics of the incoming O_2 molecules. In particular, we have

---

[*] Corresponding author.
E-mail address: lahti@lut.fi (M. Lahti).

0039-6028/$ - see front matter © 2008 Elsevier B.V. All rights reserved.
doi:10.1016/j.susc.2008.09.034

calculated two-dimensional cuts of the full six-dimensional potential energy surface (PES) which yield information on the possible dissociation and, furthermore, the poisoning effect caused by sulphur. On Pd(100) surface we address the S coverage dependence by performing calculations for an isolated S atom on the surface representing low coverage, and for the p(2×2) and c(2×2) structures corresponding to 0.125, 0.25 and 0.5 monolayer coverage, respectively. For comparison, we performed corresponding calculations for preadsorbed oxygen at the same coverages as for sulphur. As far as the trends in the dissociation energy vs. sulphur and oxygen concentration are concerned, our results qualitatively agree with the above mentioned experimental findings for other O_2/metal systems.

The rest of this paper is organized as follows. In the next Section, we describe the details of the computational methods used. Section 3 contains the results and the discussion of the PES calculations and the calculations for the electronic structure, needed for the interpretation of the PES. Finally, our conclusions are presented in Section 4.

2. Computational details

The static calculations for total energies were performed using the Vienna ab-initio simulation package (VASP)[14–17] including the projector augmented wave (PAW) [18] potentials. We applied kinetic energy cut-off of 400 eV for the plane waves. For the exchange-correlation potential we employed the generalized gradient approximation (GGA) of the Perdew–Wang 91 (PW91) flavor [19].

Due to their heavy computational burden, the first principles molecular dynamics (MD) calculations were carried out using the Spanish Initiative for Electronic Simulations with Thousands of Atoms (SIESTA) [20–24] package. Instead of planewaves, it applies Numerical Atomic Orbitals (NAOs) for the basis functions therefore reducing the computational demand, making it possible to do longer MD runs. Unfortunately, it also reduces the accuracy. In slab calculations, where one has a lot of empty space over the slab this turns out to be a very efficient way. A comparison of the results produced by SIESTA and VASP in the case of O_2 on Cu(100) can be found at Ref. [25]. Even though the differences in the adsorption energies and dissociation barriers can be of the order of 0.1 eV, the qualitative behaviour remains the same regardless of the program used. We applied Troullier–Martins [26] type of pseudopotentials to describe the potential caused by the nuclei and the core electrons together with GGA of Perdew–Burke–Ernzerhof (PBE) [27] flavor. The PBE functional is an improved parametrization of PW91 and the two functionals yield similar results. In the pseudopotentials we had the valence configurations of $4d^9\,5s^1$ and $2s^2\,2p^4$ for Pd and O, respectively. We applied a standard double zeta basis with polarization orbitals for Pd with the energy shift of 15 meV. For O we used optimized basis including d-orbitals for O to account for the polarization effects caused by the surface. Eventhough two different programs have been used, this approach does not lead into inconsistencies since the results of the two programs are never compared with each other in the same context.

Within both methods we utilized a Monkhorst–Pack [28] special k-point sampling with the mesh of $8 \times 8 \times 1$ to sample the first Brillouin-zone. While calculating the two-dimensional potential energy surface (PES) cuts, surface atoms were kept frozen (frozen substrate approximation). The PES's were constructed by varying the O_2 intramolecular bond length and the distance from the surface and calculating the total energy. In the slab calculations we had four layers with eight atoms per layer resulting in 32 Pd atoms per supercell. During the MD calculations the temperature was fixed to 300 K and controlled using the Nosé thermostat. The total runtime for each MD run varied from 400 to 900 fs. The d-band centers were calculated as averages of the local densities of states, localized on single atoms. The atoms in question are indicated in the caption of Fig. 4 and the corresponding discussion.

3. Results and discussion

3.1. Clean Pd(100)

To address the poisoning effect of S on O_2 dissociation on Pd(100), it is important to understand the behaviour of O_2 on the clean surface. We performed PES and first principles molecular dynamics calculations for several trajectories for O_2 on Pd(100). The PES's for trajectories depicted in Fig. 1 are presented in Fig. 2. The most stable site for O_2 adsorption is over the four fold hollow site. Particularly stable is the bridge-hollow-bridge (b-h-b) configuration, which shows a small energy barrier for the dissociation close to the surface. Eventhough observed in the PES, the existence of such barrier is not certain, due to the frozen substrate approximation used in the calculations. Then again, our molecular dynamics calculations also showed trapping of molecules in the b-h-b configuration close to the surface. Moreover, we tested the validity of the approximation by performing a similar PES calculation with the frozen molecule approximation (see Fig. 3) allowing full relaxations for metal atoms, except for the bottom most layer, for each molecular bond length and distance. The two results (frozen substrate and frozen molecule shown in Figs. 2a and 3), which are considered as the upper and lower bounds for the dissociation barrier showed only negligible difference in the barrier height.

We observed dissociation of O_2 through the most stable (h-b-h) configuration also in the MD calculations. Our limited amount of MD trajectories only showed dissociation for the molecules that drifted from the hollow-top-hollow (h-t-h) to the b-h-b configuration. The reason for this was the fact that the molecules starting from the b-h-b configuration could not convert their translational energy to dissociation energy effectively enough. A similar steric hindrance effect has been observed for example for O_2 on Pt(111) [29]. The molecules starting from the h-t-h configuration show a PES shape that is more favourable for the translational to vibrational energy transition, because the bend in the PES is less steep than for the b-h-b, and therefore the molecules that end up drifting from the h-t-h configuration to the b-h-b configuration have enough vibrational energy to overcome the transition state barrier, and thus dissociate. In any case, these results indicate the sticking of close to unity for O_2 on the Pd(100) surface, because the adsorption energy of the molecule is higher for the molecular orientation than the dissociation energy making the dissociation process favoured over the desorption.

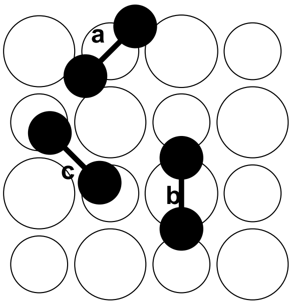

Fig. 1. PES trajectories for the clean Pd(100) shown as a schematic plot.

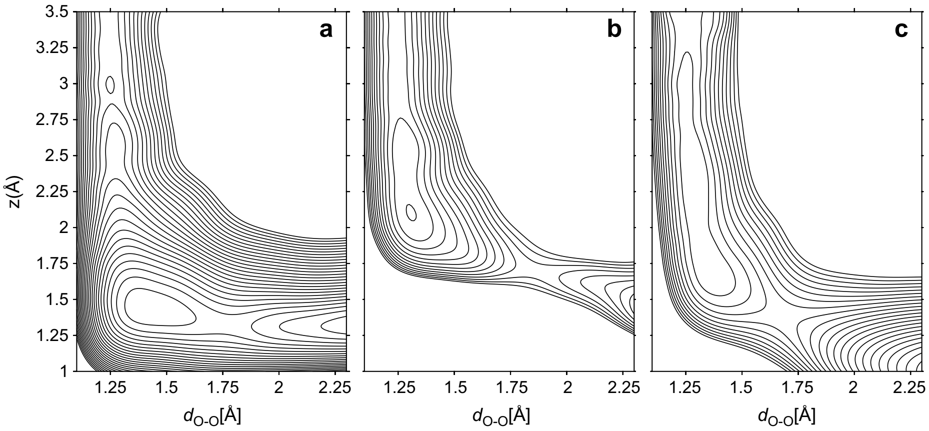

Fig. 2. The calculated PES plots for the clean Pd(100), (a) bridge-hollow-bridge (b-h-b), (b) hollow-top-hollow (h-t-h), and (c) hollow-bridge-hollow (h-b-h) configurations. None of the trajectories have energy barriers in the entrance channel indicating non-activated adsorption. The b-h-b trajectory has a late barrier of 0.1 eV and a sharp bend near the surface (see the discussion in the text). The contour line separation is 0.1 eV.

3.2. S/Pd(100)

On the Pd(100) surface, sulphur atoms occupy fourfold hollow sites [3,30]. It is known that on Pd(100) at small coverages of 0.25 ML (monolayer), sulphur forms a $p(2 \times 2)$ structure, and when the coverage is further increased to the saturation value of 0.5 ML the $c(2 \times 2)$ structure is formed [30]. We show the palladium *d*-band density of states (DOS) for both geometries in Fig. 4 where the vertical line corresponds to the center of the *d*-band. The values for the *d*-band center are gathered in Table 1 along with the corresponding values for O/Pd(100). The *d*-band model of Hammer and Nørskov [31] states that while the metal *d*-band center decreases in energy the antibonding states of the molecule towards the surface strengthen making the bonding between the molecule and metal atoms weaker. This is clearly seen in our adsorption energy calculations, when comparing the results against the *d*-band center

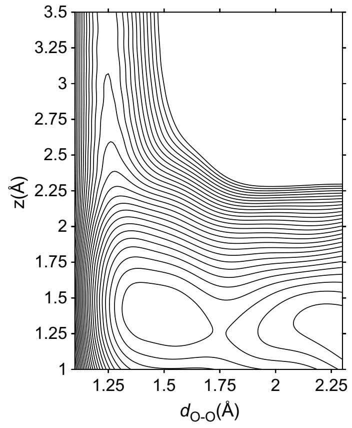

Fig. 3. The calculated PES for O_2 at the b-h-b configuration (corresponding to Fig. 2a), calculated using the frozen molecule approximation. The contour line separation is 0.1 eV.

Table 1
The adsorption and dissociation energies, extracted from Figs. 5 and 6, the labels referring to the corresponding labels in the figures, for the O_2 with different overlayer structures and materials.

Adsorbate	*c* [ML] 0.00	E_{dis} [eV] 0.2	E_{ads} [eV] 1.4	*d*-band center 1.4
S	0.125, h-t-h	1.4	0.0	1.8
O	(a)	4.5	0.1	1.5
S	0.125, b-h-b	0.3	0.7	1.8
O	(b)	0.2	1.1	1.5
S	0.25	0.6	0.5	1.9
O	(c)	0.5	0.8	1.5
S	0.50	3.0	0.0	2.6
O	(d)	–	0.1	1.9

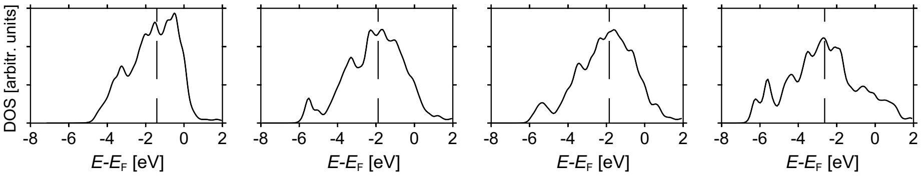

Fig. 4. The projected *d*-band Density of States for Pd atoms sitting next to the S atom with (a) clean surface, (b) coverage 0.125 ML, (c) $p(2 \times 2)$ (0.25 ML) (d)$c(2 \times 2)$ (0.5 ML). The dashed line indicates the center of the *d*-band.

Table 2
The Bader charge analysis data for the oxygen and sulphur covered surface (separated by the horizontal line) at 0.125 ML. The site column describes the distance from the adsorbate (e.g. 1 is the nearest neighbour and 2 is the second nearest neighbour).

Layer	Site	Type	Charge [e]
		S	6.2709
1st	1	Pd	9.98
1st	2	Pd	10.07
2nd	1	Pd	10.03
		O	6.78
1st	1	Pd	9.88
1st	2	Pd	10.08
2nd	1	Pd	9.98

heights in different cases. Indeed, the adsorption energies decrease with the decreasing *d*-band center of the surface metal atoms.

The Bader charge analysis [32–34] for the system, which has O_2 at 3.0 Å distance above the preadsorbed sulphur with the bond length 1.3 Å shows that also the Coulombic interaction between the oxygen atoms and the preadsorbed sulphur is slightly repulsive. The Bader charges are -0.27 and -0.16 for the sulphur atom and the oxygen molecule, respectively (see Table 2). This results in a net repulsive force of the order of 0.07 eV/Å calculated with a simple point charge model.

By the fact that the sulphur atoms occupy the hollow sites, which are also the most stable sites for the oxygen molecules, it is rather straightforward to speculate that the S atoms will physically block the potential dissociation sites which they are already occupying. This effect is clearly visible in Fig 5, where we show the PES results for the O_2 molecule approaching the sulphur atom, the nearest hollow site, and the p(2 × 2) and c(2 × 2) structures. The PES calculations show that the sulphur atom is blocking, as expected, the approaching molecule when the molecular trajectory approaches the sulphur atom directly. The p(2 × 2) structure increases the late barrier in the hollow site and reduces the kinetic energy gain in the entrance channel. However, only the c(2 × 2) structure makes the whole surface so repulsive towards O_2 that the sticking is completely blocked. As shown in the figure, in the latter case even the unoccupied hollow sites exhibit a large energy barrier for the sticking.

3.3. O/Pd(100)

Similarly to sulphur, oxygen occupies the four fold sites [30]. At 0.25 ML the oxygen forms a *p*(2 × 2) overlayer, and as the oxygen concentration gets higher, a metastable *c*(2 × 2) structure is formed [35]. We performed calculations for O_2 on O/Pd(100) analogous to the ones in the previous section for S/Pd(100). Fig. 6

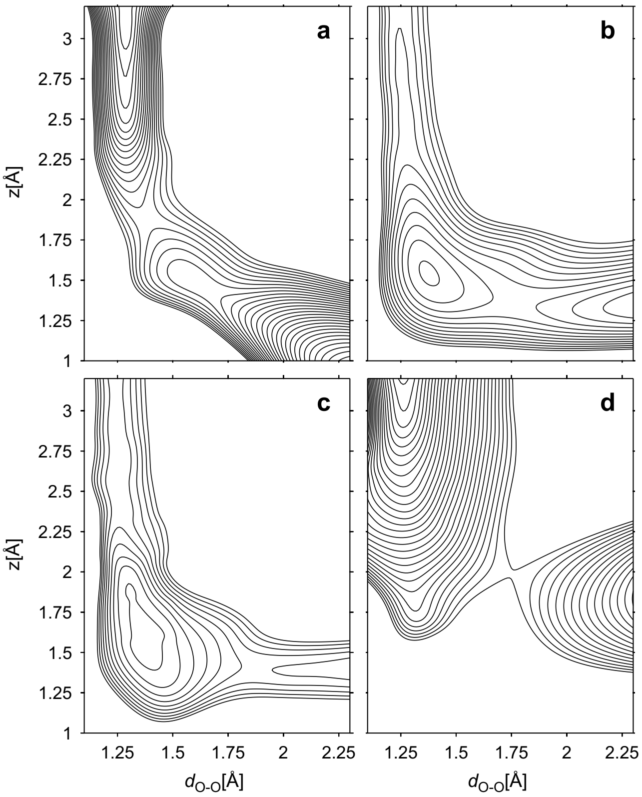

Fig. 5. The calculated PES plots for sulphur precovered Pd(100), (a) 0.125 ML, O_2 approaching hollow site occupied by S (b) 0.125 ML, nearest unoccupied hollow site (c) 0.25 ML, (d) 0.5 ML. The effect of the sulphur is already visible for the lowest coverage at the nearest hollow site. At the saturation coverage (c(2 × 2)), the PES shows very repulsive behaviour. The contour line separation is 0.1 eV.

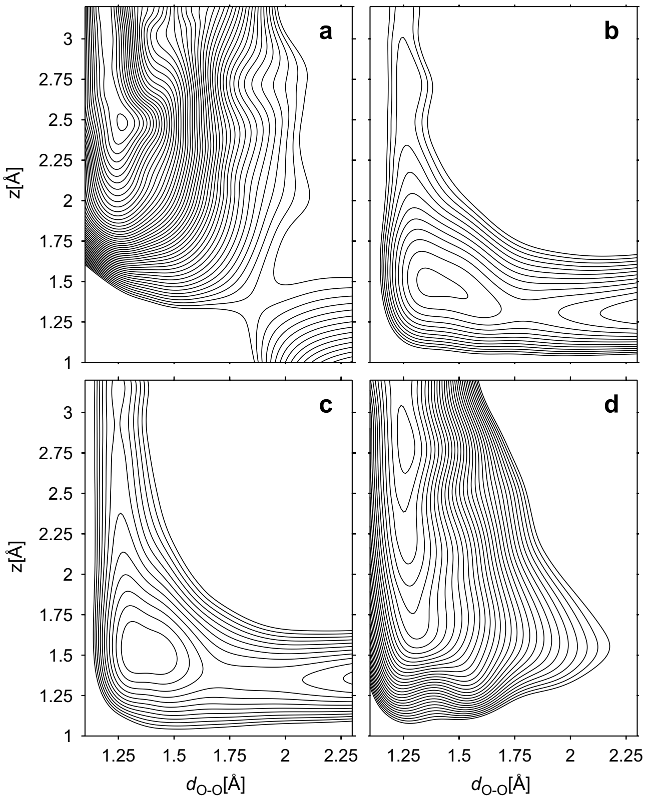

Fig. 6. The calculated PES plots for oxygen precovered Pd(100), (a) 0.125 ML, O_2 approaching hollow site occupied by O (b) 0.125 ML, nearest unoccupied hollow site (c) 0.25 ML, hollow site in between the preadsorbed layer, (d) 0.5 ML, hollow site in between the preadsorbed layer. The contour line separation is 0.1 eV.

demonstrates that the oxygen overlayer will have similar effects for the dissociation as the preadsorbed sulphur. The difference is that the effect is not as dramatic as on the S/Pd(100). The reason for this is that the oxygen states are less delocalized over the vacuum region, and therefore, the repulsion has a more localized nature. This is also seen as a lower dissociation barrier at the hollow site (see Figs. 5 and 6b), in contrast to the fact that for an O_2 molecule approaching directly at the top site of O atom, the barrier is higher than for O_2 approaching the S top site (Figs. 5 and 6b). The effect of sulphur therefore extends further than that of oxygen in the direction perpendicular to the surface. This is not unexpected, given the larger atomic radius of sulphur also as a free atom. Interestingly, however, the effect of oxygen on the electron density at the surface layer extends further than the effect of sulphur, see the discussion related to Fig. 8 below.

To compare the molecular adsorption and dissociation energies, we have gathered the information in Table 1. The Bader charge analysis shows that the on-surface oxygen atom attracts 0.8 electrons from the surface Pd atoms and the charge for the oxygen molecule is −0.16. This results in a 0.19 eV/Å repulsive force between the oxygen molecule and the preadsorbed oxygen atom. It is noteworthy that for the preadsorbed oxygen, also the second layer Pd atoms donate charge to the oxygen atom whereas in the case of sulphur the extra charge comes mainly from the nearest neighbour Pd atoms at the first layer. The extracted Bader charge analysis for the relevant atoms is included in Table 2.

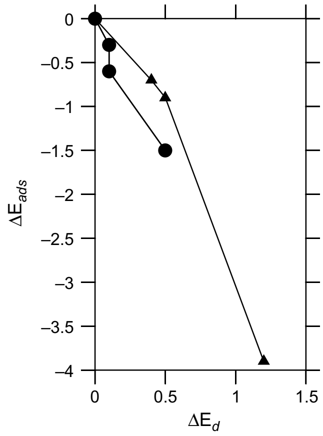

Fig. 7. Adsorption energy vs the *d*-band center of surface Pd atoms for S/Pd(100) (triangles) and O/Pd(100) (bullets). The values are relative to ones for the clean surface. The adsorption energy for the *d*-band shift of 1.2 is estimated from the PES for O_2 on 0.5 ML S/Pd(100) at position (1.25,1.75).

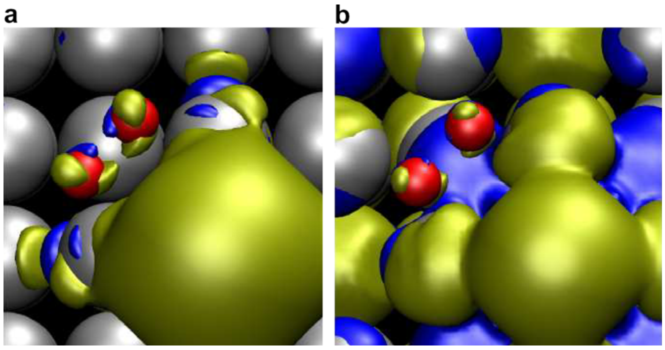

Fig. 8. The electron density difference maps indicating the difference in electron density between the clean surface and (a) 0.125 ML preadsorbed S and (b) 0.125 ML preadsorbed O, with O_2 at 1.4 Å above the surface hollow site. The decreased electron density is indicated by yellow (lighter) colour and the increased density by blue (darker) colour. The red and grey spheres are the oxygen atoms at the O_2 molecule and Pd atoms, respectively.

3.4. Comparison of S and O on Pd(100)

A plot showing the dependence of the adsorption energy against the *d*-band center of the metal atoms is shown in Fig. 7. The figure shows that the adsorption energy is reduced almost linearly as the sulphur and oxygen concentrations are increased. This supports the *d*-band model by Hammer and Nørskov and shows that the same effect is also responsible for the reduction of the adsorption energies. However, there is a difference between the preadsorbed species, which causes the horizontal shift between the two curves. This effect is most likely due to the Coulomb repulsion, which is more effective for the preadsorbed oxygen, thus leading to the more efficient reduction of the adsorption energies with smaller shifts in the *d*-band center. As seen in Table 2, the preadsorbed oxygen gains more electronic charge than sulphur, leading to increased Coulomb repulsion. A similar effect has been found by Pillay and Johannes, who discuss the inability of the *d*-band model to predict the activity of the oxygen reduction reaction on Pt(111) [11]. They point out that the *s* and *p* states are also involved in the bonding and that the direct electrostatic repulsion between the poison and the coadsorbates are indeed not taken into account in the *d*-band model.

To visualize the effect of different preadsorbates to the surface electron density, we have plotted electron density difference isosurfaces in Fig. 8 illustrating the quantity

$$\Delta n(\mathbf{R}) = n_c(\mathbf{R}) - n_a(\mathbf{R}). \qquad (1)$$

Here $n_c(\mathbf{R})$ is the electron density of the clean surface with O_2 at distance 1.4 Å above the surface hollow site and $n_a(\mathbf{R})$ is the electron density of the surface containing 0.125 ML of S (a) and O (b) preadsorbate with corresponding O_2 orientation. The charge density difference map shows that while preadsorbed sulphur has only little effect on the charge density of the surface metal atoms, the on-surface O attracts charge considerably from the surrounding Pd atoms. This can be well reasoned by the larger electronegativity of oxygen. Both preadsorbed species increase the density at the molecular antibonding states of the oxygen molecule (the little humps seen above the oxygen atoms in the molecule). The effect caused by the preadsorbed sulphur is more local in the slab direction, but non-local in the surface normal direction compared to the effect of preadsorbed oxygen.

4. Conclusions

In the previous sections, we have shown evidence for the mechanism of the blocking effect caused by the preadsorbed sulphur and oxygen. Firstly, both types of atoms block the four fold hollow sites physically by favouring the four fold symmetry in adsorption, therefore reducing the available space on the substrate surface. Secondly, the charging effects cause Coulombic repulsion between the approaching molecule and the preadsorbate. The charging effect is shown to be more effective in the case of the O/Pd(100) surface compared to the S/Pd(100) surface due to the larger electronegativity of oxygen. However, the sulphur states are more long-ranged and thus spill further out from the surface causing Pauli repulsion already at 3 Å above the sulphur atom. This leads to a more repulsive behaviour at the entrance channel for O_2 on S/Pd(100). Due to these facts, the effect of preadsorbed sulphur is more local than that of the preadsorbed oxygen. Nevertheless, as the surface sulphur concentration is increased to 0.5 ML the metal atoms are no longer visible to the approaching O_2 and therefore the surface seems more repulsive than the corresponding oxygen precovered surface.

According to our results it can be concluded that the main repulsive force in the case of the S precovered surface is the Pauli repulsion, whereas in the O precovered surface it is the Coulomb repulsion caused by the charging of the adsorbent and the incoming molecule. This can be concluded by looking at the charge analysis, the charge density difference maps, and the fact that both adsorbents have the same effect on the *d*-band of the surface Pd.

Acknowledgement

The computer resources provided by CSC, the Finnish IT centre for science are greatfully acknowledged. Parts of this work were supported by the Finnish National Graduate School for Materials Physics and the Finnish Cultural Foundation.

References

[1] P. Feibelman, D.R. Hamann, Phys. Rev. Lett. 52 (1984) 61.
[2] C.M. Wei, A. Groß, M. Scheffler, Phys. Rev. B 57 (1998) 15572.
[3] I. Makkonen, P. Salo, M. Alatalo, T.S. Rahman, Phys. Rev. B 67 (2003) 165415.
[4] P.A. Gravil, H. Toulhoat, Surf. Sci. 430 (1999) 176.
[5] S. Wilke, M. Scheffler, Phys. Rev. Lett. 76 (1996) 3380.
[6] K. Honkala, K. Laasonen, J. Chem. Phys. 115 (2001) 2297.
[7] W. Arabczyk, U. Narkiewicz, K. Kalucki, E. Freidenberg, Appl. Surf. Sci 72 (1993) 45.
[8] S. Jaatinen, J. Blomqvist, P. Salo, A. Puisto, M. Alatalo, M. Hirsimäki, M. Ahonen, M. Valden, Phys. Rev. B 75 (2007) 075402.
[9] P. Błoński, A. Kiejna, J. Hafner, Phys. Rev. B 77 (2008) 155424.
[10] X.Y. Deng, B.K. Min, A. Guloy, C.M. Friend, J. Am. Chem. Soc. 127 (2005) 9267.
[11] D. Pillay, M.D. Johannes, J. Phys. Chem. C 112 (2008) 1544.
[12] C. Zhang, P. Hu, M.H. Lee, Surf. Sci. 432 (1999) 305.
[13] Z. Yang, R. Wu, J.A. Rodriguez, Phys. Rev. B 65 (2002) 155409.

[14] G. Kresse, J. Hafner, J. Phys. Condens. Mat. 6 (1994) 8245.
[15] G. Kresse, J. Furthmüller, Comput. Mat. Sci 6 (1996) 15.
[16] G. Kresse, J. Furthmüller, Phys. Rev. B 54 (1996) 11169.
[17] G. Kresse, J. Joubert, Phys. Rev. B 59 (1999) 1758.
[18] P.E. Blöchl, Phys. Rev. B 50 (1994) 17953.
[19] J.P. Perdew, Y. Wang, Phys. Rev. B 45 (1992) 13244.
[20] J.M. Soler, E. Artacho, J.D. Gale, A. García, J. Junquera, P. Ordejón, D. Sánchez-Portal, J. Phys. Condens. Mat. 14 (2002) 2745.
[21] D. Sánchez-Portal, P. Ordejón, E. Artacho, J.M. Soler, Int. J. Quantum Chem. 65 (1997) 453.
[22] E. Artacho, D. Sánchez-Portal, P. Ordejón, A. García, J.M. Soler, Phys. Status Solidi (b) 215 (1999) 809.
[23] J. Junquera, O. Paz, D. Sánchez-Portal, E. Artacho, Phys. Rev. B 64 (2001) 235111.
[24] E. Anglada, J.M. Soler, J. Junquera, E. Artacho, Phys. Rev. B 66 (2002) 205101.
[25] M. Alatalo, A. Puisto, H. Pitkänen, A.S. Foster, K. Laasonen, Surf. Sci. 600 (2006) 1574.
[26] N. Troullier, J.L. Martins, Phys. Rev. B 43 (1991) 1993.
[27] J.P. Perdew, K. Burke, M. Ernzerhof, Phys. Rev. Lett. 77 (1996) 3865.
[28] H.J. Monkhorst, J.D. Pack, Phys. Rev. B 13 (1976) 5188.
[29] A. Groß, A. Eichler, J. Hafner, M.J. Mehl, D.A. Papaconstantopoulos, Surf. Sci. Lett. 539 (2003) L542.
[30] D. Kolthoff, D. Jürgens, C. Schwennicke, H. Pfnür, Surf. Sci. 365 (1996) 374.
[31] B. Hammer, J.K. Nørskov, Surf. Sci. 343 (1995) 211.
[32] R.F.W. Bader, Oxford University Press, 1990.
[33] G. Henkelman, A. Arnaldsson, H. Jónsson, Comput. Mater. Sci. 36 (2006) 254.
[34] E. Sanville, S.D. Kenny, R. Smith, G. Henkelman, J. Comp. Chem 28 (2007) 899.
[35] S.-L. Chang, P.A. Thiel, Phys. Rev. Lett. 59 (1987) 296.

Publication III

M. Lahti, K. Pussi, M. Alatalo, S.A. Krasnikov, A.A. Cafolla "Sulphur adsorption on Au{110}: DFT and LEED study" Reprinted from Surface Science, 604, 797

Surface Science 604 (2010) 797–803

Contents lists available at ScienceDirect

Surface Science

journal homepage: www.elsevier.com/locate/susc

Sulphur adsorption on Au{1 1 0}: DFT and LEED study

M. Lahti [a], K. Pussi [a,*], M. Alatalo [a], S.A. Krasnikov [b,c], A.A. Cafolla [b,c]

[a] *Department of Mathematics and Physics, Lappeenranta University of Technology, PO Box 20, FIN-53581, Lappeenranta, Finland*
[b] *School of Physical Sciences, Dublin City University, Glasnevin, Dublin 9, Ireland*
[c] *National Centre for Sensor Research (NCSR), Dublin City University, Glasnevin, Dublin 9, Ireland*

ARTICLE INFO

Article history:
Received 11 November 2009
Accepted for publication 1 February 2010
Available online 8 February 2010

Keywords:
DFT
LEED
Gold
Sulphur
Adsorption
Surface structure

ABSTRACT

The adsorption of sulphur on clean reconstructed Au{1 1 0}-(1 × 2) surface was studied using density functional theory (DFT) and quantitative low energy electron diffraction (LEED) calculations. The results show that the sulphur atoms form a (4 × 2) ordered structure which preserves the missing row reconstruction of the clean surface. The sulphur atom is found to adsorb on threefold hollow sites, on the {1 1 1} microfacets that border the trenches of the missing rows.

1. Introduction

The adsorption of sulphur and sulphur compounds on metal surfaces is an important topic in catalysis, interfacial physics, electrochemistry and material science [1]. In particular the adsorption and desorption of sulphur or sulphur containing compounds on gold surfaces has been an area of intense experimental and theoretical investigation for the past decade. Gold is an attractive substrate for surface science studies due to its chemical inertness; it has also become an increasingly important material in industrial applications because of its unique blend of properties for example its resistance to corrosion which makes it the ideal metal for electrical contacts and its potential applications in heterogeneous catalysis [2–4], while, in molecular electronics, the bonding between thiol groups and gold electrodes is the ideal molecular link for producing stable molecular junctions [3,4]. Gold is also the preferred substrate for the preparation self-assembled alkanethiol monolayers (SAMs), exploiting the interaction of the sulphur atom in the molecular endgroup with the Au [4]. For these reasons the interaction of atomic sulphur with the Au{1 1 1} and Au{1 0 0} surfaces has attracted much interest recently [2,3,5–8] but the exact details of the S–Au interface remain unclear. The majority of these studies indicate that the S atom bonds to high coordinated hollow site, in the case of alkylthiolates twofold bridge site and top site have also been suggested [9]. Large scale surface restructuring caused by the formation of a 2D AuS phase has also been reported for Au{1 1 1} [2]. Studies of sulphur adsorption on Au{1 1 0} have not yet produced a definite structure determination [1,10]. The aim of the present work is to provide a clearer understanding of the adsorption and desorption of sulphur atoms and molecules on the Au{1 1 0}-(1 × 2) surface and to provide additional support for the models proposed on the basis of low energy electron diffraction (LEED), Auger electron spectroscopy (AES) and thermally programmed desorption (TPD) studies. This paper presents the first detailed structural analysis of 0.13 ML sulphur adsorption on Au{1 1 0} surface using DFT and LEED intensity analysis. The results presented provide important information on the ordering of sulphur overlayers on the Au{1 1 0}-(1 × 2) surface and provide a starting point to understanding the reaction mechanisms sulphur containing organic molecules on this surface.

2. Calculations

2.1. DFT

First-principles DFT calculations were performed for the sulphur on Au{1 1 0} system to verify and analyze the experimental results presented in this paper.

The static calculations for total energies were performed using the Vienna ab initio simulation package (VASP) [11–14] including the projector augmented wave (PAW) [15] potentials. A kinetic energy cut-off of 300 eV was applied for the plane waves. This was found to produce converged results for both S and Au. For

---

* Corresponding author. Tel.: +358 33115 2681; fax: +358 33115 2600.
E-mail address: katariina.pussi@lut.fi (K. Pussi).

0039-6028/$ - see front matter © 2010 Elsevier B.V. All rights reserved.
doi:10.1016/j.susc.2010.02.002

the exchange-correlation potential the generalized gradient approximation (GGA) of the Perdew-Wang 91 (PW91) flavor [16] was employed. The $10 \times 8 \times 1$ Monkhorst–Pack mesh [17] was used for *k*-point sampling. While calculating the 2-dimensional Potential Energy Surface (PES) cuts, surface atoms were kept fixed (frozen substrate approximation). The PESs were constructed by varying the S_2 intramolecular bond length and the distance between the molecule and the surface and calculating the total energy.

The Au surface was modelled using the supercell approach, where periodic boundary conditions are applied to the central supercell so that it is reproduced periodically throughout *xy*-space. The surface slab was modelled with 8 layers of Au atoms; 4 atoms in the topmost substrate layer and 8 atoms in deeper layers, resulting in 60 Au atoms per supercell. A region of approximately 10 Å of vacuum was inserted in the *z*-direction to prevent interactions occurring between periodic images. An Au lattice constant of 4.17 Å was used, which was obtained from optimization of the bulk cell using the same computational parameters. The bottommost layer of the surface slab was frozen during the geometry relaxation. The adsorption energy of an S atom is defined as:

$$E_{ads} = \frac{1}{N_S} \times \left(E_{tot} - E_{clean} - \frac{N_S}{2} \times E_{S_2} \right) \tag{1}$$

where E_{tot} is the total energy of a relaxed Au/S supercell, E_{clean} is the total energy of the relaxed clean Au slab, N_S is the number of sulphur atoms and E_{S_2} is the energy of a S_2 molecule. For substitutional alloy structures the adsorption energy is defined as

$$E_{ads} = \frac{1}{N_S} \times \left(E_{tot} - E_{clean} - \frac{N_S}{2} \times E_{S_2} + N_S \times E_{Au-bulk} \right), \tag{2}$$

where $E_{Au-bulk}$ is the total energy of an Au bulk atom [18].

Six different atomic adsorption sites were modelled, as shown in Fig. 1. The high symmetry adsorption geometries (adsorption geometries that preserve the symmetry of the substrate, p2mm) are top (A), hollow (B), short-bridge (C) and long-bridge (D). In addition to these adsorption sites three different high symmetry substitutional alloy structures were also considered by replacing one Au atom in the unit cell by S where (a), (c) and (d) are the replacements sites of an Au atom in the "top row", in the bottom of the missing row and in the third layer below the top row position, respectively. Three low symmetry sites were also considered; off short bridge (E), off hollow (F) and a substitutional alloy structure were one Au atom is replaced by S atom in the second layer (b). In the previous LEED and TPD study of Krasnikov et al. [1] an electrochemical cell which primarily produces S_2 molecules was used to deposit the sulphur on the gold surface, for this reason both S atom and S_2 molecule adsorption were considered. For the S_2 adsorption the following different orientations of the molecular axis are considered: adsorption with the molecular axis aligned with the $[\bar{1}10]$ row, adsorption with the molecular axis perpendicular to the $[\bar{1}10]$ row and adsorption with the molecular axis perpendicular to the surface plane. The molecular adsorption sites and orientations are shown in Fig. 2. The adsorption energies for each site are listed in Table 1. The surface coverage of the $p(4 \times 2)$ sulphur layer was estimated to be about 0.13 ML according to Auger electron spectroscopy (AES) signal intensity analysis [1], which indicates that sulphur adsorbs as an S atom. This experimental result is also supported by our DFT calculations, in which the S atom adsorbed at the off-symmetry bridge site is found to be the most stable adsorption geometry.

The geometrical parameters for an S atom adsorbed at the off-symmetry short bridge site extracted from the DFT analysis are listed in Table 3. PES cuts for the S_2 molecule approaching the surface at the short bridge site (with the molecular axis either parallel or perpendicular to the $[\bar{1}10]$ row) and an S_2 molecule approaching the hollow site (molecular axis parallel to the $[\bar{1}10]$ row) are shown in Fig. 3. Judging by Fig. 3, S_2 will most likely adsorb molecularly, even though direct dissociation cannot be excluded based on the present results.

The most favorable molecular adsorption site is the short-bridge site with the S_2 molecular axis aligned along the $[\bar{1}10]$

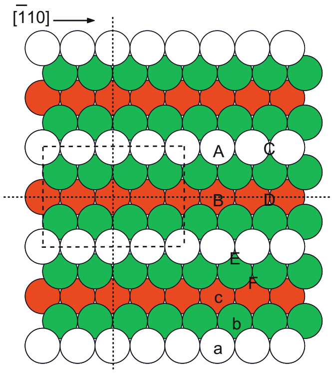

Fig. 1. Top view of the Au{110}-(1×2) surface showing the missing row reconstruction. The $p(4 \times 2)$ unit cell is indicated by the dashed line. The high symmetry adsorption sites are labelled with capital letters: A = top, B = hollow, C = short-bridge and D = long-bridge. The low symmetry adsorption sites are labelled with capital letters: E = off short-bridge and F = off hollow. Lower case letters a, b and c refer to the substitutional alloy structures described in the text. Dotted lines show the positions of the two mirror planes for the high symmetry models. Au atoms in different layers are indicated with different colors: dark grey = the third layer Au, light grey = the second layer Au and white = the first layer Au. (For interpretation of the references to color in this figure legend, the reader is referred to the web version of this article.)

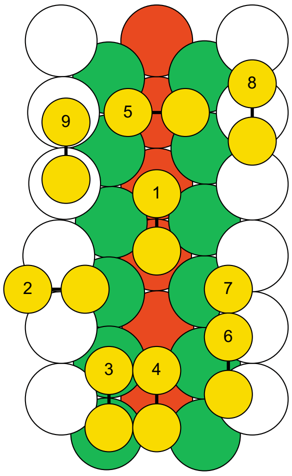

Fig. 2. Different adsorption sites and orientations for the S_2 molecule. The high symmetry adsorption sites are: 1 = long-bridge, 2 and 9 = short-bridge, 4 and 5 = hollow and 8 = top. The low symmetry adsorption sites are: 6 and 7 = off short-bridge and 3 = off hollow. The molecular axis of the molecule at the off-symmetry short-bridge site (site number 7), is oriented perpendicular to the {111} microfacet of the missing row wall. The coloring scheme for the Au atoms is the same as in Fig. 1 and the S_2 molecules are colored with light grey. (For interpretation of the references to color in this figure legend, the reader is referred to the web version of this article.)

Table 1
The adsorption energies for S and S_2 at the different adsorption sites considered in the DFT analysis. A positive E_{ads} indicates that the adsorption is unfavorable, while a negative value indicated that adsorption is likely, with the lowest value being the most stable. Letters in parentheses refer to the S atom adsorption sites shown in Fig. 1 and numbers in parentheses refer to the molecular adsorption sites shown in Fig. 2. The lowest adsorption energy is indicated in bold font. For the alloy structures only the best adsorption energy is shown.

Adsorption site	E_{ads} [eV]/S atom			
		S atom		S_2 molecule
Top	(A)	+0.044	(8)	−0.549
Hollow	(B)	−0.679	(4)	−0.906
			(5)	−0.836
Short bridge	(C)	−1.017	(9)	−0.967
			(2)	−0.743
Long bridge	(D)	−0.489	(1)	−0.327
Alloy	(a)	−0.397		
Off short bridge	(E)	−**1.476**	(6)	−0.840
			(7)	−0.613
Off hollow	(F)	−0.764	(3)	−0.898

row (E_{ads} = 0.967 eV, Fig. 3a). As seen in Fig. 3, an energy of about 0.5 eV is needed for S_2 to rotate through 90° in order to have the molecular axis perpendicular to the $[\bar{1}10]$ row (Fig. 3b). Looking at the PES cut shown in Fig. 3b, an energy of 0.4 eV is required to break the S–S bond. This leads to S atoms moving towards the off-symmetry short-bridge site which shows as a minimum in the right lower corner of the figure. This is the same site that is found to be the most favorable adsorption site for the S atom. Initially there is a sulphur atom on both sides of the top $[\bar{1}10]$ row at a S–S distance of about 2.86 Å. It is probable that because of the annealing treatments described in the next paragraph only half of these S atoms remain on the surface. This leads to the (4×2) periodicity and a coverage of 0.13 ML that are observed experimentally. It is clear by comparing the PES cuts for the parallel and perpendicular cases of short-bridge adsorption (Fig. 3a and b) that breaking of the S–S bond is unlikely to occur if the molecule remains aligned with its molecular axis is parallel to the $[\bar{1}10]$ row. The bond breaking is much more favourable after a 90° rotation.

In the previously reported experimental study of Krasnikov et al. [1] S_2 was deposited onto the clean Au{1 1 0}-(1×2) surface at room temperature. A saturation coverage of about 0.75 ML was reached after an exposure of about 6 L of S_2. Subsequently the surface was annealed at 650 K for one hour resulting in a sharp $p(4 \times 2)$ LEED pattern. From TPD spectra it was seen that most of the S and S_2 species are desorbed from the saturated sulphur layer in the temperature range between 295 K and 358 K. These species were weakly bonded and not ordered. For annealing at 650 K a single TPD peak was observed where the excess S and S_2 left the surface resulting in an ordered structure. A high temperature annealing of $p(4 \times 2)$ structure at 900 K removed all the sulphur (monitored by AES) and restored the Au{1 1 0}-(1×2) clean surface. The heating procedures described in the study of Krasnikov et al. [1] provide enough energy for rotation of the S_2 molecule and dissociation of the S–S bond in order for the S atom to reach the final adsorption site determined both by DFT and LEED intensity analysis.

The adsorption of the S_2 molecule at the hollow site (Fig. 3c) has only a slightly higher adsorption energy than the short-bridge site adsorption. The energy required to break the S–S bond at that site is, however, larger and thus it is less likely to occur. Also the adsorption energy of a S atom at hollow or off-symmetry hollow sites is considerably higher than that for a S atom adsorbed at the off-symmetry short-bridge site. Based on our DFT results and the LEED intensity analysis result presented below, we propose that the $p(4 \times 2)$-S adsorption geometry is created by adsorption of an S_2 molecule first on the high symmetry short bridge site from where it finds its way after a 90° rotation and dissociation to its final off-symmetry site.

For comparison, Lustemberg et al. obtained an adsorption energy of −3.9 eV for an S atom at the fcc hollow site on Au{1 1 1} [19]. This value was obtained by using the energy of a S atom in vacuum as a reference. The largest adsorption energy in our case, calculated using the S atom as a reference, is −4.4 eV, which is in a good agreement with the result of Lustemberg et al., given that the Au{1 1 0} surface has a more open structure than Au{1 1 1}, typically yielding larger adsorption energies. For Au{1 0 0}, Slusarski and Kostyrko found that the fcc hollow site is the most favourable site for S adsorption [8].

2.2. LEED I(E) analysis

The LEED experiment has been described elsewhere [1]. The data set utilized in the LEED intensity analysis consisted of 19 beams, (8 integer and 11 fractional order beams), ranging from 20 eV to 350 eV, recorded at 300 K. The cumulative energy range was 3562 eV. The dynamical LEED calculations were done using the Barbieri/Van Hove SATLEED package [20]. The relativistic phase shifts were calculated using the phase shift program [21] that was packaged with Tensor-LEED. The Muffin-tin radius of both the Au and S atoms was varied in the phase shift calculation as suggested by Materer et al. [22]. This did not improve the level of agreement thus the values used were set equal to one half of the interatomic distance (1.03 Å and 1.44 Å for sulphur and gold, respectively). The agreement between the theory and the experiment was tested using the Pendry R-factor and the error bars quoted were calculated using the Pendry RR-function [23]. Three different sets of phase shifts were used; one for sulphur, one for top layer Au atoms and one for the Au atoms in deeper layers. The Debye temperatures were set to 300 K and 165 K for sulphur and gold, respectively, and the l_{max} value was set to 8. These values were optimized at the final stage of the analysis. The real part of the inner potential is independent of energy and it was allowed to relax as is the normal procedure in the LEED analysis. The imaginary part of the inner potential was set to a fixed value at the beginning of the analysis (−5 eV), but in the final refinement an energy dependent form $\left(V_\imath = constant * E^{\frac{1}{3}}\right)$ was used.

Initially the clean Au{1 1 0}-(1×2) surface was analysed and the results obtained are in excellent agreement with those of Moritz et al. [24]. A large contraction of about 17% was found for the top layer interlayer spacing while the deeper interlayer spacings remain close to the bulk value of 1.44 Å. The third interlayer spacing exhibits large buckling of 0.26 Å, where the bottom of the "missing row" is lifted up towards the vacuum. The Pendry R-factor for the clean surface is 0.31, which is comparable with the value of 0.35 obtained in the earlier analysis of Moritz et al. [24].

Because the earlier AES [1] and our DFT analysis indicated that sulphur adsorbs as an S atom rather than an S_2 molecule, the Au{1 1 0}-$p(4 \times 2)$-S adsorption geometries considered in the LEED intensity analysis are formed by adsorption of one S atom in each unit cell. The adsorption sites used are the same as those used in the DFT analysis described above (see Fig. 1). Since the high symmetry adsorption sites all showed poor agreement, only the low symmetry sites were considered as in our DFT analysis. Because the structural search in the LEED intensity analysis works in a reasonably small radius, many different starting structures for the low-symmetry sites, (E) and (F), were considered. The off short-bridge sites (E) cover the adsorption sites lying on the line connecting the short-bridge site to the long-bridge site (C–D). The off-symmetry hollow sites (F) cover the adsorption sites on the line connecting the hollow site and top site (A–B) (see Fig. 1). These "lines" are explored in steps of 0.2 Å. In the case of the

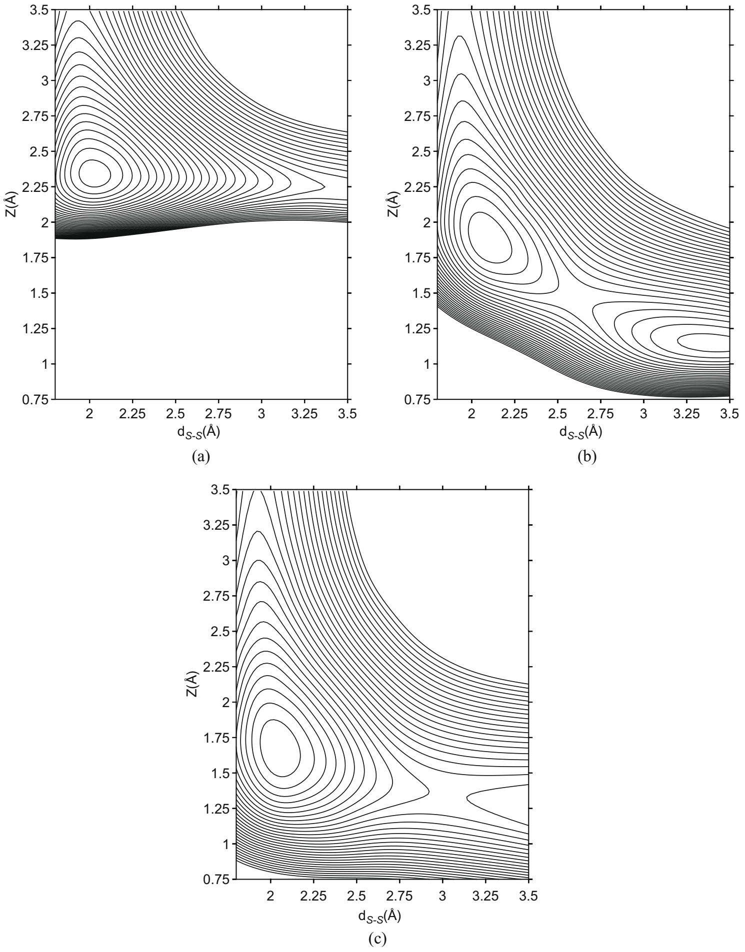

(a)

(b)

(c)

Fig. 3. PES cuts for an S_2 molecule approaching the short-bridge site with the molecular axis (a) parallel to the $[\bar{1}10]$ row (b) perpendicular to the $[\bar{1}10]$ row and (c) approaching the hollow site with the molecular axis parallel to the $[\bar{1}10]$ row. The *x*-axis shows the S–S bond length in Å and the *y*-axis shows the perpendicular distance between the first Au layer and the S_2 molecule. The energy step between each curve is 0.1 eV.

low-symmetry sites the symmetry of the system was lowered to p1m, which means that proper domain averaging had to be taken into account during the LEED calculation.

At the initial stage of the analysis the positions of the substrate atoms were kept fixed below the first Au layer and the only parameters varied were the perpendicular distance between the sulphur atom and the substrate, the vertical positions of the top layer Au atoms and the real part of the inner potential. In the second stage of the analysis the sulphur atom and top five layers of the substrate were allowed to relax. In the final state of the analysis the non-structural parameters (Debye temperatures, l_{max} (values up to $l_{max} = 15$ were considered), and imaginary part of inner potential) were optimized. The Pendry *R*-factors from different stages of analysis are listed in Table 2. After each stage, structures that have Pendry *R*-factor less than the sum of minimum *R*-factor and Pendry variance, were selected to be optimized further. Structural and non-structural parameters for the optimum structure are listed in Table 3 together with the results of our DFT analysis. Top and side views are shown in Figs. 4 and 5. The best fit $I(E)$ curves are shown in Fig. 6. The final *R*-factor reached is 0.35.

Table 2
Pendry *R*-factors from different stages of the analysis. Letters in parentheses refer to adsorption sites shown in Fig. 1. Structures were selected for further analysis using the Pendry's *RR*-method [23]. R_p^{min} stands for the minimum Pendry *R*-factor at each stage. For the alloy structures only the best *R*-factor is quoted.

Adsorption site	R_P (1. stage)	R_P (2. stage)	R_P (final)
Top (A)	0.80	–	–
Hollow (B)	0.73	–	–
Short bridge (C)	0.73	–	–
Long bridge (D)	0.72	–	–
Alloy (a)	0.69	0.59	–
Off short bridge (E)	0.64	0.48	**0.35**
Off hollow (F)	0.66	0.54	–
Pendry variance ($RR * R_P^{min}$)	0.06	0.05	

Table 3

Geometrical parameters extracted from DFT and LEED analysis. d(S–Au(i)) is the nearest neighbor bond length between the S and the Au in layer i, r(S) is the radius of sulphur, dz_{S-Au} is the vertical distance between the S atom and the center of mass of the first Au layer, δ_1 is the lateral distance off the short bridge site, δ_2/δ_3 are the lateral movement of the first layer Au atoms bonded to the S atom parallel/perpendicular to the $[\bar{1}10]$ direction, $\Delta_i^{average}$ is the average amplitude of buckling in ith layer, $dz_{ij}^{average}$ is the interlayer spacing between the centers of mass of the ith and jth layer, Θ_D is the Debye temperature, V_i is the imaginary part of the inner potential and l_{max} is the maximum l value used in the analysis. C is a constant that normalizes the imaginary part of inner potential such that its value is −5 eV at 150 eV. Some of the geometrical parameters are indicated in Figs. 4 and 5.

Structural parameter	DFT	LEED	Non-structural parameter	LEED
d(S–Au(1)) [Å]	2.38	2.3 ± 0.2	$\Theta_D(S)$ [K]	100
d(S–Au(2)) [Å]	2.42	2.4 ± 0.2	$\Theta_D(Au_{surface})$ [K]	205
r(S) [Å]	0.94	0.9	$\Theta_D(Au_{bulk})$ [K]	165
dz_{S-Au} [Å]	0.98	1.1 ± 0.2	V_i	$C * E^{\frac{1}{3}}$
δ_1 [Å]	1.43	1.4 ± 0.2	l_{max}	8
δ_2 [Å]	0.18	0.04 ± 0.2		
δ_3 [Å]	0.08	0.08 ± 0.2		
$\Delta_1^{average}$ [Å]	0.07	0.09 ± 0.03		
$\Delta_2^{average}$ [Å]	0.04	0.07 ± 0.07		
$\Delta_3^{average}$ [Å]	0.13	0.11 ± 0.07		
$\Delta_4^{average}$ [Å]	0.02	0.01 ± 0.11		
$\Delta_5^{average}$ [Å]	0.01	0.03 ± 0.14		
$dz_{12}^{average}$ [%]	−11	817 ± 5		
$dz_{23}^{average}$ [%]	+1	±0 ± 6		
$dz_{34}^{average}$ [%]	+1	+1 ± 9		
$dz_{45}^{average}$ [%]	+3	+1 ± 14		
$dz_{56}^{average}$ [%]	−2	+2 ± 20		
dz_{Bulk} [Å]	1.474	1.442		

3. Results and discussion

From previous studies it is known that sulphur prefers high coordinated adsorption sites [6]. The (2 × 1) reconstruction of the clean Au{1 1 0} surface provides potential binding sites and makes it reactive towards adsorbates. The study of Krasnikov et al. [1] proposes that the S atoms that remain on the surface after annealing are bonded to the "missing row" sites (which they identify as high symmetry hollow sites), by, e.g. visual inspection of the differences between the $I(E)$ curves measured from the clean Au{1 1 0}-(2 × 1) and Au{1 1 0}-(2 × 4)-S surfaces. Our DFT and LEED calculations confirm the "missing row site adsorption", but instead of high symmetry hollow site, our results show that the most favored adsorption site for S is situated on the fcc{1 1 1} walls of the missing rows.

The S atom is found to adsorb symmetrically almost in the center of the threefold hollow site situated at the fcc{1 1 1} microfacets bordering the trenches created by the missing rows. The lateral distance between the S atoms on the surface is large, about 8 Å, which means that S–S interactions are not important compared to the S–Au interactions. The lateral distance to the high symmetry short-bridge site determined by both DFT and LEED is 1.4(3) Å. The S atom is bonded to two Au atoms in the first substrate layer and one Au atom in the second substrate layer. These bonds are almost equal in length; 2.3(8) Å and 2.4(2) Å for bonds between S and the first layer Au atoms and S and the second layer Au atom, respectively. The radius of the sulphur atom calculated using the nearest neighbor Au–S distance (2.38 Å) and Au radius (1.44 Å) is 0.94 Å. Compared to the inward relaxation of the clean surface [24] the sulphur adsorption reduces the inward relaxation in the case of DFT. This effect has been reported before, e.g. in the paper of Lahtinen et al. [29]. In the LEED intensity analysis the first interlayer spacing remains at the same value as in the case of the clean Au{1 1 0}-(1 × 2) surface. This is not surprising, since there are very few differences between the $I(E)$ curves that are common in both Au{1 1 0}-(2×1) and Au{1 1 0}-(2×4)-S systems [1]. The deeper interlayer spacings, calculated between the centers of mass of the adjacent layers, remain close to the bulk value in both the DFT and LEED analyses. There is a significant average buckling (0.13/0.11 ± 0.07 Å DFT/LEED) in the third Au layer, because of the outward relaxation of the atoms in the bottom of the missing row. The average buckling (compared to the center of mass of the layer) of the Au atoms in the first layer is 0.07/0.09 ± 0.03 Å

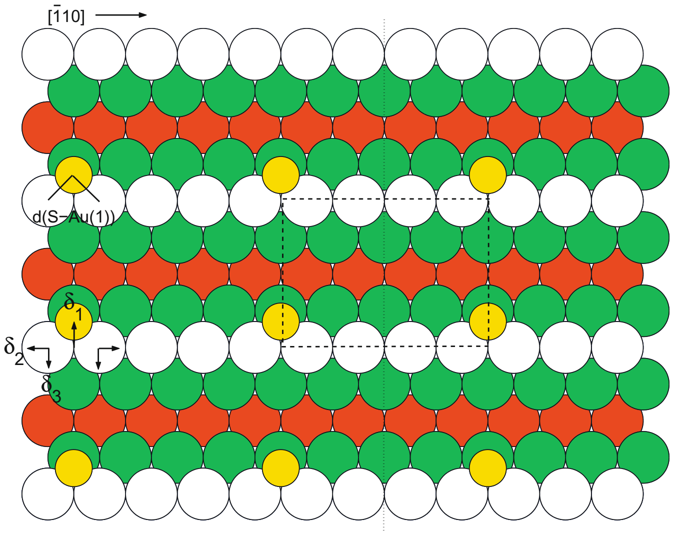

Fig. 4. Top view of the optimized geometry. The dashed line shows the unit cell. The dotted line shows the position of the mirror plane. Geometrical parameters shown in the figure are listed in Table 3. The coloring scheme for the atoms is the same as that in Figs. 1 and 2. (For interpretation of the references to color in this figure legend, the reader is referred to the web version of this article.)

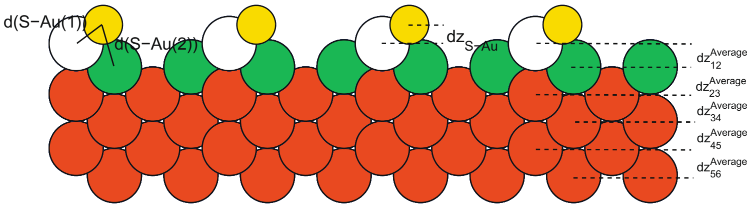

Fig. 5. Side view of the optimized geometry. Geometrical parameters shown in the figure are listed in Table 3. The coloring scheme for the atoms is the same as that in Figs. 1, 2 and 4. (For interpretation of the references to color in this figure legend, the reader is referred to the web version of this article.)

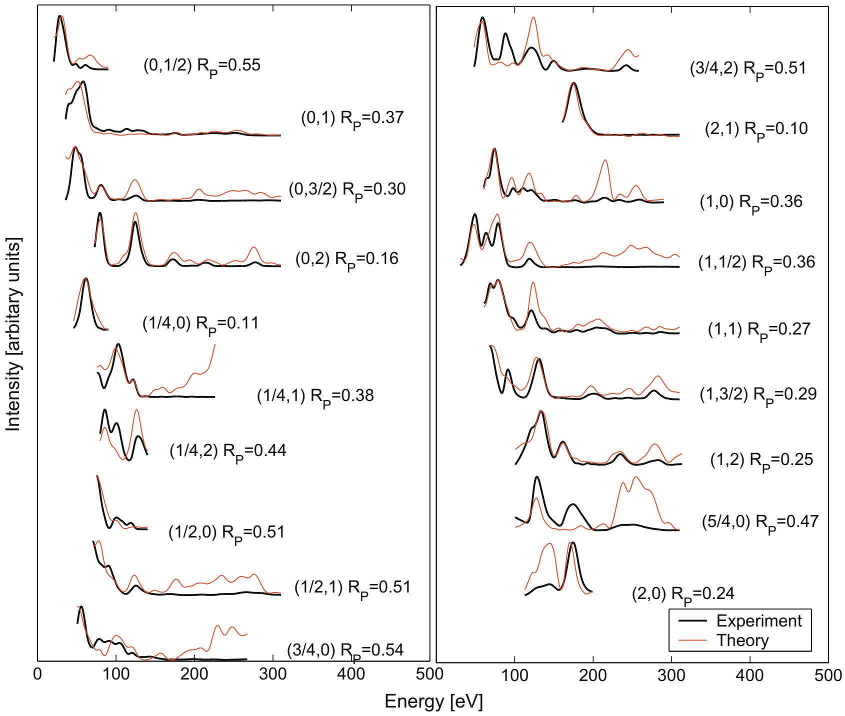

Fig. 6. *I*(*E*) curves for the best fit structure. Thick and thin lines correspond to experiment and calculation, respectively. *R*-factors for individual beams are indicated in the figure. The overall Pendry *R*-factor is 0.35.

(DFT/LEED). Buckling in the deeper layers is negligible. There is some lateral relaxation in the first layer, in which the Au atoms that are bonded to the sulphur move away slightly from the S atom (see Fig. 4). This lateral relaxation is more evident in the DFT analysis. In the LEED analysis it is within the error bars, which is not surprising, since normal incidence LEED is known to be more sensitive to the parameters that are perpendicular to the surface.

In previous studies of S adsorption on (2×1) reconstructed fcc{1 1 0} type metal surfaces (Au{1 1 0} [10,1], Pt{1 1 0} [25] and Ir{1 1 0} [26–28]) structural models were proposed for Ir{1 1 0} and Au{1 1 0}. In the case of Pt{1 1 0}, no structural model was proposed. On the Ir{1 1 0} surface at 0.5 ML coverage the sulphur atoms form zig-zag rows along the $[\bar{1}\,1\,0]$ direction, where the adsorption site of the sulphur is the same fcc{1 1 1} type hollow as observed in our analysis, although the sulphur coverage is much higher.

On Au{1 0 0} the most favorable adsorption site for sulphur is the fourfold coordinated hollow site [8]. On Au{1 1 1} at low sulphur coverages the most favorable site is threefold hollow [3,5,6]. On other close packed metal surfaces (Co, Ru, Re, Ni, Pt, Rh, Pd) the adsorption site is also found to be the three- or fourfold hollow site [29]. Lahtinen et al. report metal–sulphur bond lengths in the range of 2.11–2.32 Å. If the S radius is calculated by subtracting the metal radius (calculated from the interatomic distance in bulk), from the metal–sulphur bond length then a S radius in range of 0.82–0.99 Å is obtained [29]. With 0.25 ML sulphur on Au{1 1 1} the Au–S bond length is found to be 2.39 Å which corresponds to a S atom radius of 0.95 Å [5]. These values for the S radius correspond well with our value of 0.94 Å.

On unreconstructed fcc{1 1 0} type metal surfaces such as Ni{1 1 0}, Cu{1 1 0} and on Fe{1 1 0} sulphur adsorbs on high coordinated (threefold or fourfold) hollow sites [30–35]. The metal–sulphur bond is reported to be 2.14–2.20 Å on Ni{1 1 0} [32], 2.37 ± 0.03 Å on Cu{1 1 0} [36] and 2.19 Å on Fe{1 1 0} [35]. The sulphur radii calculated from the above values are 0.90–0.96 Å, 1.09 Å and 0.95 Å, for Ni{1 1 0}, Cu{1 1 0} and Fe{1 1 0}, respectively. On Mo{1 1 0} a low-symmetry position near the long-bridge site is favored [37,38]. Sulphur radii for different coverages of S on Mo{1 1 0} are in the range of 1.0–1.1 Å.

4. Conclusions

In this paper we have demonstrated by DFT and LEED calculations that the most favorable adsorption site of sulphur on Au{1 1 0}-(4 × 2)-S is a threefold hollow site that is situated at the fcc{1 1 1} microfacets that form the walls of the missing rows. There is very good agreement between the geometrical parameters extracted from the DFT and LEED analyzes as shown in Table 3. The results reported in this paper are also in very good agreement with the previously reported results for S adsorption on other metal surfaces. Although the level of agreement reached in the LEED $I(E)$ analysis is similar to the other LEED studies of Au surfaces, it is lower than found for most other low index surfaces, probably due to the lower accuracy of the phase shift calculations for high-atomic-number atoms such as Au, Pb and Pt [22] and due to the large unit cell.

Acknowledgements

M. Lahti and K. Pussi would like to thank National Graduate School in Materials Physics and Academy of Finland for funding, and CSC – IT Center for Sciences Ltd., for computational resources. A. Cafolla acknowledged funding from the Irish Higher Education Authority PRTLI programme and from Science Foundation, Ireland through the Research Frontiers Programme (Grant No. 06/RFP/PHY082).

References

[1] Sergey A. Krasnikov, Greg Hughes, Attilio A. Cafolla, Surf. Sci. 601 (2007) 3506.
[2] Monica M. Biener, Juergen Biener, Cynthia M. Friend, Langmuir 21 (2005) 1668.
[3] Miao Yu, H. Ascolani, G. Zampieri, D.P. Woodruff, C.J. Satterley, Robert G. Jones, V.R. Dhanak, J. Phys. Chem. C 111 (2007) 10904.
[4] Henrik Grönbeck, Hannu Häkkinen, Robert L. Whetten, J. Phys. Chem. C 112 (2008) 15940.
[5] J.A. Rodriguez, J. Dvorak, T. Jirsak, G. Liu, J. Hrbek, Y. Aray, C. Gonzales, J. Am. Chem. Soc. 125 (2003) 276.
[6] J. Gottschalck, B. Hammer, J. Chem. Phys. 116 (2002) 784.
[7] C. Vericat, M.E. Vela, G. Andreasen, R.C. Salvarezza, Langmuir 17 (2001) 4919.
[8] T. Ślusarski, T. Kostyrko, Surf. Sci. 603 (2009) 1150.
[9] D.C. Jackson, A. Chaudhuri, T.J. Lerotholi, D.P. Woodruff, Robert G. Jones, V.R. Dhanak, Surf. Sci. 603 (2009) 807.
[10] D.M. Jaffey, R.J. Madix, Surf. Sci. 258 (1991) 359.
[11] G. Kresse, J. Hafner, J. Phys. Cond. Mater. 6 (1994) 8245.
[12] G. Kresse, J. Furthmüller, Comput. Mater. Sci. 6 (1996) 15.
[13] G. Kresse, J. Furthmüller, Phys. Rev. B 54 (1996) 11169.
[14] G. Kresse, J. Joubert, Phys. Rev. B 59 (1999) 1758.
[15] P.E. Blöchl, Phys. Rev. B 50 (1994) 17953.
[16] J.P. Perdew, Y. Wang, Phys. Rev. B 45 (1992) 13244.
[17] H.J. Monkhorst, J.D. Pack, Phys. Rev. B 13 (1976) 5188.
[18] J.L. Nie, H.Y. Xiao, X.T. Zu, Fei Gao, Chem. Phys. 326 (2006) 583.
[19] P.G. Lustemberg, C. Vericat, G.A. Benitez, M.E. Vela, N. Tognalli, A. Feistein, M.L. Martiarena, R.C. Salvarezza, J. Phys. Chem. C 112 (2208) 11394–11402.
[20] M.A. Van Hove, W. Moritz, H. Over, P.J. Rous, A. Wander, A. Barbieri, N. Materer, U. Starke, G.A. Somorjai, Surf. Sci. Rep. 19 (1993) 191.
[21] A. Barbieri, M.A. Van Hove, private communication.
[22] N. Materer, U. Starke, A. Barbieri, R. Döll, K. Heinz, M.A. Van Hove, G.A. Somorjai, Surf. Sci. 325 (1995) 207.
[23] J.B. Pendry, J. Phys.C: Solid State Phys. 13 (1980) 937.
[24] W. Moritz, D. Wolf, Surf. Sci. 163 (1985) L655.
[25] H.P. Bonzel, R. Ku, J. Chem. Phys. 58 (1973) 4617.
[26] J. Kuntze, S. Speller, W. Heiland, Phys. Rev. B 62 (2000) 4681.
[27] C.-M. Chan, M.A. Van Hove, Surf. Sci. 183 (1987) 303.
[28] E.D. Williams, C.-M. Chan, W.H. Weinberg, Surf. Sci. 81 (1979) L309.
[29] J. Lahtinen, P. Kantola, S. Jaatinen, K. Habermehl-Cwirzen, P. Salo, J. Vuorinen, M. Lindroos, K. Pussi, A.P. Seitsonen, Surf. Sci. 599 (2005) 113.
[30] J.E. Demuth, D.W. Jepsen, P.M. Marcus, Phys. Rev. Lett. 32 (1974) 1182.
[31] R. Bäcker, G. Hörz, Vacuum 46 (1995) 1101.
[32] A.P. Woodhead, P. Bailey, T.C.Q. Noakes, D. Norman, G. Thornton, Surf. Sci. 496 (2002) 299.
[33] A.F. Carley, P.R. Davies, R.V. Jones, K.R. Harikumar, G.U. Kulkarni, M. Wyn Roberts, Surf. Sci. 447 (2000) 39.
[34] L. Berbil-Bautista, S. Krause, T. Hänke, M. Bode, R. Wiesendanger, Surf. Sci. 600 (2006) L20.
[35] Michelle J.S. Spencer, Andrew Hung, Ian K. Snook, Irene Yarovsky, Surf. Sci. 540 (2003) 420.
[36] A. Atrei, A.L. Johnson, D.A. King, Surf. Sci. 254 (1991) 65.
[37] J. Toofan, G.R. Tinseth, P.R. Watson, J. Vac. Sci. Technol. A 12 (4) (1994) 2246.
[38] M. Chen, P.G. Clark Jr., T. Mueller, C.M. Friend, Phys. Rev. B 60 (1999) 11783.

Publication IV

I.M McLeod, V.R Dhanak, A. Matilainen, M. Lahti, K. Pussi, K.H.L. Zhang
"Structure determination of p($\sqrt{3} \times \sqrt{3}$)R30° Bi-Ag(111) surface alloy using
LEED I-V and DFT analyses" Reprinted from Surface Science, 604,
1395©(2010)with permission from Elsevier.

Surface Science 604 (2010) 1395–1399

Contents lists available at ScienceDirect

Surface Science

journal homepage: www.elsevier.com/ locate/susc

Structure determination of the $p\left(\sqrt{3}\times\sqrt{3}\right)R30^\circ$ Bi–Ag(111) surface alloy using LEED I–V and DFT analyses

I.M. McLeod [a], V.R. Dhanak [a,*], A. Matilainen [b], M. Lahti [b], K. Pussi [b], K.H.L. Zhang [c]

[a] Department of Physics, the University of Liverpool, Liverpool L69 3BX, UK
[b] Department of Mathematics and Physics, Lappeenranta University of Technology, P.O. Box 20, 53851 Lappeenranta, Finland
[c] Department of Chemistry, Chemistry Research Laboratory, Mansfield Road, Oxford, OX1 3TA, UK

ARTICLE INFO

Article history:
Received 16 February 2010
Accepted 29 April 2010
Available online 21 May 2010

Keywords:
Bismuth
Ag(111)
LEED
DFT
Surface alloy

ABSTRACT

The deposition of 1/3 of a monolayer of Bi on Ag(111) leads to the formation of $BiAg_2$ surface alloy with a long range ordered $\left(\sqrt{3}\times\sqrt{3}\right)R30^\circ$ superstructure. A detailed analysis of this structure using LEED I–V measurements together with DFT calculations is presented. We find strong correlation between experimental and calculated LEED I–V data, with the fit between the two data sets having a Pendry's reliability factor of 0.16. The Bi atom is found to replace one top layer Ag atom in each unit cell, forming a substitutional $BiAg_2$ surface alloy, with the Bi atoms residing approximately 0.6 Å above the Ag atoms due to their size difference. DFT calculations are in good agreement with the LEED results.

1. Introduction

The understanding of the growth of thin metallic films on metallic substrates has been the subject of much research over the last few years. Whilst these systems are of interest from the view point of technological applications, the growth processes can be complex, offering a range of interesting phenomena at the atomic level. This is particularly the case for the growth of semi-metal overlayers, such as Pb, Sb and Bi on metal surfaces [1–6]. Bismuth is a particularly attractive adsorbate material due to its small electron effective mass, anomalously high values of electron mean free path and mobility, highly anisotropic Fermi surface as well as having a long Fermi wavelength at room temperature, and small overlap between the conduction and valence bands [7–10]. Furthermore, the growth of Bi nanowires by vapour deposition on Ag(111) was recently reported in an STM study [11]. Such nanostructures are expected to exhibit interesting effects due to quantum confinement and finite size effects.

The Bi–Ag(111) system is very similar to that of the much studied case of Pb–Ag(111) [12–16]. Since neither Bi nor Pb are miscible with Ag, it is expected that the growth process would occur by formation of dense islands on the Ag(111) surface. However, in both cases, it is found that at 1/3 ML coverage, a $\left(\sqrt{3}\times\sqrt{3}\right)R30^\circ$ superstructure is observed as a result of surface alloy formation, which represents a new class of materials, and is similar to what has been observed for Sb and Bi on Cu (111), Sb on Ag(111) and Pb on Ni(111) [17–25]. At higher coverages, above some critical value, a de-alloying process occurs and the monolayer growth leads to a dense plane above the Ag(111) surface. The $\left(\sqrt{3}\times\sqrt{3}\right)R30^\circ$ structure observed for Bi and Pb on Ag(111) is of particular interest as a new class of material because the two dimensional alloy structure in both cases appears to behave like a 2-D electron gas with quantum confinement leading to spin–orbit coupling, known as the Rashba effect, which has implications for spintronic applications [26–28]. Recently, a structural study of the $\left(\sqrt{3}\times\sqrt{3}\right)R30^\circ$ Pb–Ag(111) system using surface X-ray diffraction (SXRD) [14] and photoemission [15] has shown that the Pb atoms are embedded into the Ag top layer, forming a well ordered $PbAg_2$ surface alloy and a similar structure has been suggested for the Bi–Ag(111) system [27]. Nevertheless, a detailed investigation on the atomic structures of these 2-D surface alloys is still lacking, even though such information plays a critical role in determining the electronic structures of the surface alloys.

As mentioned above, the $\left(\sqrt{3}\times\sqrt{3}\right)R30^\circ$ surface alloy structure has also been observed for adsorbates on other fcc (111) systems and studied using a variety of techniques. In particular, Vries et al. [17] used SXRD to investigate this structure for Sb–Cu(111) and Sb–Ag (111) systems. The latter system has also been studied using quantitative low energy electron diffraction (LEED) [18] and impact–collision ion scattering spectroscopy [19]. Bailey et al. [20] and Quinn et al. [21] studied the Sb–Cu(111) and Sb–Ag(111) structures, respectively using medium-energy ion scattering (MEIS). In these cases it was found that the correct structure was a surface alloy with a slightly 'rumpled' surface layer in which all the surface atoms occupy 'hcp' hollow sites, directly above second layer substrate atoms, rather

---

* Corresponding author.
E-mail address: vin@liverpool.ac.uk (V.R. Dhanak).

doi:10.1016/j.susc.2010.04.027

than the ‘fcc’ hollow sites, confirming a stacking fault in the interface region between the top surface alloy layer and the substrate. These findings were supported by a DFT (density functional theory) total energy calculation although it was noted that there was negligible energy difference between the faulted and unfaulted surface alloy structures [22]. It was further noted that for Sb on Ag(111), the MEIS study showed that it was possible to form both the faulted and unfaulted surface structures, depending on the Sb dosing history, implying a subtle influence of subsurface Sb [21]. On the other hand, MEIS and LEED investigations of this structure for the Pb–Ni(111) system [6,23], and a SXRD study of Bi–Cu(111) system [24] showed that the correct structure was not the faulted surface alloy but the substitutional alloy structure. The latter result was further supported by a recent DFT calculation [25].

In this paper we present a detailed atomic structure of the $\left(\sqrt{3}\times\sqrt{3}\right)R30^\circ$ Bi–Ag(111) structure using a combined LEED I–V and DFT analyses. The results show that a Bi atom is found to replace one top layer Ag atom in each unit cell, forming a substitutional unfaulted $BiAg_2$ surface alloy, with the larger Bi atoms residing about 0.6 Å above the Ag atoms due to the size difference.

2. Experiment

The experiments were made in a standard ultra high vacuum (UHV) surface science chamber consisting of a PSP Vacuum Technology electron energy analyser, dual anode X-ray source, rear view LEED optics from OCI Vacuum Microengineering and an Omicron STM-1. The base pressure of the system was less than 2×10^{-10} mBar, with hydrogen as the main residual gas in the chamber. The Ag(111) surface was prepared by cycles of Ar ion bombardment and annealing to approximately 800 K. The sample was considered clean when the LEED pattern showed sharp integer order spots and XPS did not show any traces of contamination.

Bi was deposited onto the clean Ag(111) surface from a well degassed Omicron K-cell. During deposition the Ag sample was kept at room temperature and the vacuum pressure did not exceed 3×10^{-10} mBar. The Bi was deposited at a constant rate of 0.1 ML/min until a sharp $\left(\sqrt{3}\times\sqrt{3}\right)R30^\circ$ structure was observed.

The intensity of the diffraction spots as a function of the energy of the incident electrons (LEED I–V spectra) was measured at normal incidence of the primary beam. The spectra were background subtracted and normalised with respect to the primary beam current. The intensities of the symmetrically equivalent spots were averaged in order to reduce experimental noise.

3. Results and discussion

The data set utilized consisted of 9 beams (5 integer and 4 fractional order beams) ranging from 30 eV to 330 eV and recorded at 300 K (Fig. 1). The cumulative energy range was 1640 eV. The dynamical LEED calculations were done using the Barbieri/Van Hove SATLEED package [29]. The relativistic phase shifts were calculated using the phase shift program [30] that was packaged with SATLEED. Pendry's reliability factor, $R_{P,}$ was used to quantify the agreement between experimental and calculated data and the error bars quoted were calculated using the Pendry RR-function [31]. Three different sets of phase shifts were used; one for bismuth, one for top layer Ag atoms and one for the Ag atoms in deeper layers. At the beginning of the analysis the Debye temperatures were set to 120 K and 225 K for bismuth and silver respectively, the l_{max} value was set to 8 and the imaginary part of inner potential was set to −5 eV. These values were optimized at the final stage of the analysis. The real part of the inner potential is independent of energy and was allowed to relax as is the normal procedure in the LEED analysis.

Six different structural models were considered in the LEED calculations. These included four high symmetry adsorption

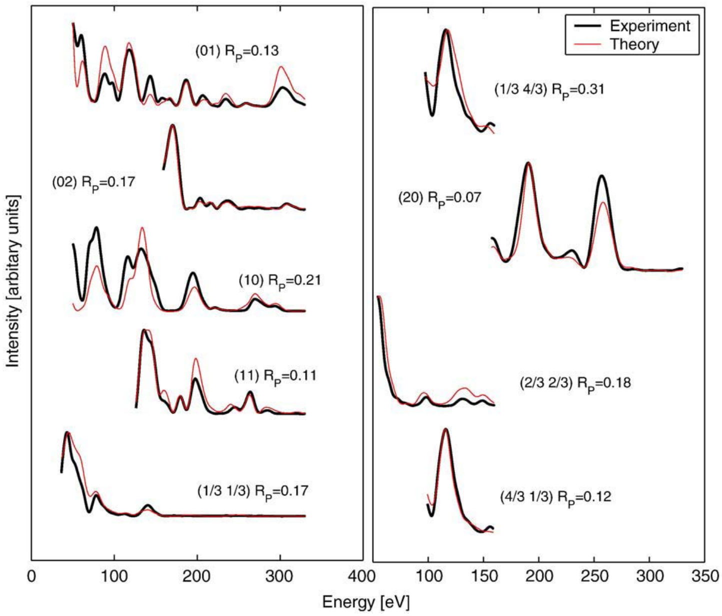

Fig. 1. I–V curves for the best fit structure compared with experimental data. Individual beam *R*-factors are shown.

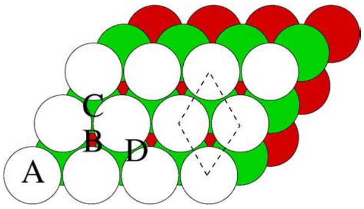

Fig. 2. Adsorption sites: A = top, B and C = hollow and D = bridge. Top three layers of the substrate are shown. (1×1) unit cell is shown with dashed line.

geometries, namely the top (A) and hollows (B and C, for fcc and hcp hollows, respectively), as well as the bridge site (D), as shown in Fig. 2. Adsorption at bridge site (D) lowers the symmetry of the surface, which means that proper domain averaging has to be taken into account in the LEED analysis. As well as these adsorption sites, two high symmetry substitutional alloy structures were also considered. The first of these was formed by placing one Bi atom per unit cell in a substitutional position over an essentially unperturbed Ag(111) surface layer to give the $\left(\sqrt{3} \times \sqrt{3}\right)R30^\circ$ superstructure. The second was a similar surface alloy but with all the surface atoms displaced to the 'hcp' hollow sites, the so-called faulted surface alloy structure [20–22]. In Fig. 2, the "hcp" hollow site is indicated by "C".

At the first stage of the analysis the substrate atom positions were kept fixed and the only parameters varied were the perpendicular distance between the bismuth and substrate atoms, and the real part of the inner potential. In the second stage of the analysis the bismuth atom and top five layers of the substrate were allowed to relax. In the final state of the analysis the non-structural parameters (Debye temperatures, l_{max} and imaginary part of inner potential) were optimized.

The Pendry *R*-factors from different stages of analysis are listed in Table 1. After each stage, structures that have a Pendry *R*-factor less than the sum of the minimum *R*-factor and Pendry variance were selected to be optimized further. The substitutional surface alloy model was clearly most favourable after the 1st stage, consistent with the structure previously suggested by C.R. Ast et al. [27], rendering it unnecessary to further optimize the other structures. The faulted surface alloy in which all the surface atoms occupy 'hcp' hollow sites was found to be the least favourable structure. Structural and non-structural parameters for the alloyed structure are listed in Table 2 together with the results from our DFT analysis (see below). Top and side views of the structure are shown in Fig. 3. The corresponding best fit I–V curves are shown in Fig. 1. The final *R*-factor reached was 0.16. It is also noted that the optimized structure incorporates a slight buckling of the fourth layer of the silver substrate. This is interesting because for the similar $\left(\sqrt{3} \times \sqrt{3}\right)R30^\circ$ Pb/Ag(111) structure, Dalmas et al. [14] suggest a slight out of plane distortion of the Ag atoms in the top surface layer based on STM and SXRD measurements. They attribute this to a possible Peierls type distortion, although they do note that this distortion could be an effect of their measurements. The overall structure remains bulk like with a small contraction of the top layers.

Table 1
Pendry *R*-factors from LEED analysis and adsorption energies from DFT calculations, for different adsorption geometries. Positive adsorption energy indicates that the adsorption is unfavourable, whilst a negative value indicates that adsorption is likely, with the lowest value being the most stable. Letters in parentheses refer to the Bi atom adsorption sites shown in Fig. 1.

Adsorption site	*R*-factor (1st stage)	*R*-factor (final)	Adsorption energy (eV)
Top (A)	0.52		0.414
Hollow (B)	0.54		0.198
Hollow (C)	0.50		0.234
Bridge (D)	0.41		0.208
Faulted surface alloy	0.58		−0.354
Surface alloy	0.27	0.16	−0.353
Pendry variance	0.04		

Table 2
Structural and non-structural parameters from LEED and DFT analyses. *d*(Bi–Ag) is the bond length between Bi and Ag atoms in the first layer, dz(Ag–Bi) is the vertical distance between the 1st layer of Ag atoms and the Bi atoms (Bi is above Ag), dz/dz$_{bulk}$ (Ag*i*–Ag*j*) is the change in the vertical distance between the centres of mass of Ag layers *i* and *j* (negative means contraction). Δ (Ag4) is the buckling in the 4th substrate layer where the Ag atoms directly below the Bi atoms are pulled up slightly. Using a bulk interlayer spacing for clean Ag(111) of 2.35 Å, the LEED results show that the overall structure remains bulk like within the errors.

Parameter	LEED	DFT
d(Ag–Bi) [Å]	2.95 ± 0.05	3.01
dz(Ag–Bi) [Å]	0.57 ± 0.05	0.61
dz/dz$_{bulk}$(Ag1–Ag2) [%]	−1 ± 1	−1
dz/dz$_{bulk}$(Ag2–Ag3) [%]	−1 ± 1	0
dz/dz$_{bulk}$(Ag3–Ag4) [%]	−1 ± 2	−1
dz/dz$_{bulk}$(Ag4–Ag5) [%]	−1 ± 2	0
Δ (Ag4) [Å]	0.02 ± 0.05	0.02
Debye T (Bi) [K]	80	
Debye T (Ag1) [K]	160	
Debye T (Ag bulk) [K]	225	
$V_{imaginary}$ [eV]	−4.5	
l_{max}	13	
Ag bulk lattice constant [Å]	4.09	4.17

First-principle DFT calculations were performed for the bismuth on Ag(111) system to verify and analyze the experimental results presented in this paper. The static calculations for total energies were performed using the Vienna ab-initio simulation package (VASP) [32–35] including the projector augmented wave (PAW) [36] potentials. A kinetic energy cut-off of 400 eV was applied for the plane waves, which was found to produce converged results for both Ag and Bi, for all the structures. For the exchange correlation potential the generalized gradient approximation (GGA) of the Perdew-Wang 91 (PW91) [37] was employed. The 10 × 8 × 1 Monkhorst–Pack mesh [38] was used for k-point sampling. The Ag surface was modelled using the supercell approach, where periodic boundary conditions are applied to the central supercell so that it is reproduced periodically throughout xy-space. The surface slab was modelled with 6 layers of Ag atoms. A region of approximately 10 Å of vacuum was inserted in the *z* direction to prevent interactions occurring between periodic images. The bottommost layer of the surface slab was frozen during the geometry relaxation.

Adsorption energies of Bi atom are defined as:

$$E_{ads} = 1/N_{Bi}\, x\, (E_{tot} - E_{clean} - N_{Bi}\, x\, E_{Bi}) \tag{1}$$

where E_{tot} is total energy of relaxed Ag/Bi supercell, E_{clean} is the total energy of the relaxed clean Ag slab, N_{Bi} is the number of Bi atoms and E_{Bi} is the energy of one atom in the Bi bulk.

For substitutional alloy structures the adsorption energy is defined as:

$$E_{ads} = 1/N_{Bi}\, x \left(E_{tot} - E_{clean} - N_{Bi}\, x\, E_{Bi} + N_{Bi}\, x\, E_{Ag\text{-}bulk}\right) \tag{2}$$

where, $E_{Ag\text{-}bulk}$ is the total energy of an Ag bulk atom.

An Ag lattice constant of 4.17 Å was used, which was obtained from bulk cell optimization using the same computational parameters. The six structural models used in the LEED I–V analysis were considered in the DFT analysis. The adsorption energies for each site for the models that showed convergence in the calculations are listed in Table 1. Of the overlayer geometries, the fcc hollow site is the most favourable, albeit with small energy difference between the two

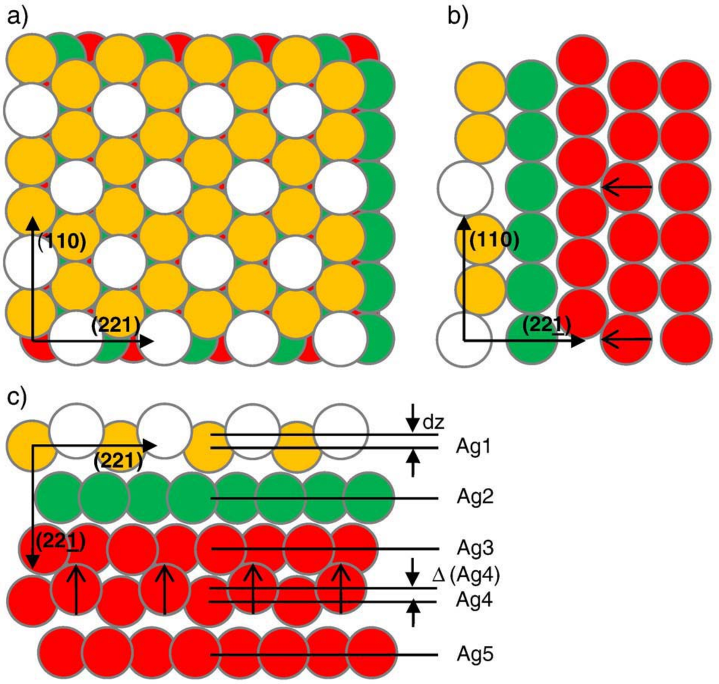

Fig. 3. Large white circles represent the Bi atoms that substitute Ag atoms in the top layer. (a) Top view of the favoured structure. Top three layers of the slab are shown. (b, c) Side views showing the top five layers. The arrows show the buckling in the 4th substrate layer as the Ag atoms directly below the Bi are displaced vertically up.

hollows and the bridge sites. On the other hand, both the substitutional and faulted surface alloy structures were found to be the most stable with an adsorption energy of -0.353 eV. The geometrical parameters for the relaxed substitutional surface alloy structure are listed in Table 2 and compare well with the LEED data.

While the LEED analysis unambiguously favours the unfaulted substitutional surface alloy, the DFT calculations only confirm that the structure is a surface alloy and does not distinguish between the faulted structure, where all the top surface atoms (Bi and Ag) have moved into hcp hollow sites, and the unfaulted surface alloy, where the surface atoms remain in fcc hollow sites. One possible reason why our DFT calculations fail to distinguish between the two structures is the use of the finite size of the slab (6 layers). Indeed, in an earlier DFT calculation by Woodruff and Robinson [22] for the Sb–Ag(111) system, they find that the stacking fault energy is sensitive to the slab thickness and suggest that these calculations are only realistic using much larger scale parallel computing systems beyond our means. It is also worth noting that even for the clean Ag(111) surface, they find that there is a negligible difference in energy between the surface faulted and unfaulted structures. Our calculation for the clean Ag(111) shows that the energy difference between the faulted and unfaulted Ag surface is only 20 meV, similar to what has previously been reported [22]. This implies that on Ag(111), a stacking fault surface structure could easily be facilitated. In fact for Sb on Ag(111), both faulted and unfaulted $\left(\sqrt{3}\times\sqrt{3}\right)R30^\circ$ structures have been found, as well as evidence for subsurface stacking faults, attributed to some subtle influence of subsurface Sb. For the Bi on Ag(111) case, we have only found the unfaulted $\left(\sqrt{3}\times\sqrt{3}\right)R30^\circ$ structure, suggesting perhaps that Bi, with its larger atomic size compared to Sb, does not easily diffuse into the subsurface region. Another factor could be that there is a thermal activation barrier in moving all the surface atoms from the fcc hollow sites to the hcp hollow sites. In fact the Sb on Ag(111) structures were formed by dosing and annealing to elevated temperatures while in our case, sharp $\left(\sqrt{3}\times\sqrt{3}\right)R30^\circ$ Bi on Ag(111) structure was readily formed by dosing at room temperature.

The substitutional and faulted surface alloy structures were further investigated theoretically by molecular dynamic calculations. The calculations were performed by fixing the surface temperature at 300 K, and the ionic moves were performed with the interval of 1 fs. The total duration of molecular dynamic runs was 1 ps. The relaxed atomic positions were used as initial coordinates for the molecular dynamics. In the beginning of each molecular dynamics run, random velocities were assigned to the slab atoms according to the temperature distribution. The bottommost atoms of the slab were kept fixed. The results of the molecular dynamics show that both of the structures, surface alloy and faulted surface alloy, are stable at room temperature, as found in the DFT calculations. Both calculations were tested with several random velocities for the slab atoms, and the results remained the same. Moreover, the adsorption energies stayed within the same interval in both cases during the molecular dynamics run.

Both the LEED and DFT analyses show that in the stable substitutional surface alloy structure, there is a slight ‘rumpling’ of the surface due to the larger Bi atoms located about 0.6 Å above the surface plane of the Ag atoms. This amplitude of the ‘rumpling’ is smaller by about 0.24 Å than that predicted by a simple touching hard-spheres model based on bulk metallic radii (1.44 Å for Ag and 1.56 Å for Bi). This suggests a reduction in the effective radii similar to that found by Quinn et al. [6] in their LEED study of the substitutional surface alloy structure for the Pb–Ni(111) system. It has been suggested that the reduction in the effective radii may be attributed to the influence of valance electron charge smoothing and associated surface stress effects [6,21,23]. A similar effect is possibly the case for the Bi–Ag(111) structure in our study.

4. Conclusions

There is very good agreement between the geometrical parameters extracted from LEED I–V and DFT analyses. LEED analysis shows that the Bi atoms are found to replace one top layer Ag atom in each unit cell, forming a substitutional unfaulted surface alloy. DFT calculations show that the stable $\left(\sqrt{3}\times\sqrt{3}\right)R30^\circ$ structure is a surface alloy, but does not distinguish between a faulted and unfaulted structure, possibly due to limitation of using a finite size slab. Because of the size difference between the Ag and Bi atoms (Bi is approximately 5% larger than Ag), the top layer is corrugated such that the Bi atoms reside about 0.6 Å above the Ag atoms. The amplitude of this 'rumpling' is smaller than what would be predicted on a simple touching hard-spheres model. The interlayer spacings, calculated with respect to the centres of mass of the Ag atoms, remain bulk like in both DFT and LEED analyses.

Acknowledgements

I.M.M. wishes to thank EPSRC for their funding via a studentship.

A.M., M.L. and K.P. would like to thank National Graduate School in Materials Physics and Academy of Finland for funding, and CSC – IT Centre for Sciences Ltd., for computational resources.

References

[1] D.F. Li, H.Y. Xiao, X.T. Zu, H.N. Dong, Phys. B 392 (2007) 217.
[2] J.L. Nie, H.Y. Xiao, X.T. Zu, F. Gao, Chem. Phys. 326 (2006) 308.
[3] H.Y. Xiao, X.T. Zu, X. He, F. Gao, Chem. Phys. 325 (2006) 519.
[4] V.B. Nascimento, R. Paniago, A. de Siervo, C.M.C. de Castilho, R. Landers, E.A. Soares, V.E. de Carvalho, Surf. Sci. 572 (2004) 337.
[5] A. Krupski, S. Mroz, Surf. Rev. Lett. 10 (2003) 843;
Surf. Rev. Lett. 10 (2003) 65.
[6] P.D. Quinn, C. Bittencourt, D.P. Woodruff, Phys. Rev. B 65 (2002) 233404.
[7] Ph. Hofmann, Prog. Surf. Sci. 81 (2006) 191.
[8] J.H. Xu, E.G. Wang, C.S. Ting, W.P. Su, Phys. Rev. B 48 (1993) 17271.
[9] F.Y. Yang, K. Liu, K. Hong, D.H. Reich, P.C. Searson, C.L. Chien, Science 284 (1999) 1335.
[10] M.R. Black, P.L. Hagelstein, S.B. Cronin, Y.M. Lin, M.S. Dresselhaus, Phys. Rev. B 68 (2003) 235417.
[11] H.L. Zhang, W. Chen, X.S. Wang, J. Yuhara, A.T.S. Wee, Appl. Surf. Sci. 256 (2009) 460.
[12] K. Takayanagi, D.M. Kolb, K. Kambe, G. Lehmpfuhl, Surf. Sci. 100 (1980) 407.
[13] A. Rolland, J. Bernardini, M.G. Barthes-Labrousse, Surf. Sci. 143 (1984) 579.
[14] J. Dalmas, H. Oughaddou, C. Le´andri, J.-M. Gay, G. Le Lay, G. Treglia, B. Aufray, O. Bunk, R.L. Johnson, Phys. Rev. B 72 (2005) 155424.
[15] J. Dalmas, H. Oughaddou, G. Le Lay, B. Aufray, G. Treglia, C. Girardeaux, J. Bernardini, J. Ujii, G. Panaccione, Surf. Sci. 600 (2006) 1227.
[16] D. Pacilé, C.R. Ast, M. Papagno, C. Da Silva, L. Moreschini, M. Falub, A.P. Seitsonen, M. Grioni, Phys. Rev. B 73 (2006) 245429.
[17] S.A. de Vries, W.J. Huisman, P. Goedtkint, M.J. Zwanenburg, S.L. Bennett, I.K. Robinson, E. Vlieg, Surf. Sci. 414 (1998) 159.
[18] E.A. Soares, C. Bittencourt, V.B. Nascimento, V.F. Carvalho, C.M.C. de Castilho, C.F. McConville, A.V. de Carvalho, D.P. Woodruff, Phys. Rev. B 61 (2000) 13983.
[19] T.C.Q. Noakes, D.A. Hutt, C.F. McConville, D.P. Woodruff, Surf. Sci. 372 (1997) 117.
[20] P. Bailey, T.C.Q. Noakes, D.P. Woodruff, Surf. Sci. 426 (1999) 358.
[21] P.D. Quinn, D. Brown, D.P. Woodruff, P. Bailey, T.C.Q. Noakes, Surf. Sci. 511 (2002) 43;
D.P. Woodruff, et al., Current Applied Physics 3 (2003) 19.
[22] D.P. Woodruff, J. Robinson, J. Phys. Condens. Matter 12 (2000) 7699.
[23] D. Brown, P.D. Quinn, D.P. Woodruff, P. Bailey, T.C.Q. Noakes, Phys. Rev. B61 (2000) 7706.
[24] D. Kaminski, P. Poodt, E. Aret, N. Radenovic, E. Vlieg, Phys. Rev. Lett. 96 (2006) 056102.
[25] D.F. Li, H.Y. Xiao, X.T. Zu, H.N. Dong, Physica B392 (2007) 217.
[26] F. Meier, H. Dil, J. Lobo-Checa, L. Patthey, J. Osterwalder, Phys. Rev. B 77 (2008) 165431.
[27] C.R. Ast, J. Henk, A. Ernst, L. Moreschini, M.C. Falub, D. Pacilé, P. Bruno, K. Kern, M. Grioni, Phys. Rev. Lett. 98 (2007) 186807 [see also Cond-Mat. Mtrl-Sci./0509509.].
[28] K. He, T. Hirahara, T. Okuda, S. Hasegawa, A. Kakizaki, I. Matsuda, Phys. Rev. Lett. 101 (2008) 107604.
[29] M.A. Van Hove, W. Moritz, H. Over, P.J. Rous, A. Wander, A. Barbieri, N. Materer, U. Starke, G.A. Somorjai, Surf. Sci. Rep. 19 (1993) 191.
[30] A. Barbieri and M. A. Van Hove, private communication.
[31] J.B. Pendry, J. Phys. C Solid State Phys. 13 (1980) 937.
[32] G. Kresse, J. Hafner, J. Phys. Condens. Matter 6 (1994) 8245.
[33] G. Kresse, J. Furthmüller, Comput. Mat. Sci. 6 (1996) 15.
[34] G. Kresse, J. Furthmüller, Phys. Rev. B 54 (1996) 11169.
[35] G. Kresse, J. Joubert, Phys. Rev. B 59 (1999) 1758.
[36] P.E. Blöchl, Phys. Rev. B 50 (1994) 17953.
[37] J.P. Perdew, Y. Wang, Phys. Rev. B 45 (1992) 13244.
[38] H.J. Monkhorst, J.D. Pack, Phys. Rev. B 13 (1976) 5188.

Publication V

K.H.L. Zhang, I.M McLeod, Y.H. Lu, V.R. Dhanak, A. Matilainen, M. Lahti, K.Pussi, R.G. Egdell, X.-S. Wang, A.T.S. Wee and W. Cheng "Observation of a surface alloying to de-alloying transition during growth of Bi on Ag(111)"

PHYSICAL REVIEW B **83**, 235418 (2011)

Observation of a surface alloying-to-dealloying transition during growth of Bi on Ag(111)

K. H. L. Zhang,[1,2,*] I. M. McLeod,[3] Y. H. Lu,[1] V. R. Dhanak,[3] A. Matilainen,[4] M. Lahti,[4] K. Pussi,[4] R. G. Egdell,[2]
X.-S. Wang,[1] A. T. S. Wee,[1] and W. Chen[1,5,†]
[1]*Department of Physics, National University of Singapore, 2 Science Drive 3, 117542, Singapore*
[2]*Department of Chemistry, Chemistry Research Laboratory, Mansfield Road, Oxford OX1 3TA, United Kingdom*
[3]*Department of Physics, University of Liverpool, Liverpool L69 3BX, United Kingdom*
[4]*Department of Mathematics and Physics, Lappeenranta University of Technology, P.O. Box 20, FIN-53851 Lappeenranta, Finland*
[5]*Department of Chemistry, National University of Singapore, 3 Science Drive 3, 117543, Singapore*

(Received 30 November 2010; revised manuscript received 11 April 2011; published 14 June 2011)

The atomic structures that develop as a function of coverage during deposition of Bi on Ag(111) have been studied using low-temperature scanning tunneling microscopy, low-energy electron diffraction, and *ab initio* calculations. The growth process involves two sequential stages. At low coverage, Bi atoms are incorporated into the topmost layer of Ag(111), resulting in the formation of an Ag_2Bi alloy confined to the surface and ordered $(\sqrt{3}\times\sqrt{3})R30^\circ$ Ag_2Bi islands supported on Ag(111). This mode of accommodation of Bi was found to be energetically favorable based on *ab initio* total-energy calculations. At coverage above a critical value of 0.55 monolayers, the Ag_2Bi alloy phase gradually converts into an ordered Bi $(p\times\sqrt{3})$ overlayer structure supported on Ag(111). We postulate that the dealloying transition is likely driven by compressive strain induced by incorporation of large-size Bi atoms into Ag at a high coverage and the subsequent lack of miscibility of Ag and Bi bulk phases. After completion of the dealloying process, Bi(110) thin films can be grown epitaxially on top of Ag(111) with a chemically abrupt interface.

DOI: 10.1103/PhysRevB.83.235418 PACS number(s): 68.55.−a, 68.43.−h, 68.47.−b, 68.37.−d

I. INTRODUCTION

The study of the heteroepitaxial growth of metals on metallic substrates has been motivated by the demand for high-quality thin metallic heterostructures with sharp interfaces in technological applications such as magnetic data storage and spintronics.[1–3] It is becoming clear that a wealth of complex phenomena may arise at an atomic scale that are not predicted from simple thermodynamic considerations of the respective surface and interface energies of the metal adatoms and the substrates.[4–7] Tersoff has predicted that surface-confined alloy phases may arise as an alternative to overlayer structures as a means to relieve the surface stress in systems dominated by an atomic size mismatch, even in cases where the metals are immiscible in the bulk.[8] This is particularly the case for the growth of comparatively heavier elements such as lead (Pb), antimony (Sb), and bismuth (Bi) on noble-metal surfaces.[8–13] Surface alloying is a powerful way of developing unique physical and chemical properties in alloys that do not have a bulk counterpart.[14–16] Elegant examples include the exceptionally large spin-orbit splittings of surface states in surface alloys between heavy elements such as Bi or Pb on light metals such as Cu and Ag, which opens potential applications in the area of spintronics.[17,18]

Bi is a typical group-V element and adopts a rhombohedra $A7$ lattice belonging to the space group $R\bar{3}m$. There are two atoms per unit cell, which can also be described by a hexagonal basis.[19] The band structure of Bi is that of a semimetal with an overlap of ∼ 40 meV between valence and conduction bands that arises due to a slight distortion along the trigonal axis, which is (111) in the rhombohedra basis or (0001) in the hexagonal basis. Bi possesses an unusual array of physical properties, including low carrier density, a long Fermi wavelength (∼ 40 nm at room temperature), and high carrier mobility. Most interestingly, the low-index surfaces of Bi such as Bi(111), Bi(100), and Bi(110) show very different electronic properties from the bulk associated with spin-orbit (SO) splitting at the surface due to the breakdown of inversion symmetry (the so-called Rashba-Bychkov effect).[19–21]

It has been recently reported that submonolayer Bi on Ag(111) forms a $(\sqrt{3}\times\sqrt{3})R30^\circ$ surface alloy.[17] The $(\sqrt{3}\times\sqrt{3})R30^\circ$ structure is of particular interest because the intermixing of the size mismatched atoms and the corresponding in-plane potential variations lead to giant SO splitting, which has implications for spintronics applications.[17,22,23] Nonetheless, a detailed investigation of the atomic structures of these two-dimensional (2D) surface alloys is still lacking, even though such structural information plays a critical role in determining the in-plane potential gradient, and thus the SO splitting of the surface alloys.[24] Furthermore, a similar class of electronic states evolves by the quantum confinement of electrons in ultrathin films with a thickness comparable to the electron coherence length, to give so-called quantum well states. It has been recently reported that a giant SO splitting of quantum well states has been observed within a Bi monolayer on Cu(111).[25] Based on first-principles calculations, the authors argued that the huge SO splitting originated from the perpendicular potential at the surface and interface of the ultrathin Bi film. This finding opens the possibility of controlling the SO splitting by tuning the nanostructure of the ultrathin film.

In the present work, we present a detailed study of the nucleation of Bi on Ag(111), the subsequent development of the Ag_2Bi surface alloy, and the growth of a Bi thin film on Ag(111) using scanning tunneling microscopy (STM) and *ab initio* total-energy calculations. We show that in the initial stages of deposition Bi atoms are incorporated into the topmost Ag(111) layer by exchanging with the surface Ag atoms to form a substitutional surface alloy. This mode of incorporation was found to be energetically favorable based on *ab initio* total-energy calculations. However, a surface dealloying process ensues with increasing Bi coverage, presumably driven by the high compressive strain induced by incorporation of larger-size Bi atoms into the Ag matrix at high concentrations. For coverages above 1 monolayer (ML), the Ag_2Bi surface alloy demixes and a highly ordered Bi(110) monolayer is formed on top of Ag(111).

II. EXPERIMENTAL AND COMPUTATIONAL METHODS

The experiments were carried out in a homebuilt multichamber ultrahigh vacuum (UHV) system with a base pressure of better than 2×10^{-10} mbar incorporating an Omicron low-temperature scanning tunneling microscope (LT-STM) stage.[26] The STM was operated with a Nanonis controller (Nanonis, Switzerland). Ag(111) substrates were cleaned by repeated cycles of Ar^+ sputtering and annealing at 800 K. The cleanliness and surface order of the samples was checked by LT-STM images, which in the final stages of cleaning showed sharp step edges and smooth terraces without obvious signs of impurities. Bi was thermally evaporated from a Knudsen cell in a growth chamber with a base pressure of better than 3×10^{-10} mbar. The Bi deposition rate was calibrated using a quartz microbalance (QCM) and was set at 0.05 ML/min, where 1 ML is defined as 1 atomic layer of Bi(110), i.e., 9.3×10^{14} atoms cm^{-2}. STM images were obtained at 77 K in constant-current mode with a chemically etched tungsten tip. Additional low-energy electron diffraction (LEED) experiments were performed in a standard UHV surface science chamber with rear view LEED optics from OCI Vacuum Microengineering.

The static calculations of total energies were performed using density functional theory (DFT) as implemented in the Vienna *ab initio* simulation package (VASP),[27,28] including the projector augmented-wave (PAW) potentials.[29] A kinetic energy cutoff of 400 eV was applied to the plane waves, which was found to produce well-converged results for both Ag and Bi. The exchange correlation potential employed the generalized gradient approximation (GGA) of the Perdew-Wang 91 (PW91).[30] A $10 \times 8 \times 1$ Monkhorst-Pack mesh was used for k-point sampling.[31] The Ag surface was modeled using a supercell approach with thin slabs separated by vacuum spacings. Periodic boundary conditions were applied to the central supercell so that it was reproduced periodically throughout xy space. The periodic slab was modeled with six layers of Ag atoms. A region of ~ 10 Å of vacuum was inserted in the z direction to prevent interactions between periodic images. The SO coupling has not been switched on in the VASP calculation. We have tested that the SO coupling did not have significant effect on the resulting structures. The bottommost layer of the surface slab was frozen during the geometry relaxation. An Ag lattice constant of 4.17 Å was used, which was obtained from bulk cell optimization using the same computational parameters.

III. RESULTS AND DISCUSSION

A. Surface alloying at low coverage

Figure 1(a) shows a large-area STM image following deposition of 0.2 ML of Bi on a clean Ag(111) surface at room temperature. It reveals dispersed protrusions (marked P), large meandering two-dimensional (2D) islands (marked LI), and small compact islands (marked SI). The high-resolution STM image of Fig. 1(b) indicates that the protrusions have a spherical shape with a diameter of ~ 4 Å. The apparent height between the protrusion and the surrounding Ag terrace is ~ 0.3 Å, as seen by the line profile in Fig. 1(c). These features are associated with Bi atoms incorporated into the topmost layer of Ag(111) by an exchange process which involves substitution of substrate Ag atoms by Bi atoms. The surface Bi protrusion is expected on the basis of a simple hard-sphere picture because the bulk metallic radii of Bi (1.56 Å) is larger than that of Ag (1.44 Å). This process results in the formation of a Bi-Ag alloy confined in the surface. It is noted that the substitutional Bi atoms are randomly distributed among the available Ag lattice sites.

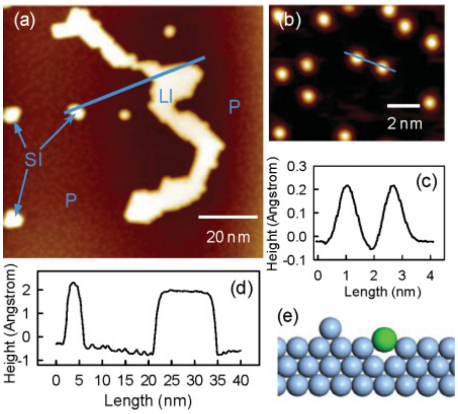

FIG. 1. (Color online) (a) An overview of large-scale STM images of 0.2 ML Bi deposited on Ag(111) ($V_s = -1.8$ V, $I_t = 0.2$ nA), showing dispersed protrusions (marked P), large meandering islands (marked LI), and small compact islands (marked SI). (b) High-resolution STM image of the disperse protrusions. (c) A line profile along the line in (b). (d) A line profile along the line in (a). (e) Schematic model for the incorporation of Bi (green) in an Ag lattice (navy).

In contrast, the line profiles in Fig. 1(d) indicate that the apparent topographic height of the meandering islands (LI) and small islands (SI) is 2.5 Å, corresponding to the height of an island one atomic layer thick. Atomically resolved STM images such as those shown in Fig. 2(a) reveal that both islands have an ordered hexagonal lattice with a $(\sqrt{3} \times \sqrt{3})R30^\circ$ superstructure ($\mathbf{a} \sim 5$ Å), where the periodicity is defined in terms of the Ag(111) substrate surface. Based on these observations, we speculate that these islands contain a 2D Bi-Ag alloy layer and that the alloy layer is formed from Ag atoms that are displaced from the surface layer by Bi atoms along with nonembedded Bi adatoms found on the Ag(111) surface. A schematic model of the proposed structure is shown in Fig. 3(a). The formation of this structure involves the following steps. First, deposited Bi atoms embed themselves into the topmost Ag layer to form a dilute substitutional alloy. One Ag atom is displaced out of the surface for each Bi atom

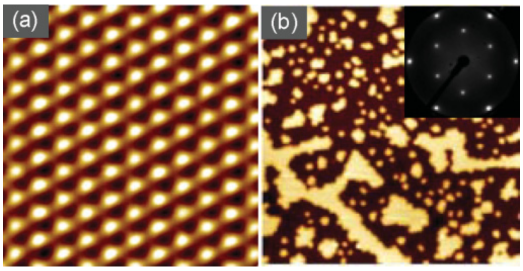

FIG. 2. (Color online) (a) High-resolution 5 nm × 5 nm STM image ($V_s = 1.2$ and $I_t = 0.18$ nA) from the top of a large meandering island, showing the supported Ag_2Bi surface alloy with an ordered $(\sqrt{3} \times \sqrt{3})R30^\circ$ superstructure (the bright spots are associated with Bi atoms). (b) Large-scale STM image (100 nm×100 nm) of 0.4 ML Bi deposited on Ag(111). The inset shows the LEED pattern of the $(\sqrt{3} \times \sqrt{3})R30^\circ$ structure with an electron beam energy of 42 eV.

that is incorporated. The Ag adatoms then diffuse and coalesce with nonembedded Bi adatoms to form the ordered Ag_2Bi alloy islands on top of Ag(111). We did not observe any pure Ag islands formed by nucleation of the displaced Ag adatoms, which indicates that these adatoms are stabilized in the form of ordered $(\sqrt{3} \times \sqrt{3})R30^\circ$ islands. Hence one might expect a direct correlation between the numbers of embedded Bi atoms and the surface area covered by $(\sqrt{3} \times \sqrt{3})R30^\circ$ islands, given that each $(\sqrt{3} \times \sqrt{3})R30^\circ$ unit cell contains one Bi and two ejected Ag atoms. Indeed, statistical analysis reveals that the density of substitutional Bi atoms is roughly identical to the density of Ag atoms in the ordered alloy islands. Furthermore, both the density of the embedded Bi atoms and the surface area of $(\sqrt{3} \times \sqrt{3})R30^\circ$ islands increase linearly with the amount of Bi deposited. As shown in Fig. 2(b), with 0.4-ML Bi deposition most of the Ag surface is covered with Ag_2Bi surface alloy islands. At this stage a well-defined $(\sqrt{3} \times \sqrt{3})R30^\circ$ LEED pattern can be observed, as shown in the inset of Fig. 2(b).

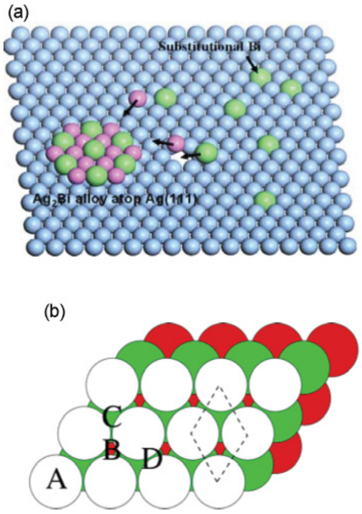

FIG. 3. (Color online) (a) Schematic of the formation of the Ag_2Bi surface alloy: Ag lattice (navy), Bi atoms (green), and squeezed Ag atoms (pink). (b) The four adsorption sites (A = top, B and C = hollow, and D = bridge) considered in DFT calculations. The corresponding adsorption energies are given in Table I. The white spheres represent the first Ag layer, the green spheres represent the layer, and the red spheres represent the third layer.

The phenomenon of alloy formation confined to a surface layer has been identified in many other heteroepitaxial systems, including those where there is bulk miscibility such as Ag/Cu(100),[32] In/Cu(100),[33] and Au/Fe(100),[34] as well as in systems where the two components are immiscible in the bulk such as Au/Ni(110) (Ref. 4) and Sb/Ag(111).[11] According to the theoretical study by Tersoff,[8] for systems dominated by atomic size mismatch, surface strain effects can favor alloying on a surface even though strain suppresses intermixing in the bulk. Clean metallic surfaces are normally under tensile stress due to broken bonds at the surface.[34] Thus the incorporation of large atoms into the surface is an efficient way to relieve the surface tensile stress. Theoretical calculations based on the embedded atom method (EAM) indicated that Ag(111) has a tensile surface stress of 0.6 eV $Å^{-2}$.[35] Therefore, the tensile surface stress can be effectively relaxed by the incorporation of the large Bi atom (metallic radii = 1.56 Å) into the Ag (1.44 Å) lattice. This is despite the fact that the surface energy for Bi(110), $\gamma_{Bi}(110) = 0.541$ J m^{-2}, is much smaller than the surface energy for Ag(111), $\gamma_{Ag}(111) = 1.17$ J m^{-2}, which would appear to favor formation of a Bi overlayer structure on Ag(111).[36] Similar considerations also explain the preference for substitutional Bi atoms to be distributed within the Ag lattice without any clustering. Because of the larger size of Bi, the incorporation of Bi atoms into the Ag lattice can induce local strain fields, which causes two nearest-neighbor embedded atoms to repel each other in the surface. Thus the embedded Bi atoms never have Bi nearest neighbors. Recent *ab initio* studies of the 3*d* transition metals on Au(100) also showed a repulsive interaction between nearest-neighbor embedded atoms, thus explaining the random distribution of the embedded impurities.[37] By contrast, the local strain can be effectively relieved in the Ag_2Bi alloy overlayer because of the finite size of the alloy islands supported on the Ag substrate.

However, the model proposed by Tersoff takes into account only the strain energy of the system.[8] The equilibrium structure will be determined by minimization of the total energy and not just the surface strain energy. Therefore, we performed first-principles DFT calculations to compare the energies of adsorption and incorporation for Bi on Ag(111) at various sites, including on-top, hollow, and bridge adsorption sites as well substitutional sites, as indicated in Fig. 3(b).[38] The adsorption energies of Bi atom are defined as

$$E_{ads} = \frac{1}{N_{Bi}}(E_{tot} - E_{clean} - N_{Bi}E_{Bi}), \qquad (1)$$

where E_{tot} is the total energy of a relaxed Ag/Bi supercell; E_{clean} is the total energy of the relaxed clean Ag slab; N_{Bi} is the number of Bi atoms and E_{Bi} is the energy of one atom in

TABLE I. Adsorption energies for different adsorption sites as indicated in Fig. 3(b).

Adsorption site	Adsorption energy (eV)
Top (A)	0.414
Hollow (B)	0.198
Hollow (C)	0.234
Bridge (D)	0.208
Surface alloy	−0.353

the bulk of the Bi metal. For substitutional alloy structures the adsorption energy is defined as

$$E_{\mathrm{ads}} = \frac{1}{N_{\mathrm{Bi}}}(E_{\mathrm{tot}} - E_{\mathrm{clean}} - N_{\mathrm{Bi}}E_{\mathrm{Bi}} + N_{\mathrm{Bi}}E_{\mathrm{Ag\text{-}bulk}}), \qquad (2)$$

where $E_{\mathrm{Ag\text{-}bulk}}$ is the total energy of an Ag bulk atom. The adsorption energies for each site of the models that showed convergence in the calculations are listed in Table I. The fcc hollow site B is the most favorable for absorption, albeit with a small energy difference between the two possible hollow sites and the bridge sites. However, the substitutional surface alloy structure was found to be the most stable configuration, with an absorption energy of −0.353 eV. There is thus a clear preference for the occupation of substitutional sites in the surface layer. The DFT calculations also indicate that the "rumpling" of the surface alloy has an amplitude of 0.6 Å, with the Bi atoms sitting above the underlying Ag surface atoms. This is in good agreement with a recent structural determination of the $(\sqrt{3} \times \sqrt{3})R30^\circ$ surface structure of the $\mathrm{Ag_2Bi}$ alloy layer by the analysis of LEED curves.[38] The rumpling amplitude is larger than the apparent protrusion height measured by STM. This can be explained by the fact that the apparent height in a STM image depends on both the topographic height and the density of electronic states near the Fermi level. This amplitude is, however, smaller by ∼0.24 Å than that predicted by a simple hard-sphere model based on bulk metallic radii of 1.44 Å for Ag and 1.56 Å for Bi. This suggests a reduction in the effective radii that is similar to that found by Quinn *et al.*[12] in their LEED study of the substitutional surface alloy structure for the Pb-Ni(111) system. It has been suggested that the reduction in the effective radii may be attributed to the influence of valence electron charge smoothing and associated surface stress effects. A similar effect is possibly the case for the Bi-Ag(111) structure in our study.

B. Dealloying and the Bi overlayer structure

The Bi surface alloy saturates at coverage of 0.5 ML, which corresponds to 0.33 ML if defined in terms of atomic layers of Ag(111) with a sheet density of 1.38×10^{15} cm^{-2}. With additional Bi deposition, the Bi-Ag system undergoes a dealloying process. Figures 4(a) and 4(b) show STM images which trace the evolution of the dealloying process as the Bi coverage increases. In Fig. 4(a) the Bi coverage is slightly above the saturation limit, and a different type of island begins to appear with a lower height above the surface than the $(\sqrt{3} \times \sqrt{3})R30^\circ$ alloy islands. These are labeled DA in the figure. As will be discussed below, these different islands have $\sqrt{3}$ periodicity along the Ag$[11\bar{2}]$ direction, but are incommensurate in the orthogonal direction. Following notation introduced by Chen *et al.*,[39] this structure is designated as $(p \times \sqrt{3})$. The authors used an electrochemical deposition technique and found that p depended on the deposition potential, hence the choice of this letter. The switchover of the structure developed further as the Bi coverage was increased to 0.75 ML [Fig. 4(b)]. Clearly, both the island size and the total coverage by the $(p \times \sqrt{3})$ overlayer islands increase dramatically, whereas the area of the $(\sqrt{3} \times \sqrt{3})R30^\circ$ islands and substitutional surface alloy decreases. Figure 4(c) shows a height profile along the line marked in Fig. 4(b), indicating that the apparent height of the $(p \times \sqrt{3})$ overlayer is 1.8 Å with respect to the substituted surface alloy and is thus 0.7 Å lower than that of the $(\sqrt{3} \times \sqrt{3})R30^\circ$ islands. A high-resolution image is shown in Fig. 4(d). This reveals the atomic structure within the $(p \times \sqrt{3})$ islands and suggests that this overlayer is based on a rectangular nonprimitive unit cell. The unit cell vectors are $\mathbf{a}_1 = 5.0$ Å along the Ag$[11\bar{2}]$ direction and $\mathbf{b}_1 = 4.7$ Å along the Ag$[1\bar{1}0]$ direction. Figure 4(e) shows a LEED

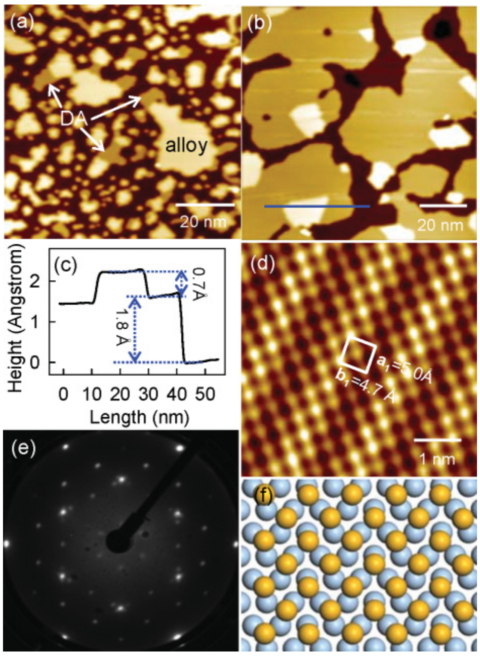

FIG. 4. (Color online) (a) Large-scale STM image of 0.6 ML Bi deposited on Ag(111), showing the appearance of $(p \times \sqrt{3})$ overlayers with a low height at the step edges of $(\sqrt{3} \times \sqrt{3})R30^\circ$ islands (labeled as "DA"). (b) The coverage of the $(p \times \sqrt{3})$ overlayers increases as 0.75 ML Bi was deposited on Ag(111). (c) A line profile along the line in (b), indicating that the height of the $(p \times \sqrt{3})$ overlayer is 1.8 Å with respect to the substituted surface alloy and 0.7 Å lower than that of the $(\sqrt{3} \times \sqrt{3})R30^\circ$ islands. (d) Atomic structure of the $(p \times \sqrt{3})$ overlayer structure with lattice constants of $\mathbf{a}_1 = 5.0$ Å, $\mathbf{b}_1 = 4.7$ Å. (e) LEED pattern (with an electron energy of 38 eV) for the $(p \times \sqrt{3})$ overlayer. (f) Schematic model for the $(p \times \sqrt{3})$ Bi overlayers (yellow) on Ag(111) (navy).

pattern measured with an electron energy of 38 eV for the $(p \times \sqrt{3})$ overlayer. It further confirms that the $\mathbf{a}_1$ direction of the Bi overlayer structure is commensurate with the Ag(111) surface along the Ag$[11\bar{2}]$ direction $(\mathbf{a}_1 = a_{\mathrm{Ag}}\sqrt{3})$, but incommensurate along the Ag$[1\bar{1}0]$ direction. Because of the threefold symmetry of the Ag(111) surface, there are three coexisting domains of the rectangular structures rotated 120° and 240° with respect to each other. The $(p \times \sqrt{3})$ overlayer structure is similar to a Bi $(p \times \sqrt{3})$ overlayer structure on Au(111) formed by electrochemical deposition.[39] The lattice constants are slightly larger than those found in the Bi(110) planes of elemental bismuth, where $(\mathbf{a}_2 = 4.74$ Å, $\mathbf{b}_2 = 4.54$ Å), so that the atomic density of 8.0×10^{14} cm^{-2} is also lower than in the Bi metal. A modulation with an amplitude of 0.2 Å is seen to be superimposed on the ordered Bi overlayer structures along the Ag$[1\bar{1}0]$ direction. This modulation is straightforwardly explained as a moiré pattern arising from the interference between the Bi overlayer and the Ag substrate along the $[1\bar{1}0]$ direction. We thereby identify the $(p \times \sqrt{3})$ islands as pure Bi overlayers formed during the dealloying process sitting on top of Ag(111). A structural model for the $(p \times \sqrt{3})$ overlayer based on the atomic resolution image is proposed in Fig. 4(f). At a coverage of 0.9 ML, we found that there is complete coverage of the surface by the $(p \times \sqrt{3})$ overlayer so that the dealloying process is complete.

Dealloying transitions similar to those found here have been observed in several other systems including Pd/Cu(111),[40] In/Cu(100),[32] Mn/Cu(001),[41] and Au/ Ni(110).[42] Relief of the compressive energy is proposed as one of the driving forces for the dealloying process. In the Au/Ni(110) system,[42] Au atoms initially alloy into the Ni(110) surface at low coverage but dealloy into a vacancy-stabilized Au dimer-trimer chain structure at Au coverages larger than 0.4 ML. Based on total-energy calculations it was shown that the surface compressive stress induced by the substituted Au drives the surface alloy to dealloy above a critical coverage. Similarly, in the present Ag-Bi system, the tensile stress of the clean Ag surface is originally relieved by the incorporation of large-sized Bi atoms into the Ag lattice. However, above a critical coverage, further incorporation of Bi turns the tensile stress into compressive stress. Hence, as the Bi coverage increases above the critical limit, a dealloying process is favored.

We suggest a possible mechanism for the dealloying process and formation of the $(p \times \sqrt{3})$ overlayer based on the following steps. First, starting at the step edges, the deposited Bi atoms replace the Ag atoms in the $(\sqrt{3} \times \sqrt{3})R30°$ islands on Ag(111) to form the $(p \times \sqrt{3})$ overlayer. Second, the displaced Ag atoms diffuse onto the substrate terraces and displace Bi atoms from the substitutional sites, thereby recovering the original pure Ag(111) surface. The displaced Bi atoms can add to the $(p \times \sqrt{3})$ island, playing a role similar to that of the deposited Bi atoms. We did not observe any $(p \times \sqrt{3})$ structures embedded into the terraces during STM scanning. Thus the possibility that deposited Bi atoms can replace Ag atoms in the substitutional alloy to form an embedded Bi layer can be ruled out. As a result of these processes a chemically abrupt interface can be recovered by the dealloying process.

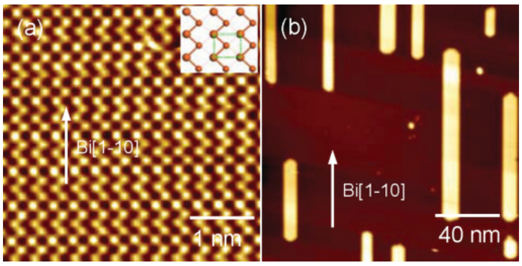

FIG. 5. (Color online) (a) Atomic resolution STM image of 1 ML Bi deposited on Ag(111), showing the formation of a Bi monolayer with the Bi(110) plane. The inset shows the atomic configuration of the Bi(110) plane. (b) STM image of 1.5 ML Bi deposition on Ag(111), showing the elongated growth along the Bi$[1\bar{1}0]$ direction.

C. Bi(110) overlayers

The Bi $(p \times \sqrt{3})$ overlayer phase shows a further structural transition with increasing coverage. As shown in Fig. 5(a), after deposition of 1 ML of Bi, the lattice constants decrease compared to those discussed in Sec. III B and a rectangular unit cell with $\mathbf{a}_2 = 4.74$ Å and $\mathbf{b}_2 = 4.54$ Å can be identified in the image. The atomic density has increased to a value of 9.3×10^{14} cm^{-2}. The surface unit cell contains two atoms, and the central atom in the cell is offset to the short edge of the unit cell to give a structure containing zigzag chains. The compressed overlayer structure is basically that found on the (110) surface of elemental Bi. Based on STM and LEED observations, the epitaxial relationship between Bi(110) and Ag(111) is determined to be Bi$[1\bar{1}0] \parallel$ Ag$[1\bar{1}0]$ and Bi$[001] \parallel$ Ag$[11\bar{2}]$ with $7|\mathbf{a}_{\mathrm{Bi}[1\bar{1}0]}| = 11|\mathbf{a}_{\mathrm{Ag}[1\bar{1}0]}|$ and $20|\mathbf{a}_{\mathrm{Bi}[001]}| = 19|\mathbf{a}_{\mathrm{Ag}[11\bar{2}]}|$.[43] This is similar to the adsorption structure of Bi(110) thin films electrodeposited on Au(111).[44] In a simple model, the phase transition from the $(p \times \sqrt{3})$ structure to Bi(110) is determined by two competing interactions, namely, Ag-Bi substrate-overlayer interactions and Bi-Bi overlayer-overlayer interactions. In the loosely packed $(p \times \sqrt{3})$ overlayer, the Ag-Bi interaction dominates over the Bi-Bi interaction. This statement is corroborated by the fact that the $(p \times \sqrt{3})$ is locked pseudomorphically to the $[11\bar{2}]$ direction of the Ag substrate. The relatively strong Ag-Bi interaction causes the Bi atoms to adopt positions determined by the Ag substrate lattice. However, with increasing Bi coverage, Bi-Bi interactions become more important and gradually become the major determinant of surface structure. Thus Bi-Bi interaction drives Bi to adopt its own lattice structure, giving rise to an incommensurate Bi(110) monolayer.

Increasing the Bi coverage to beyond 1 ML promotes the growth of Bi ribbon bilayers elongated along the $[1\bar{1}0]$ direction, as shown in Fig. 5(b).[43] The preferential growth of Bi ribbons elongated along this direction results from the preferential attachment of Bi atoms to the ends of the ribbons. Bulk Bi has highly anisotropic bonding[19] and the surface structure of Bi(110) is characterized by zigzag covalently bonded atomic chains running along the $[1\bar{1}0]$ direction, with weaker bonds in the orthogonal direction [the inset in Fig. 5(a)]. Therefore, Bi adatoms on the surface preferentially attach to the ends of the ribbons, resulting in preferential growth along the Bi [1$\bar{1}$0] direction. Furthermore, the growth of Bi ribbons is quantized into double (110) layers units with a width of 6.6 Å, and the growth exhibits an even-number layer stability. This is consistent with recent observations of "magic" thicknesses in ultrathin Bi films on the Si(111) surface, where Bi(110) 2D islands with an even number of layers are dominant.[45] This stability is attributed to the energetically preferred pairing of two neighboring layers. On a bulk-terminated Bi(110) surface, 50% of surface atoms have *pz* dangling bonds. In a film with an even number of (110) layers, the dangling bonds are completely saturated by pairing with a neighboring layer. All the atoms are then threefold coordinated, leading to stabilization of the (110) surface. In contrast, films with an odd number of layers are not stable since the dangling bonds of the top layer are unable to be saturated by layer pairing.

IV. CONCLUDING REMARKS

In summary, we have investigated the coverage-dependent growth of Bi on Ag(111) and have identified a number of atomically ordered structures. The system exhibits an alloying and dealloying process that is typical for metal-on-metal systems where the individual components are not miscible as bulk phases. It is energetically favorable for the initially deposited Bi atoms to be incorporated into the topmost Ag(111) layer by exchanging with surface Ag atoms to form a dilute array of substitutional Bi atoms within the Ag matrix as well as an adlayer of the Ag_2Bi surface alloy. Since the incorporation of larger-sized Bi atoms presumably induces a compressive strain, a surface dealloying process ensues when the Bi coverage is reaches a critical value. Future stress measurements or kinetic Monte Carlo calculations are required to elucidate the mechanisms and driving force for the dealloying process. Nevertheless the Ag_2Bi alloy phase gradually converts into an ordered $(p \times \sqrt{3})$ overlayer structure with a rectangular lattice 2D surface cell with $\mathbf{a}_1 = 5.0$ Å, $\mathbf{b}_1 = 4.7$ Å supported on Ag(111). After the dealloying process is complete, Bi(110) thin films can be finally grown epitaxially on Ag(111) with a chemically abrupt interface. The "rumpling" of the surface alloy determined from experimental and *ab initio* calculations may provide additional information necessary to understand the giant spin splitting recently observed in the Bi/Ag(111) surface alloy system, which was believed to originate from a strong in-plane gradient of the crystal potential in the surface layer. This also provides a model system to envision the alloying process in other systems such as Pb on Ag(111), which exhibit a large Rashba effect. The ultrathin Bi films on Ag(111) may exhibit unusual properties originating from quantum confinement effects coupled with the unique properties of the Bi surface, opening up potential applications in spintronic devices.[19,25] As an elegant example, the quantum well state confinement by the ultrathin Bi film can induce a huge SO splitting. From a fundamental point of view, the results contribute further to the understanding of surface and interface phenomena in heteroepitaxial growth in materials.

ACKNOWLEDGMENT

The authors acknowledge support from Singapore ARF Grants No. R-143-000-392-133, No. R-143-000-406-112, and No. R-143-000-440-112, and from NUS YIA Grant No. R-143-000-452-101.

---

[*] hongliang.zhang@keble.ox.ac.uk

[†] phycw@nus.edu.sg

[1] M. Wuttig and X. Liu, *Ultrathin Metal Films*, Springer Tracts in Modern Physics Vol. 206 (Springer, New York, 2004).

[2] V. A. Shchukin and D. Bimberg, Rev. Mod. Phys. **71**, 1125 (1999).

[3] J. V. Barth, G. C. Costantini, and K. Kern, Nature (London) **437**, 671 (2005).

[4] L. Pleth Nielsen *et al.*, Phys. Rev. Lett. **71**, 754 (1993).

[5] H. Röder, E. Hahn, H. Brune, J. Bucher, and K. Kern, Nature (London) **366**, 141 (1993).

[6] H. L. Meyerheim, D. Sander, N. N. Negulyaev, V. S. Stepanyuk, R. Popescu, I. Popa, and J. Kirschner, Phys. Rev. Lett. **100**, 146101 (2008).

[7] J. A. Venables, G. D. T. Spiller, and M. Handbücken, Rep. Prog. Phys. **47**, 399 (1984).

[8] J. Tersoff, Phys. Rev. Lett. **74**, 434 (1995).

[9] J. Dalmas, H. Oughaddou, C. Leandri, J. M. Gay, G. Le Gay, G. Treglia, B. Aufray, O. Bunk, and R. L. Johnson, Phys. Rev. B **72**, 155424 (2005).

[10] H. Y. Xiao, X. T. Zu, X. He, and F. Gao, Chem. Phys. **325**, 519 (2006).

[11] S. A. de Vries, W. J. Huisman, P. Goedtkindt, M. J. Zwanenburg, S. L. Bennett, I. K. Robinson, and E. Vlieg, Surf. Sci. **414**, 159 (1998).

[12] P. D. Quinn, C. Bittencourt, and D. P. Woodruff, Phys. Rev. B **65**, 233404 (2002).

[13] G. Bihlmayer, S. Blügel, and E. V. Chulkov, Phys. Rev. B **75**, 195414 (2007).

[14] F. Besenbacher *et al.*, Science **279**, 1913 (1998).

[15] M. L. Plummer, J. van Ek, and D. Weller, *The Physics of Ultra-High-Density Magnetic Recording* (Springer, New York, 2001).

[16] V. R. Stamenkovic *et al.*, Nat. Mater. **6**, 241 (2007).

[17] C. R. Ast, J. Henk, A. Ernst, L. Moreschini, M. C. Falub, D. Pacilé, P. Bruno, K. Kern, and M. Grioni, Phys. Rev. Lett. **98**, 186807 (2007).

[18] L. Moreschini, A. Bendounan, H. Bentmann, M. Assig, K. Kern, F. Reinert, J. Henk, C. R. Ast, and M. Grioni, Phys. Rev. B **80**, 035438 (2009).

[19] Ph. Hofmann, Prog. Surf. Sci. **81**, 191 (2006).

[20] Y. Koroteev, G. Bihlmayer, J. E. Gayone, E. V. Chulkov, S. Blügel, P. M. Echenique, and Ph. Hofmann, Phys. Rev. Lett. **93**, 046403 (2004).

[21] T. Hirahara *et al.*, Phys. Rev. Lett. **97**, 146803 (2006).

[22] C. R. Ast *et al.*, Phys. Rev. B **75**, 201401(R) (2007).

[23] H. Mirhosseini *et al.*, Phys. Rev. B **79**, 245428 (2009).

[24] I. Gierz, B. Stadtmüller, J. Vuorinen, M. Lindroos, F. Meier, J. H. Dil, K. Kern, and C. R. Ast, Phys. Rev. B **81**, 245430 (2010).

[25] S. Mathias *et al.*, Phys. Rev. Lett. **104**, 066802 (2010).

[26] K. H. L. Zhang, H. Li, H. Y. Mao, H. Huang, J. Ma, Andrew T. S. Wee, and W. Chen, J. Phys. Chem. C **114**, 11234 (2010).

[27] G. Kresse and J. Hafner, J. Phys. Condens. Matter **6**, 8245 (1994).

[28] G. Kresse and J. Joubert, Phys. Rev. B **59**, 1758 (1999).

[29] P. E. Blöchl, Phys. Rev. B **50**, 17953 (1994).

[30] J. P. Perdew and Y. Wang, Phys. Rev. B **45**, 13244 (1992).

[31] H. J. Monkhorst and J. D. Pack, Phys. Rev. B **13**, 5188 (1976).

[32] P. T. Sprunger, E. Lægsgaard, and F. Besenbacher, Phys. Rev. B **54**, 8163 (1996).

[33] T. Nakagawa, S. Mitsushima, H. Okuyama, M. Nishijima, and T. Aruga, Phys. Rev. B **66**, 085402 (2002).

[34] M. M. J. Bischoff, T. Yamada, A. J. Quinn, R. G. P. van der Kraan, and H. van Kempen, Phys. Rev. Lett. **87**, 246102 (2001).

[35] R. C. Cammarata, Prog. Surf. Sci. **71**, 1 (1994).

[36] L. Vitos, A.V. Ruban, H. L. Skriver, and J. Kollár, Surf. Sci. **411**, 186 (1998).

[37] V. S. Stepanyuk and W. Hergert, Phys. Rev. B **62**, 7542 (2000).

[38] I. M. McLeod, V. R. Dhanak, A. Matilainen, M. Lahti, K. Pussi, and K. H. L. Zhang, Surf. Sci. **604**, 1395 (2010).

[39] C. Chen, K. D. Kepler, A. A. Gewirth, B. M. Ocko, and J. Wang, J. Phys. Chem. **97**, 7290 (1993).

[40] C. Nagl, O. Haller, E. Platzgummer, M. Schmid, and P. Varga, Surf. Sci. **321**, 237 (1994).

[41] W. Pan, R. Popescu, H. L. Meyerheim, D. Sander, O. Robach, S. Ferrer, M.-T. Lin, and J. Kirschner, Phys. Rev. B **71**, 174439 (2005).

[42] L. Pleth Nielsen, F. Besenbacher, I. Stensgaard, E. Lægsgaard, C. Engdahl, P. Stoltze, and J. K. Nørskov, Phys. Rev. Lett. **74**, 1159 (1995).

[43] H. L. Zhang,W. Chen, X. S. Wang, J. Yuhara, and A. T. S. Wee, Appl. Surf. Sci. **256**, 460 (2009).

[44] C. A. Jeffrey, S. H. Zheng, E. Bohannan, D. A. Harrington, and S. Morin, Surf. Sci. **600**, 95 (2006).

[45] T. Nagao, J. T. Sadowski, M. Saito, S. Yaginuma, Y. Fujikawa, T. Kogure, T. Ohno, Y. Hasegawa, S. Hasegawa, and T. Sakurai, Phys. Rev. Lett. **93**, 105501 (2004).

Publication VI

I.M. McLeod, V.R Dhanak, A. Matilainen, M. Lahti, K. Pussi, K.H.L. Zhang
"LEED I-V and DFT Structure determination of p($\sqrt{3} \times \sqrt{3}$)R30° Pb-Ag(111)
surface alloy" Reprinted from Submitted to Journal of Physics: Condensed Matter.
23, 265006 ©(2011) IOP Science
http://dx.doi.org/10.1088/0953-8984/23/26/265006

IOP PUBLISHING JOURNAL OF PHYSICS: CONDENSED MATTER

J. Phys.: Condens. Matter **23** (2011) 265006 (6pp) doi:10.1088/0953-8984/23/26/265006

LEED I–V and DFT structure determination of the $(\sqrt{3} \times \sqrt{3})$R30° Pb–Ag(111) surface alloy

I M McLeod[1], V R Dhanak[1,4], M Lahti[2], A Matilainen[2], K Pussi[2] and K H L Zhang[3]

[1] Department of Physics, The University of Liverpool, Liverpool L69 3BX, UK
[2] Department of Mathematics and Physics, Lappeenranta University of Technology, PO Box 20, 53851 Lappeenranta, Finland
[3] Department of Chemistry, Chemistry Research Laboratory, Mansfield Road, Oxford OX1 3TA, UK

E-mail: vin@liverpool.ac.uk (V R Dhanak)

Received 18 March 2011, in final form 13 May 2011
Published 13 June 2011
Online at stacks.iop.org/JPhysCM/23/265006

Abstract

The deposition of 1/3 of a monolayer of Pb on Ag(111) leads to the formation of $PbAg_2$ surface alloy with a long range ordered $(\sqrt{3} \times \sqrt{3})$R30° superstructure. A detailed analysis of this structure using low-energy electron diffraction (LEED) I–V measurements together with density functional theory (DFT) calculations is presented. We find strong correlation between experimental and calculated LEED I–V data, with the fit between the two data sets having a Pendry's reliability factor of 0.21. The Pb atom is found to replace one top layer Ag atom in each unit cell, forming a substitutional $PbAg_2$ surface alloy, as expected, with the Pb atoms residing approximately 0.4 Å above the Ag atoms due to their size difference. DFT calculations are in good agreement with the LEED results.

1. Introduction

The formation of a surface alloy when a metal is deposited on a metal substrate is by no means an unusual phenomenon. In fact, even where the two metals in question are immiscible in the bulk, the formation of a surface alloy is not uncommon, giving rise to both interesting and useful properties, particularly in the case of post-transition metals such as Pb, Sb and Bi [1–5, 24, 6, 7]. These properties include potential applications in catalysis, corrosion resistance, surface hardening or for their electronic properties which can lead to novel effects such as spin splitting. As such, they have received considerable interest in recent years and continue to do so. Pb thin film growth is also of interest for use as a surfactant to promote 2D layer by layer growth as has been reported in numerous recent studies [8–11]. Furthermore, as an adsorbate at higher coverage, the growth of Pb films can lead to the formation of nano-sized structures due to quantum confinement and finite size effects which in turn can lead to some novel effects [12–14].

The deposition of Pb on Ag(111) gives rise to a $(\sqrt{3} \times \sqrt{3})$R30° surface alloy at approximately 1/3 monolayer (ML) coverage, then, after some critical coverage, a de-alloying process occurs. Here we focus our attention on the $(\sqrt{3} \times \sqrt{3})$R30° structure. This $(\sqrt{3} \times \sqrt{3})$R30° structure is seen in other systems on fcc(111) substrates [15–21] and in fact Ast *et al* [22] recently identified these surface alloys between heavy metals and noble metals as a new class of materials having long range order and exhibiting large spin splitting of their surface states. The main factors leading to their formation are the relative surface energies of the pure elements, their relative atomic sizes and the interactions between adsorbate–adsorbate and adsorbate–substrate atoms [23]. The alloys are formed by a direct substitution of every third atom in the surface layer by an adsorbate atom, meaning that the unit cell of the surface layer contains three atoms instead of one, as was previously the case. In instances where the adsorbate atoms are significantly larger than those of the substrate, a 'rumpling' of the surface layer is seen with the adsorbate atoms slightly raised above those of the substrate due to their size mismatch. It is worth noting that this rumpling is often less than that predicted using a hard-spheres

---

[4] Author to whom any correspondence should be addressed.

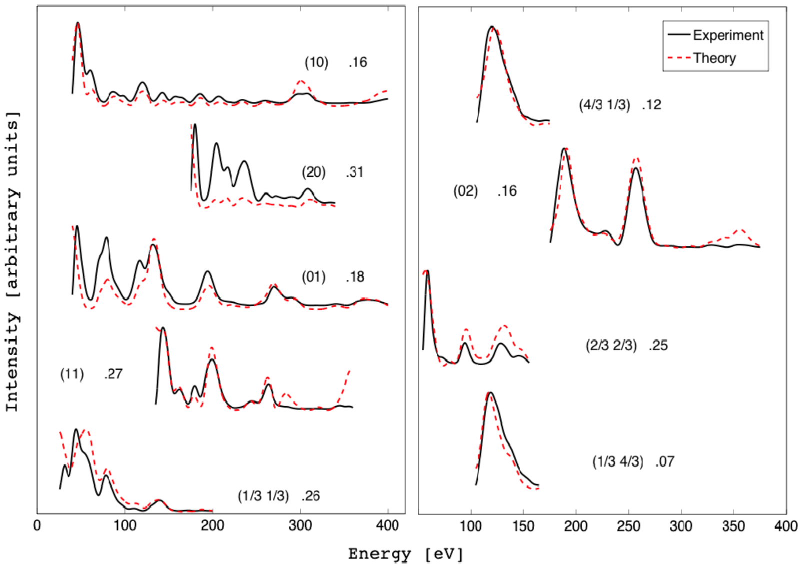

Figure 1. I–V curves for the best fit structure compared with experimental data. Individual beam R-factors are shown. (This figure is in colour only in the electronic version)

model based on atomic radii. In some systems, such as the ($\sqrt{3} \times \sqrt{3}$)R30° Sb–Cu(111) and Sb–Ag(111) [24], a stacking fault is also induced by the alloy formation. This so-called stacking fault is where the whole top layer of atoms moves from the fcc hollow sites to the hcp hollows. It is not clear why a stacking fault is manifested in some of these systems but possibly there is a role played by subsurface species of adatoms [24].

The case of Pb/Ag(111) has, in fact, been the subject of recent studies from both a structural and an electronic point of view [25, 26]. Interestingly, Dalmas *et al* [27] reported a rumpling not only between the Pb and Ag atoms in the surface layer but also between the two Ag atoms in the unit cell of this surface layer, as seen with scanning tunneling microscopy (STM). They speculated that this phenomenon was induced by a Peierls type distortion although such an effect has not been seen in any similar systems. Given the interest in these materials for properties such as the Rashba effect and the fact that Rashba energies can be tuned with small changes in surface composition and structure [28, 29], as well as the unusual nature of the rumpling, we have carried out this further structural study on the system.

In this paper we present a detailed atomic structural analysis of the ($\sqrt{3} \times \sqrt{3}$)R30° Pb–Ag(111) structure using a combined low-energy electron diffraction (LEED) I–V and density functional theory (DFT) analysis. The results show that a Pb atom is found to replace one top layer Ag atom in each unit cell, forming a substitutional unfaulted PbAg$_2$ surface alloy, with the larger Pb atoms residing about 0.4 Å above the Ag atoms due to the size difference. The results also indicate that the Dalmas model with surface Ag rumpling is slightly less favourable than the model where the Ag atoms remain in their normal positions relative to one another.

2. Experiment

The experiments were conducted in a standard ultra-high vacuum (UHV) surface science chamber consisting of a PSP vacuum technology electron energy analyser, a dual anode x-ray source, rear view LEED optics from OCI Vacuum Microengineering and an Omicron STM-1. The base pressure of the system was less than 2×10^{-10} mbar, with hydrogen as the main residual gas in the chamber. The Ag(111) surface was prepared by cycles of Ar ion bombardment and annealing to approximately 750 K. The sample was considered clean when the LEED pattern showed sharp integer order spots and x-ray photoelectron spectroscopy (XPS) did not show any traces of contamination.

Pb was deposited onto the clean Ag(111) surface from a well degassed Omicron K-cell. During deposition the Ag sample was kept at room temperature and the vacuum pressure did not exceed 3×10^{-10} mbar. The Pb was deposited at a constant rate of 0.1 ML min^{-1}.

The intensity of the diffraction spots as a function of the energy of the incident electrons (LEED I–V spectra) was measured at normal incidence of the primary beam with the sample cooled to around 150 K. The spectra were background subtracted and normalized with respect to the primary beam current. The intensities of the symmetrically equivalent spots were averaged in order to reduce experimental noise.

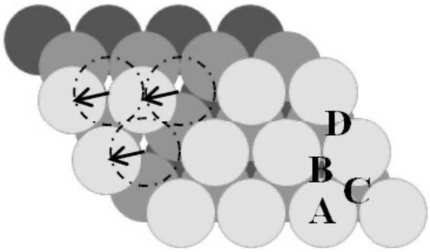

Figure 2. Adsorption sites: A = top, B = hcp hollow, C = fcc hollow and D = bridge. The top three layers of the substrate are shown. The arrows show atoms shifted into the hcp stacking fault position.

Table 1. Pendry R-factors from LEED analysis and adsorption energies from DFT calculations, for different adsorption geometries. A positive adsorption energy indicates that the adsorption is unfavourable, whilst a negative value indicates that adsorption is likely, with the lowest value being the most stable. Letters in parentheses refer to the Pb atom adsorption sites shown in figure 1.

Adsorption site	R-factor (first stage)	R-factor (final)	Adsorption energy (eV)
Top (A)	0.55		0.335
Hollow (B)	0.58		0.092
Hollow (C)	0.54		0.215
Bridge (D)	0.46		0.140
Faulted surface alloy	0.57		−0.275
Surface alloy	0.25	0.21	−0.290
Pendry variance	0.04		

3. Results and discussion

The data set utilized consisted of nine beams (five integer and four fractional order beams) ranging from 30 to 400 eV and recorded at 150 K (figure 1). The cumulative energy range was 1738 eV. The dynamical LEED calculations were carried out using the Barbieri/Van Hove SATLEED package [30]. The relativistic phase shifts were calculated using the phase shift program [31] that was packaged with SATLEED. Pendry's reliability factor, R_p, was used to quantify the agreement between experimental and calculated data and the error bars quoted were calculated using the Pendry RR-function [32]. Three different sets of phase shifts were used, one for lead, one for top layer Ag atoms and one for the Ag atoms in deeper layers. At the beginning of the analysis the Debye temperatures were set to 105 K and 225 K for lead and silver respectively, the l_{max} value was set to 11 and the imaginary part of the inner potential was set to −5 eV. The parameter l_{max} is the highest value used in the calculation and correlates to the accuracy in the muffin-tin potential. These values were optimized at the final stage of the analysis. The real part of the inner potential is independent of energy and was allowed to relax, as is the normal procedure in LEED analysis. All the parameters considered at each stage were optimized simultaneously.

Six different structural models were considered in the LEED calculations. These included four high symmetry adsorption geometries, namely the top (A) and hollows (B and C, for fcc and hcp hollows, respectively), as well as the bridge site (D), as shown in figure 2. Adsorption at the bridge site (D) lowers the symmetry of the surface, which means that proper domain averaging has to be taken into account in the LEED analysis. As well as these adsorption sites, two high symmetry substitutional alloy structures were also considered. The first of these was formed by placing one Pb atom per unit cell in a substitutional position over an essentially unperturbed Ag(111) surface layer to give the $(\sqrt{3} \times \sqrt{3})$R30° superstructure. The second was a similar surface alloy but with all the surface atoms displaced to the 'hcp' hollow sites, the so-called faulted surface alloy structure [5, 24, 7]. In figure 2, the hcp hollow site is indicated by 'C'.

At the first stage of the analysis the substrate atom positions were kept fixed and the only parameters varied were the perpendicular distance between the lead and substrate atoms, and the real part of the inner potential. In the second stage of the analysis the lead atom and the top five layers of the substrate were allowed to relax. In the third stage of the analysis the non-structural parameters (Debye temperatures, l_{max} and imaginary part of the inner potential) were optimized. Finally, in order to test the Dalmas model, the Ag atoms in the unit cell of the surface layer were allowed to move independently of one another.

The Pendry R-factors from different stages of analysis are listed in table 1. After each stage, structures that had a Pendry R-factor less than the sum of the minimum R-factor and the Pendry variance were selected to be optimized further. The substitutional surface alloy model was clearly most favourable after the first stage, consistent with the structure suggested by previous studies [25, 26], rendering it unnecessary to further optimize the other structures. Once the favoured structure was optimized the Ag atoms in the unit cell of the surface layer were allowed to move independently of one another. Since the model with surface Ag rumpling is lower symmetry there are more free parameters and hence one would expect to see a lower R-factor. In fact, allowing the Ag atoms to move independently, the program gave a 0.06 Å rumpling between the Ag atoms as the optimum structure. However, the R-factor for this structure was the same as for the unrumpled structure (0.21). Based on the LEED I–V one cannot really categorically say whether the Dalmas model is real or not. One thing that must be remembered is that if the Dalmas model were real, it would require domain averaging (the LEED pattern should be a combination of two domains related by a mirror plane). Structural and non-structural parameters for the unrumpled, alloyed structure are listed in table 2 together with the results from our DFT analysis (see table 2).

Top and side views of the structure are shown in figure 3 along with a LEED image of the structure. The corresponding best fit I–V curves are shown in figure 1. The final R-factor reached was 0.21. It is also noted that the optimized structure incorporates a slight buckling of the fourth layer of the silver substrate. The overall structure remains bulk like with a small contraction of the top layers.

First-principles DFT calculations were performed for the lead on Ag(111) system to verify and analyse the experimental

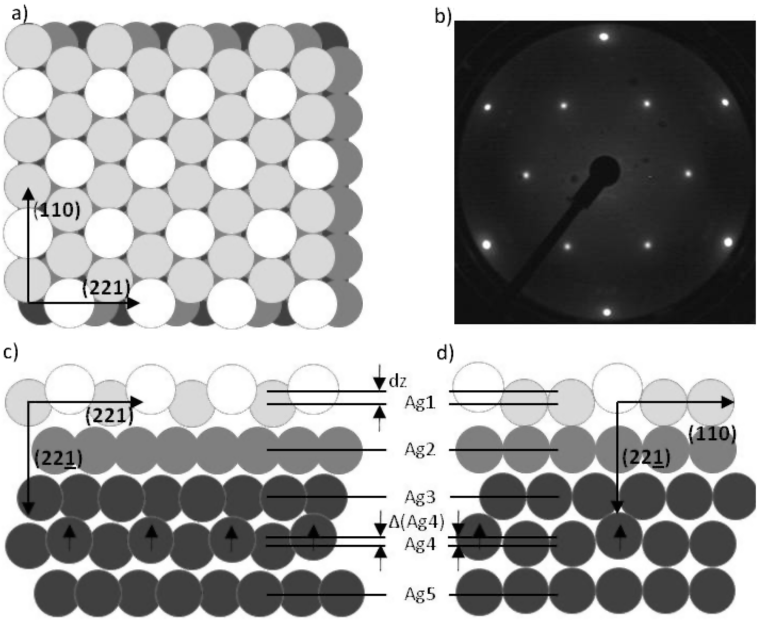

Figure 3. (a) Top view of the favoured structure. The top three layers of the slab are shown. (b) Corresponding LEED image taken at 46 eV. The outer spots are the (1, 0) and (0, 1) substrate spots and the inner spots are the (1/3, 1/3) adsorbate spots. ((c), (d)) Side views showing the top five layers. The arrows show the buckling in the fourth substrate layer as the Ag atoms directly below the Pb are displaced vertically upwards. The large white circles represent the Pb atoms that substitute Ag atoms in the top layer.

Table 2. Structural and non-structural parameters from LEED and DFT analysis. d(Pb–Ag) is the bond length between the Pb and Ag atoms in the first layer, dz(Ag–Pb) is the vertical distance between the first layer Ag atoms and the Pb atoms (the Pb is above the Ag), $dz/dz_{\mathrm{bulk}}(\mathrm{Ag}i - \mathrm{Ag}j)$ is the change in the vertical distance between the centres of mass of Ag layers i and j (negative means contraction). Δ(Ag4) is the buckling in the fourth substrate layer where the Ag atoms directly below the Pb atoms are pulled up slightly. Using a bulk interlayer spacing for clean Ag(111) of 2.35 Å, the LEED results show that the overall structure remains bulk like within the errors.

Parameter	LEED	DFT
d(Ag–Pb) (Å)	2.90 ± 0.06	3.01
dz(Ag–Pb) (Å)	0.42 ± 0.06	0.59
dz/dz_{bulk} (Ag1–Ag2) (%)	0 ± 1	-1
dz/dz_{bulk} (Ag2–Ag3) (%)	0 ± 1	0
dz/dz_{bulk} (Ag3–Ag4) (%)	-1 ± 2	0
dz/dz_{bulk} (Ag4–Ag5) (%)	-1 ± 3	0
Δ (Ag4) (Å)	0.02 ± 0.10	0.02
Debye T (Pb) (K)	85	
Debye T (Ag1) (K)	160	
Debye T (Ag bulk) (K)	225	
$V_{\mathrm{imaginary}}$ (eV)	-5	
l_{max}	11	
Ag bulk lattice constant (Å)	4.09	4.17

results presented in this paper. The static calculations for total energies were performed using the Vienna *ab initio* simulation package (VASP) [33–36] including the projector augmented wave (PAW) [37] potentials. A kinetic energy cut-off of 400 eV was applied for the plane waves, which was found to produce converged results for both Ag and Pb, for all the structures. For the exchange correlation potential the generalized gradient approximation (GGA) of Perdew and Wang (1991) (PW91) [38] was employed. The 10 × 8 × 1 Monkhorst–Pack mesh [39] was used for k-point sampling. In the DFT program, a quasi-Newton (or variable metric) algorithm is used to relax the ions into their instantaneous ground state. The forces and the stress tensor are used as search directions to find the equilibrium position. The Ag surface was modelled using the supercell approach, where periodic boundary conditions are applied to the central supercell so that it is reproduced periodically throughout xy-space. The surface slab was modelled with six layers of Ag atoms. A region of approximately 10 Å of vacuum was inserted in the z direction to prevent interactions from occurring between periodic images. The bottommost layer of the surface slab was frozen during the geometry relaxation.

The adsorption energies of the Pb atom are defined as

$$E_{\mathrm{ads}} = 1/N_{\mathrm{Pb}} \times (E_{\mathrm{tot}} - E_{\mathrm{clean}} - N_{\mathrm{Pb}} \times E_{\mathrm{Pb}}) \qquad (1)$$

where E_{tot} is the total energy of the relaxed Ag/Pb supercell, E_{clean} is the total energy of the relaxed clean Ag slab, N_{Pb} is the number of Pb atoms and E_{Pb} is the energy of one atom in the Pb bulk.

For substitutional alloy structures the adsorption energy is defined as

$$E_{\mathrm{ads}} = 1/N_{\mathrm{Pb}} \times (E_{\mathrm{tot}} - E_{\mathrm{clean}} - N_{\mathrm{Pb}} \times E_{\mathrm{Pb}} + N_{\mathrm{Pb}} \times E_{\mathrm{Ag-bulk}}) \quad (2)$$

where $E_{\mathrm{Ag-bulk}}$ is the total energy of an Ag bulk atom.

An Ag lattice constant of 4.17 Å was used, which was obtained from bulk cell optimization using the same computational parameters. The six structural models used in the LEED I–V analysis were considered in the DFT analysis. The adsorption energies for each site for the models that showed convergence in the calculations are listed in table 1. Of the overlayer geometries, the hcp hollow site is the most favourable but the substitutional and faulted surface alloy structures were by far the most stable with the unfaulted structure having an adsorption energy of −0.290 eV. The geometrical parameters for the relaxed substitutional surface alloy structure are listed in table 2 and compare well with the LEED data.

Like the LEED analysis, DFT also favours the unfaulted substitutional surface alloy (−0.290 eV) although faulted alloy structure where all the top surface atoms (Pb and Ag) have moved into hcp hollow sites is only marginally less favourable (−0.275 eV). One possible reason why our DFT calculations fail to clearly distinguish between the two structures is the use of the finite size of the slab (six layers). Indeed, in an earlier DFT calculation by Woodruff and Robinson [7] for the Sb–Ag(111) system, they found that the stacking fault energy was sensitive to the slab thickness and suggested that these calculations are only realistic using much larger scale parallel computing systems beyond our means. It is also worth noting that even for the clean Ag(111) surface, they found that there was a negligible difference in energy between the surface faulted and unfaulted structures. Our calculation for the clean Ag(111) shows that the energy difference between the faulted and unfaulted Ag surfaces is only 20 meV, similar to what has previously been reported [7]. This implies that on Ag(111), a stacking fault surface structure could easily be facilitated. In fact for Sb on Ag(111), both faulted and unfaulted $(\sqrt{3} \times \sqrt{3})\mathrm{R}30^\circ$ structures have been found, as well as evidence for subsurface stacking faults, attributed to some subtle influence of subsurface Sb. For the Pb on Ag(111) case, we have only found the unfaulted $(\sqrt{3} \times \sqrt{3})\mathrm{R}30^\circ$ structure, suggesting perhaps that Pb, with its larger atomic size compared to Sb, does not easily diffuse into the subsurface region. Another factor could be that there is a thermal activation barrier in moving all the surface atoms from the fcc hollow sites to the hcp hollow sites. In fact the Sb on Ag(111) structures were formed by dosing and annealing to elevated temperatures while in our case sharp $(\sqrt{3} \times \sqrt{3})\mathrm{R}30^\circ$ Pb on Ag(111) structure was readily formed by dosing at room temperature.

DFT was also used to test the rumpled model suggested by Dalmas *et al*. Table 3 shows the adsorption energies starting with no rumpling and increasing to a maximum value of 0.15 Å between the two Ag atoms in the surface unit cell as measured perpendicular to the surface. In fact the total change in adsorption energy over this range was only 0.015 eV, coincidently the same as for the faulted structure. Although the unrumpled model is favoured, given the previously stated limitations of this technique it cannot be absolutely stated which model is correct.

Table 3. Changes in adsorption energy resulting from a change in the height of the top layer Ag atoms as calculated by DFT.

Dz (Å)	Adsorption energy (eV)
0.00	−0.290
0.04	−0.273
0.07	−0.273
0.13	−0.277
0.15	−0.275

Both the LEED and DFT analysis show that in the stable substitutional surface alloy structure, there is a slight ‘rumpling’ of the surface due to the larger Pb atoms located about 0.4 Å above the surface plane of the Ag atoms. This amplitude of the ‘rumpling’ is smaller by about 1 Å than that predicted by a simple touching hard-spheres model based on bulk metallic radii (1.44 Å for Ag and 1.80 Å for Pb). This suggests a reduction in the effective radii similar to that found by Quinn *et al* [6] in their LEED study of the substitutional surface alloy structure for the Pb–Ni(111) system. It has been suggested that the reduction in the effective radii may be attributed to the influence of valence electron charge smoothing and associated surface stress effects [5, 24, 6, 13]. A similar effect is possibly the case for the Pb–Ag(111) structure in our study.

4. Conclusions

There is very good agreement between the geometrical parameters extracted from LEED I–V and DFT analyses. LEED analysis shows that the Pb atoms are found to replace one top layer Ag atom in each unit cell, forming a substitutional unfaulted surface alloy. DFT calculations show that the stable $(\sqrt{3} \times \sqrt{3})\mathrm{R}30^\circ$ structure is a surface alloy, but do not clearly distinguish between a faulted and unfaulted structure, possibly due to the limitation of using a finite size slab. Because of the size difference between the Ag and Pb atoms (Pb is approximately 25% larger than Ag), the top layer is corrugated such that the Pb atoms reside about 0.4 Å above the Ag atoms. The amplitude of this ‘rumpling’ is smaller than what would be predicted by a simple touching hard-spheres model. The interlayer spacings, calculated with respect to the centres of mass of the Ag atoms, remain bulk like in both the DFT and LEED analyses. Both LEED and DFT marginally favour the structure with no rumpling between the surface Ag atoms, although given the small size of any possible distortion and the limitations of the techniques the rumpled structure cannot be ruled out.

Acknowledgments

IMM wishes to thank EPSRC for their funding via a studentship. AM, ML and KP would like to thank the National Graduate School in Materials Physics and Academy of Finland for funding, and the CSC-IT Centre for Sciences Ltd for computational resources.

References

[1] Li D F, Xiao H Y, Zu X T and Dong H N 2007 *Physica* B **392** 217

[2] Nie J L, Xiao H Y, Zu X T and Gao F 2006 *Chem. Phys.* **326** 308

[3] Xiao H Y, Zu X T, He X and Gao F 2006 *Chem. Phys.* **325** 519

[4] Nascimento V B, Paniago R, de Siervo A, de Castilho C M C, Landers R, Soares E A and de Carvalho V E 2004 *Surf. Sci.* **572** 337

[5] Quinn P D, Brown D, Woodruff D P, Bailey P and Noakes T C Q 2002 *Surf. Sci.* **511** 43
Woodruff D P *et al* 2003 *Surf. Rev. Lett.* **10** 65

[6] Quinn P D, Bittencourt C and Woodruff D P 2002 *Phys. Rev.* B **65** 233404

[7] Woodruff D P and Robinson J 2000 *J. Phys.: Condens. Matter* **12** 7699

[8] Xu M C, Qian H J, Liu F Q, Ibrahim K, Lai W Y and Wu S C 2000 *Chin. Phys. Lett.* **17** 595

[9] Prieto J E, Rath Ch, Muller S, Hammer L, Heintz K and Miranda R 2000 *Phys. Rev.* B **62** 5144

[10] Gomez L and Ferron J 2001 *Phys. Rev.* B **64** 033409

[11] Farias D, Nino M A, de Miguel J J, Miranda R, Morse J and Bozzolo G 2003 *Appl. Surf. Sci.* **219** 80

[12] Ayuela A, Ogando E and Zabala N 2007 *Appl. Surf. Sci.* **254** 29

[13] Wei C M and Chou M Y 2002 *Phys. Rev.* B **66** 233408

[14] Ogando E, Zabala N, Chulkov E V and Puska M J 2005 *Phys. Rev.* B **71** 205401

[15] van Gastel R, Kaminski D, Vlieg E and Poelsema B 2009 *Surf. Sci.* **603** 3292

[16] De Vries S A, Huisman W J, Goedtkindt P, Zwanenburg M J, Bennett S L, Robinson I K and Vlieg E 1998 *Surf. Sci.* **414** 159

[17] McLeod I M, Dhanak V R, Matilainen A, Lahti M, Pussi K and Zhang K H L 2010 *Surf. Sci.* **604** 1395

[18] Brown D, Quinn P D, Woodruff D P, Bailey P and Noakes T C 2000 *Phys. Rev.* B **61** 7706

[19] Xu M C, Qian H J, Liu F Q, Ibrahim K, Lai W Y and Gao H J 2005 *Surf. Sci.* **589** 1

[20] Wider H, Gimple V, Evenson W, Schatz G, Jaworski J, Prokop J and Marszalek M 2003 *J. Phys.: Condens. Matter* **15** 1909

[21] Soares E A, Bittencourt C, Lopes E L, de Carvalho V E and Woodruff D P 2004 *Surf. Sci.* **550** 127

[22] Ast C R, Henk J, Ernst A, Moreschini L, Falub M C, Pacilé D, Bruno P, Kern K and Grioni M 2010 *Phys. Rev. Lett.* **104** 066802

[23] Dalmas J, Oughaddou H, Léandri C, Gay J-M, Le Lay G, Treglia G, Aufray B, Bunk O and Johnson R L 2006 *J. Phys. Chem. Solids* **67** 601

[24] Woodruff D P, Munoz-Marquez M A and Tanner R E 2003 *Curr. Appl. Phys.* **3** 19

[25] Pacile D, Ast C R, Papagno M, Da Silva C, Moreschini L, Falub M, Seitsonen A P and Grioni M 2006 *Phys. Rev.* B **73** 245429

[26] Dalmas J, Oughaddou H, Léandri C, Gay J-M, Le Lay G, Treglia G, Aufray B, Bunk O and Johnson R L 2005 *Phys. Rev.* B **72** 155424

[27] Dalmas J, Oughaddou H, Le Lay G, Aufray B, Treglia G, Girardeaux C, Bernardini J, Ujii J and Panaccione G 2006 *Surf. Sci.* **600** 1227

[28] Ast C R, Pacilé D, Moreschini L, Falub M C, Papagno M, Kern K and Grioni M 2008 *Phys. Rev.* B **77** 081407

[29] Meier F, Petrov V, Guerrero S, Mudry C, Patthey L, Osterwalder J and Hugo Dil J 2009 *Phys. Rev.* B **79** 241408

[30] Van Hove M A, Moritz W, Over H, Rous P J, Wander A, Barbieri A, Materer N, Starke U and Somorjai G A 1993 *Surf. Sci. Rep.* **19** 191

[31] Barbieri A and Van Hove M A 2007 private communication

[32] Pendry J B 1980 *J. Phys. C: Solid State Phys.* **13** 937

[33] Kresse G and Hafner J 1994 *J. Phys.: Condens. Matter* **6** 8245

[34] Kresse G and Furthmüller J 1996 *Comput. Mater. Sci.* **6** 15

[35] Kresse G and Furthmüller J 1996 *Phys. Rev.* B **54** 11169

[36] Kresse G and Joubert J 1999 *Phys. Rev.* B **59** 1758

[37] Blöchl P E 1994 *Phys. Rev.* B **50** 17953

[38] Perdew J P and Wang Y 1992 *Phys. Rev.* B **45** 13244

[39] Monkhorst H J and Pack J D 1976 *Phys. Rev.* B **13** 5188

Publication VII

M. Lahti, K. Pussi, E. McLoughlin, A.A. Cafolla “The structure of Cu{100}-p(2×6)-2mg-Sn studied by DFT and LEED“ Reprinted from Surface Science 605, 1000 ©(2011)with permission from Elsevier.

Surface Science 605 (2011) 1000–1004

Contents lists available at ScienceDirect

Surface Science

journal homepage: www.elsevier.com/locate/susc

The structure of Cu{100}-p(2 × 6)-2mg-Sn studied by DFT and LEED

M. Lahti [a], K. Pussi [a,*], E. McLoughlin [b,c], A.A. Cafolla [b,c]

[a] Department of Mathematics and Physics, Lappeenranta University of Technology, PO Box 20, FIN-53851 Lappeenranta, Finland
[b] School of Physical Sciences, Dublin City University, Glasnevin, Dublin 9, Ireland
[c] National Centre for Sensor Research (NCSR), Dublin City University, Glasnevin, Dublin 9, Ireland

ARTICLE INFO

Article history:
Accepted 25 February 2011
Available online 5 March 2011

Keywords:
DFT
LEED
Copper
Tin
Adsorption
Surface structure

ABSTRACT

Low Energy Electron Diffraction (LEED) and Density Functional Theory (DFT) have been used to analyse the structure of Cu{100}-p(2 × 6)-2mg-Sn at room temperature. In this work we found that the favoured geometry for this 0.33 ML Cu{100}-Sn phase is a combination of an overlayer structure and a surface alloy; two Sn atoms are alloyed in to the first copper layer and the other two Sn atoms adsorb at off symmetry hollow sites. In order to relieve the stress in the alloyed layer, the alloyed Sn atoms are buckled 0.59/0.45 ± 0.2 Å (DFT/LEED) above the centre of mass of the first layer copper atoms.

1. Introduction

Intermixing, alloying, dealloying and strain-induced reconstructing at surfaces are important phenomena in the growth of thin films on metal surfaces and for these reason metal-on-metal epitaxial growth has been studied intensively for many years. The interfacial effects arising in these systems may have a significant influence on the electronic, catalytic and magnetic properties of the resulting thin films. The most commonly studied structures are bimetallic systems either in the form of bulk or surface alloys. In particular, the interaction of alkali and transition metals with the Cu{100} surface has been extensively studied both experimentally and theoretically. Interest in these systems has been motivated by the fact that Cu-based bimetallic catalysts show very useful properties in comparison to their single-metal counterparts and play an important role in many branches of industry including microelectronics electrochemistry and catalysis [1,2]. Within these systems tin adsorption on the Cu{100} surface has been extensively studied [3–14]. Below a monolayer coverage, at room temperature, there are five ordered phases of the Cu{100}-Sn system; p(2 × 2) at 0.2 ML, p(2 × 6)-2mg at 0.33 ML, c(4 × 8) at 0.375 ML, $p(3\sqrt{2}\times\sqrt{2})R45^\circ$ at 0.5 ML and c(4 × 4) at 0.65 ML [14]. The 0.5 ML phase has been studied extensively, including both LEED I(E) and DFT [6,13]. The 0.65 ML phase has been recently studied with LEED I(E) [14]. In this paper we present the results of LEED intensity analysis and DFT calculations of 0.33 ML Cu{100}-p(2 × 6)-2mg-Sn system. The model structures proposed previously by STM [10] do not give satisfactory agreement, thus we propose two additional models which are favoured by both LEED I(E) and DFT.

2. Experiments

The LEED I(E) measurements were performed in an ultrahigh vacuum chamber operated at a base pressure of 1×10^{-10} mbar. The system was equipped with a 4-grid reverse view LEED optics (VG Microtech). The Cu{100} crystal of dimensions $10\times10\times1.5$ mm^3 (Metal Crystals and Oxides, Ltd.) was polished mechanically to a mirror finish. The crystal was supported by four 0.25 mm Ta support wires through which current was passed to heat the sample. The sample temperature was monitored with a chromel–alumel thermocouple embedded in a 0.25 mm diameter spark eroded hole through the top edge of the crystal. The crystal was cleaned in situ by repeated cycles of argon ion bombardment at 1 kV for 20 min followed by annealing at 800 K for 20 min. The clean crystal showed a sharp, well contrasted, p(1 × 1) LEED pattern with I(E) spectra in excellent agreement with those reported in the literature [15]. Deposition of tin on the Cu{100} surface was carried out at room temperature using a water cooled Knudsen cell evaporator (WA Technology) which provided a constant tin flux of approximately 0.015 ML·min^{-1} with the base pressure in the chamber remaining below 3×10^{-10} mbar during Sn deposition.

The LEED patterns showed five ordered phases in excellent agreement with those reported previously [3,8–11,16,17], in terms of the symmetries and periodicities observed. Coverage assignments were made by monitoring LEED spot profiles as a function of Sn deposition times. This analysis concluded that the five ordered phases reached optimal perfection at Sn coverages of 0.21, 0.33, 0.375, 0.50 and 0.70 ML respectively, on the assumptions that (i) the coverage at

---

[*] Corresponding author. Tel.: +358 5 621 2855; fax: +358 5 621 2898.
E-mail address: kathariina.pussi@lut.fi (K. Pussi).

0039-6028/$ – see front matter © 2011 Elsevier B.V. All rights reserved.
doi:10.1016/j.susc.2011.02.021

which the $p(3\sqrt{2}\times\sqrt{2})R45°$ phase reaches maximum perfection is 0.50 ML and (ii) that the sticking probability for the Sn is independent of the coverage. The transition from the p(2×6) to the c(4×8) phase occurs over a relatively narrow coverage range. Previous STM and He atom scattering studies show that p(2×6) structure coexists with the c(4×8) phase at a Sn coverage in excess of 0.35 ML [9,10]. This makes it difficult to achieve a perfect p(2×6) structure. To address this issue the p(2×6) structure was optimized by monitoring the intensity and width of the fractional order spots as a function of Sn coverage.

The LEED I(E) data were acquired using a CCD camera and the Spectaview data acquisition software which allowed automatic tracking of a user defined number of beams. I(E) spectra were recorded for the p(2×6) phase obtained at a Sn coverage of 0.33 ML where contribution from the c(4×8) diffraction spots is minimised. The I(E) data were recorded individually from sets of symmetrically equivalent beams to ensure reliable spot tracking. Normal incidence was attained by collection of I(E) spectra from the (10), (01), (−10) and (0–1) beams and variation of the sample angular alignment until the four beams exhibited visually identical I(E) spectra in the energy range 50–400 eV Two I(E) data sets were recorded, at room temperature, from independently prepared Cu{100}-(2×6)-2mg-Sn structures. Prior to analysis the I(E) spectra were individually background subtracted by empirical fitting a monotonically rising function to user defined minima in the spectra. Symmetrically equivalent beams were then averaged to improve the signal-to-noise ratio. The averaged beams were normalized to constant incoming primary beam current and smoothed via a 5-point adjacent averaging routine.

3. Calculations

The Cu{100}-p(2×6)-2mg-Sn unit cell has 12 clean substrate copper atoms. The tin coverage of this system is 0.33 ML, which means four tin atoms per unit cell. The LEED pattern has absence of intensity at the ((2 n + 1) / 6,0) positions which implies *p2mg* symmetry for the system. The model structures tested included the three models proposed by J. Lallo et al. [10] and two additional models. Model (a) is an overlayer model where the Sn atoms sit at bridge sites. Model (b) utilises the same bridge adsorption site, but four copper adatoms are added to the top layer. Model (c) is a surface alloy model, where the Sn atoms are only slightly displaced from the fourfold hollow sites and with vacancies in the second layer. The fourth model, model (d) is a combination of surface alloy and overlayer structure; two Sn atoms are alloyed into the first copper layer and two Sn atoms are sitting slightly off the fourfold hollow sites. Model (e) is the same as the model (d) with four additional copper atoms in the top layer. These five model structures are shown in Fig. 1.

3.1. DFT

The static calculations for total energies were performed using the Vienna ab-initio simulation package (VASP) [18–21] including the projector augmented wave (PAW) [22] potentials. A kinetic energy cut-off of 400 eV was applied for the plane waves. For the exchange correlation potential the Perdew–Wang 91 (PW91) generalized gradient approximation (GGA) [23] was employed. The 8 × 4 × 1 Monkhorst–Pack

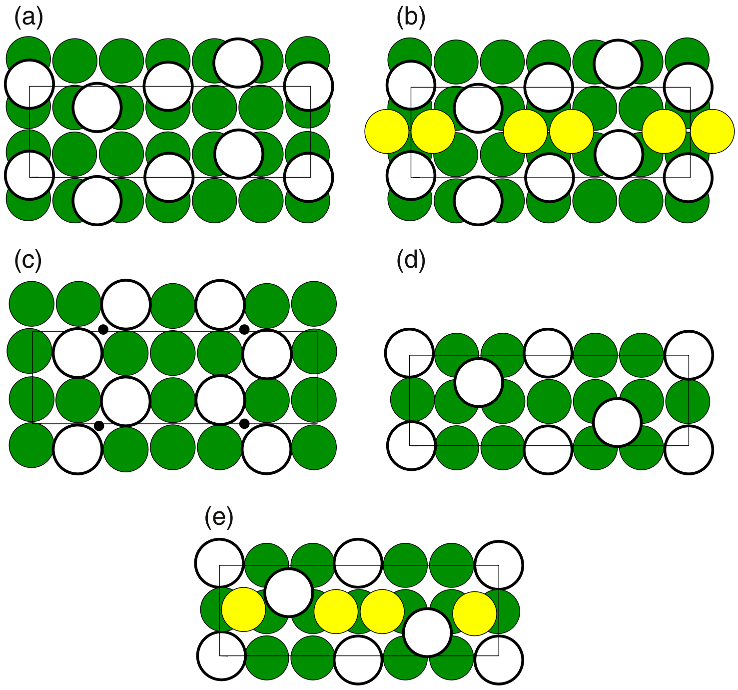

Fig. 1. Top views of the models used in the analysis. The models (a)–(c) correspond to the models in Fig. 3 in the paper by Lallo et al. [10] and the models (d) and (e) are the models proposed by the authors of this paper. White atoms are Sn, green (grey) atoms are the first layer Cu, yellow (light grey) atoms are Cu adatoms (model b and e) and black dots are missing second layer Cu atoms (model c). The p(2×6) unit cell is shown with black line.

Table 1
Adsorption energies for the models shown in Fig. 1. The model (e) was found to be unstable by DFT, thus no adsorption energy is reported for this model.

Model	Adsorption energy [eV]
(a)	−0.077
(b)	−0.401
(c)	−0.349
(d)	−0.588
(e)	–

mesh [24] was used for k-point sampling. The Cu surface was modelled using the supercell approach, where periodic boundary conditions are applied to the central supercell so that it is reproduced periodically throughout xy-space. The surface slab was modelled with 6 layers of Cu atoms. A region of approximately 18 Å of vacuum was inserted in the z-direction to prevent interactions occurring between mirror images. The bottommost layer of the surface slab was frozen during the geometry relaxation. Adsorption energies of the Sn atom are defined:

$$E_{ads} = \frac{1}{N_{Sn}} \times (E_{tot} - E_{clean} - N_{Sn} \times E_{Sn} + N_{CuA} \times E_{Cu-bulk}) \quad (1)$$

where

$$N_{CuA} = N_{Cuc} - N_{CuSn} \quad (2)$$

Where E_{tot} is the total energy of the relaxed Cu/Sn supercell, E_{clean} is the total energy of the relaxed clean Cu slab, N_{Sn} is the number of Sn atoms and E_{Sn} is the energy of the one atom in the Sn bulk. N_{Cuc} is the number of Cu atoms in the clean supercell and N_{CuSn} is the number of Cu atoms in the Cu/Sn supercell. $E_{Cu-bulk}$ is the total energy of Cu bulk atom. The adsorption energies for each model are listed in Table 1. Model (e) was found to be unstable. The copper adatoms that were initially placed at bridge sites (see Fig. 3) moved away from the glide plane, towards the hollow sites between the nearest neighbour Sn atoms, in order to maximise the distance between these copper adatoms. The adsorption energy for the resulting structure (−0.180 eV) was about 0.4 eV higher than the adsorption energy for model (d), which makes it unfavourable.

3.2. LEED I(E) analysis

The data set utilised consisted of nine beams (three integer and six fractional order beams), ranging from 40 eV to 500 eV, recorded at 300 K. The cumulative energy range is 2100 eV. The dynamical LEED calculations were performed using the Tensor-LEED program [25]. The relativistic phase shifts were calculated using the phase shift program [26] that is packaged with Tensor-LEED. The agreement between the theory and the experiment was tested using the Pendry R-factor and the error bars quoted are calculated using the Pendry RR-function [27]. Four different sets of phase shifts were used; two for tin (overlayer and alloyed), one for top layer Cu atoms and one for the Cu atoms in deeper layers. At the beginning of the analysis the Debye temperatures were set to 200 K and 345 K for tin and copper respectively, l_{max} value was set to 8 and imaginary part of inner potential was set to −5 eV. These values were optimised at the final stage of the analysis. The real part of the inner potential is independent of energy and it is allowed to relax as is the normal procedure in the LEED analysis.

At the first stage of the analysis only the Sn atoms and first layer Cu atoms were allowed to relax. The Pendry R-factors and the Pendry variance after the first stage showed that only the model (d) should be considered for further refinement (see Table 2). Model (d) was analysed in more detail, which included refining the geometrical structure down to the sixth copper layer and optimising the nonstructural parameters (Debye temperature, imaginary part of inner potential and l_{max}). A moderate value of 0.28 for the Pendry R-factor is achieved. The final structural and non-structural parameters are listed in Table 3 along with the parameters extracted from the DFT analysis. The I(E) curves for the best fit geometry are shown in Fig. 2.

4. Results and discussion

Since the Sn atoms are 9% larger than the Cu atoms the alloyed layer includes large buckling in order to relieve the stress. The alloyed Sn

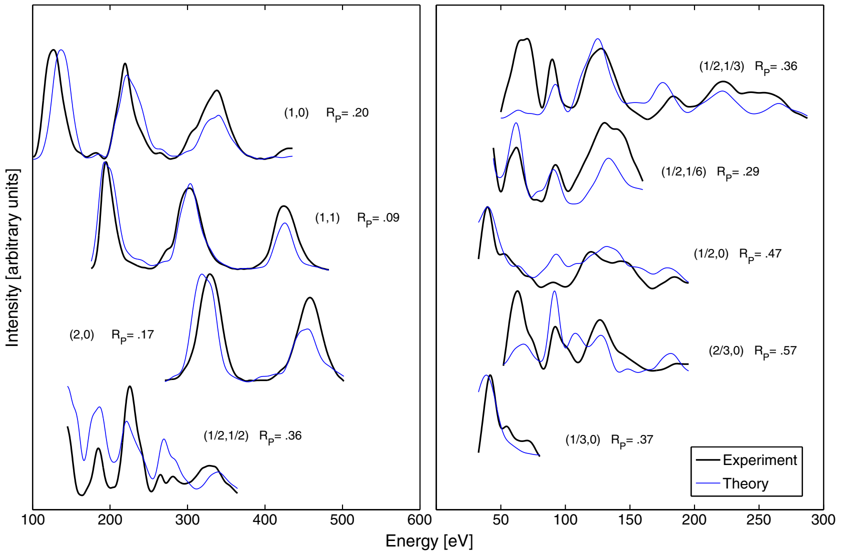

Fig. 2. I(V) curves for the favoured structure. The R-factors for the individual beams are shown in the figure. The overall Pendry R-factor is 0.28. Thick and thin lines correspond to experiment and theory respectively.

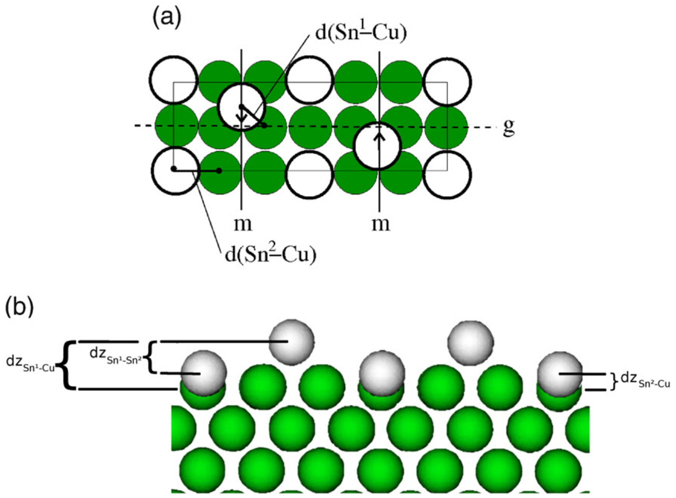

Fig. 3. Top (a) and side (b) views of the favoured structure. The colour coding of the atoms is the same as in Fig. 1. In the top view the unit cell and mirror (m) and glide (g) planes are shown. In the side view the atom radius is reduced for clarity. The arrows in (a) indicate the direction to which the Sn atoms are moved from the high symmetry hollow sites. The geometrical parameters shown in (a) and (b) are listed in Table 3.

atoms are buckled by 0.59/0.45 ± 0.2 Å (DFT/LEED) above the centre off mass of the first layer copper atoms. The overlayer tin atoms are 1.93/1.80 ± 0.2 Å (DFT/LEED) above the centre of mass of the first copper layer and the vertical distance between the Sn atoms in the overlayer and alloyed layer is 1.33/1.35 ± 0.3 Å(DFT/LEED). The nearest neighbour Cu—Sn distance between the overlayer tin and the first layer copper is 2.65/2.59 ± 0.2 Å (DFT/LEED), which gives effective radius of 1.37/1.31 Å (DFT/LEED) for tin. This effective radius is 4/7% (DFT/LEED) smaller than the Sn radius calculated from the Sn—Sn nearest neighbour distance in bulk Sn (1.405 Å). The interlayer spacings remain very close to the bulk Cu{100} values. The lateral distance off the hollow site for the overlayer Sn atoms is 0.02/0.13 ± 0.3 Å (DFT/LEED).

The structure found in this study is similar to the 0.65 ML Sn/Cu structure; Cu{100}-c(4 × 4)-Sn, where one Sn atom is alloyed into the first Cu layer and four Sn atoms are adsorbed as adatoms. The Sn adatoms are displaced from the fourfold hollow sites by 0.30 ± 0.06 Å and the alloyed Sn is buckled up by 0.33 Å with respect to the first layer copper. The effective radius for tin found in this study is 1.33 Å meaning 5% contraction compared to bulk Sn [14]. The buckling of the alloyed layer Sn in this p(2 × 6)-2mg-Sn system is considerably larger than the buckling found in c(4 × 4)-Sn system [14]. This difference can be explained by the fact that the density of alloyed Sn atoms is higher in this structure (1 alloyed Sn per c(4 × 4) unit cell vs. 2 alloyed Sn per p(2 × 6) unit cell). Because of this the strain in the alloyed layer must be larger in the p(2 × 6) unit cell causing this larger buckling. In the Cu{100}-p($3\sqrt{2} \times \sqrt{2}$)R45°-Sn system the Sn coverage is 0.5 ML and all the Sn atoms are alloyed into the first copper layer. In this system the stress in the first layer is relieved both by buckling of the Sn atoms (0.39/0.27 ± 0.07 Å above the centre of mass of the first copper layer) and by a missing row reconstruction [6,13]. In the LEED I(E) analysis of the p($3\sqrt{2} \times \sqrt{2}$)R45° phase the effective radius for tin is calculated to be 1.31 Å [6] which means contraction of 7% compared to bulk Sn. This effective radius is exactly the same as found in our LEED I(E) analysis.

Substitutional surface alloy formation on Cu{100} has also been reported for elements that are near Sn in the periodic table (In, Sb, Pb and Bi). In the Cu{100}-p(2 × 2)-Sb system, a surface alloy is formed at

Table 2
Pendry R-factors for the models shown in Fig. **1**.

Model	Pendry R-factor stage 1	Pendry R-factor stage 2
(a)	0.65	
(b)	0.63	
(c)	0.68	
(d)	0.48	0.28
(e)	0.56	
Pendry variance [28]	0.06	

Table 3
Geometrical parameters extracted from DFT and LEED analysis. d(Sn—Cu) is the nearest neighbour bond length between the Sn and the Cu, Sn^1 is the overlayer Sn, Sn^2 is the Sn alloyed into the first copper layer, Cu^1 is the first layer copper, Cu^{bulk} is the copper in deeper layers, r(Sn) is the effective radius for tin, $\Delta_{offhollow}$ is the lateral distance off the hollow site for Sn^1 (see Fig. 3(a)), dz_{Sn-Cu} is the vertical distance between the Sn atom and the centre of mass of the first Cu layer, $\Delta_i^{average}$ is the average amplitude of buckling of copper atoms in i^{th} layer, $dz_{ij}^{average}$ is the interlayer spacing between the centres of mass of the copper atoms in the i^{th} and j^{th} layer, Θ_D is the Debye temperature, V_I is the imaginary part of the inner potential, ΔE is the cumulative energy range in LEED calculation, T_{exp} is the temperature where the LEED data is measured and l_{max} is the maximum l value used in the analysis. Some of the parameters listed here are shown in Fig. 3(a) and (b).

Structural parameter	DFT	LEED	Non-structural parameter	LEED
$d(\mathrm{Sn}^1_?—\mathrm{Cu})$ [Å]	2.66	2.59 ± 0.20		
$d(\mathrm{Sn}^2_?—\mathrm{Cu})$ [Å]	2.65	2.59 ± 0.20	l_{max}	11
r(Sn)[Å]	1.37	1.31	V_I [eV]	−7
$\Delta_{offhollow}$	0.02	0.13 ± 0.30		
$dz_{Sn^1-Sn}{}^2$ [Å]	1.33	1.35 ± 0.30	$\Theta_D(Sn^1)$ [K]	80
dz_{Sn^1-Cu} [Å]	1.93	1.80 ± 0.20	$\Theta_D(Sn^2)$ [K]	120
dz_{Sn^2-Cu} [Å]	0.59	0.45 ± 0.20	$\Theta_D(Cu^1)$ [K]	240
$\Delta_1^{average}$ [Å]	0.00	0.07 ± 0.10	$\Theta_D(Cu^{bulk})$ [K]	343
$\Delta_2^{average}$ [Å]	0.00	0.01 ± 0.12	ΔE [eV]	2100
$\Delta_3^{average}$ [Å]	0.01	0.01 ± 0.20	T_{exp} [K]	300
$\Delta_4^{average}$ [Å]	0.00	0.04 ± 0.20		
$\Delta_5^{average}$ [Å]	0.00	0.06 ± 0.13		
$dz_{12}^{average}$ [%]	−1	+3 ± 6		
$dz_{23}^{average}$ [%]	+1	0 ± 9		
$dz_{34}^{average}$ [%]	+1	0 ± 11		
$dz_{45}^{average}$ [%]	+1	+1 ± 9		
$dz_{56}^{average}$ [%]	−2	+2 ± 7		
dz_{Bulk} [Å]	1.82	1.81		

an antimony coverage of 0.25 ML. The buckling between Sb and Cu atoms is of magnitude 0.56 ± 0.05 Å [28]. Similarly in the Cu{100}-p(2×2)-Bi system, a semi-ordered surface alloy is formed at the coverage of 0.25 ML. Buckling between Bi and the centre of mass of the first layer Cu atoms is of magnitude 0.56 ± 0.06 Å [29]. In the case of Cu{100}-c(4×4)-Pb, surface alloy is formed at a coverage of 0.375 ML [30]. In this case the lead atoms are buckled by 0.65 Å above the first layer Cu. The effective radii for Sb, Bi and Pb in these systems are 1.33 Å, 1.36 Å and 1.51 Å, respectively. These values compare well with our result, since Sb/Bi/Pb radius calculated from Sb—Sb/Bi—Bi/Pb—Pb distance in bulk is 3%/10%/24% larger than the corresponding radius for Sn. For low coverages (≈0.2 ML) of indium on Cu{100} a surface alloy is formed [31]. At that coverage a nearest neighbour Cu—In separation of 2.59 Å has been determined, which implies effective radius of 1.31 Å for indium [31].

5. Conclusions

In this paper we have studied the structure of Cu{100}-p(2×6)-2mg-Sn. In addition to the previously suggested model structures [10] we have introduced one additional model structure which turned out to be favoured by both LEED I(E) analysis and DFT calculations. The moderate level of agreement reached in the LEED I(E) analysis (Pendry R-factor of 0.28) could be partly explained by the fact that the p(2×6) phase is often in coexistence with the c(4×8) phase [10] which might have an effect on the I(E) data.

Acknowledgements

M. Lahti and K. Pussi would like to thank National Graduate School in Materials Physics and Academy of Finland for funding (grant numbers 130818, 218186 and 218546), and CSC—IT Center for Sciences Ltd, for computational resources. A. Cafolla acknowledged funding from the Irish Higher Education Authority PRTLI programme and from Science Foundation Ireland through the Research Frontiers Programme (grant number 06/RFP/PHY082).

Appendix A. Supplementary data

Supplementary data to this article can be found online at doi:10.1016/j.susc.2011.02.021.

References

[1] C.T. Campbell, Annu. Rev. Phys. Chem. 41 (1990) 775.
[2] G.A. Somorjai, Chem. Rev. 96 (1996) 1223.
[3] C. Argile, G.E. Rhead, Thin Solid Films 87 (1982) 265.
[4] E. McLoughlin, A.A. Cafolla, E. AlShamaileh, C.J. Barnes, Surf. Sci. 482 (2001) 1431.
[5] A.A. Cafolla, E. McLoughlin, E. AlShamaileh, Ph. Guaino, G. Sheerin, D. Carty, T. McEvoy, C. Barnes, V. Dhanak, A. Santoni, Surf. Sci. 544 (2003) 121.
[6] K. Pussi, E. AlShamaileh, E. McLoughlin, A.A. Cafolla, M. Lindroos, Surf. Sci. 549 (2004) 24.
[7] J. Martínez-Blanco, V. Joco, H. Ascolani, A. Tejeda, C. Quirós, G. Panaccione, T. Balasubramanian, P. Segovia, E.G. Michel, Phys. Rev. B 72 (2005) 041401.
[8] J. Martínez-Blanco, V. Joco, P. Segovia, T. Balasubramanian, E.G. Michel, Appl. Surf. Sci. 252 (2006) 5331.
[9] Y. Nara, K. Yaji, T. Iimori, K. Nakatsuji, F. Komori, Surf. Sci. 601 (2007) 5170.
[10] J. Lallo, L.V. Goncharova, B.J. Hinch, S. Rangan, R.A. Bartynski, D.R. Strongin, Surf. Sci. 602 (2008) 2348.
[11] K. Yaji, R. Nakayama, K. Nakatsuji, T. Iimori, F. Komori, Surf. Sci. 603 (2009) 341.
[12] J. Martínez-Blanco, V. Joco, C. Quirós, P. Segovia, E.G. Michel, J. Phys. Condens. Matter 21 (2009) 134001.
[13] J.D. Fuhr, J.E. Gayone, J. Martínez-Blanco, E.G. Michel, H. Ascolani, Phys. Rev. B 80 (2009) 115410.
[14] Hisashi Yoshida, Akinori Okamoto, Seigi Mizuno, Hiroshi Tochihara, Surf. Sci. 604 (2010) 535.
[15] F. Jona, Surf. Sci. 192 (1987) 398, and references therein.
[16] G.E. Rhead, C. Argile, M.-G. Barthes, Surf. Interface Anal. 3 (1981) 165.
[17] G. Argile, G.E. Rhead, Surf. Sci. 135 (1983) 18.
[18] G. Kresse, J. Hafner, J. Phys. Condens. Matter 6 (1994) 8245.
[19] G. Kresse, J. Furthmüller, Comput. Mater. Sci. 6 (1996) 15.
[20] G. Kresse, J. Furthmüller, Phys. Rev. B 54 (1996) 11169.
[21] G. Kresse, J. Joubert, Phys. Rev. B 59 (1999) 1758.
[22] P.E. Blöchl, Phys. Rev. B 50 (1994) 17953.
[23] J.P. Perdew, Y. Wang, Phys. Rev. B 45 (1992) 13244.
[24] H.J. Monkhorst, J.D. Pack, Phys. Rev. B 13 (1976) 5188.
[25] M.A. Van Hove, W. Moritz, H. Over, P.J. Rous, A. Wander, A. Barbieri, N. Materer, U. Starke, G.A. Somorjai, Surf. Sci. Rep. 19 (1993) 191.
[26] A. Barbieri and M.A. Van Hove, private communication.
[27] J.B. Pendry, J. Phys. C Solid State Phys. 13 (1980) 937.
[28] K. Pussi, E. AlShamaileh, A.A. Cafolla, M. Lindroos, Surf. Sci. 583 (2–3) (2005) 151.
[29] E. AlShamaileh, C. Barnes, Phys. Chem. Chem. Phys. 4 (2002) 5148.
[30] Y. Gauthier, W. Moritz, W. Hosler, Surf. Sci. 345 (1996) 53.
[31] C.J. Barnes, in: D.P. Woodruff (Ed.), Surface Alloys and Alloy Surfaces (The Chemical Physics of Solid Surfaces), 10, Elsevier, Amsterdam, 2002.

ACTA UNIVERSITATIS LAPPEENRANTAENSIS

398. WANDERA, CATHERINE. Performance of high power fiber laser cutting of thick-section steel and medium-section aluminium. 2010. Diss.

399. ALATALO, HANNU. Supersaturation-controlled crystallization. 2010. Diss.

400. RUNGI, MAIT. Management of interdependency in project portfolio management. 2010. Diss.

401. PITKÄNEN, HEIKKI. First principles modeling of metallic alloys and alloy surfaces. 2010. Diss.

402. VAHTERISTO, KARI. Kinetic modeling of mechanisms of industrially important organic reactions in gas and liquid phase. 2010. Diss.

403. LAAKKONEN, TOMMI. Distributed control architecture of power electronics building-block-based frequency converters. 2010. Diss.

404. PELTONIEMI, PASI. Phase voltage control and filtering in a converter-fed single-phase customer-end system of the LVDC distribution network. 2010. Diss.

405. TANSKANEN, ANNA. Analysis of electricity distribution network operation business models and capitalization of control room functions with DMS. 2010. Diss.

406. PIIRAINEN, KALLE A. IDEAS for strategic technology management: Design of an electronically mediated scenario process. 2010. Diss.

407. JOKINEN, MARKKU. Centralized motion control of a linear tooth belt drive: Analysis of the performance and limitations. 2010. Diss.

408. KÄMÄRI, VESA. Kumppanuusohjelman strateginen johtaminen – Monitapaustutkimus puolustushallinnossa. 2010. Diss.

409. KARJALAINEN, AHTI. Online ultrasound measurements of membrane compaction. 2010. Diss.

410. LOHTANDER, MIKA. On the development of object functions and restrictions for shapes made with a turret punch press. 2010. Diss.

411. SIHVO, VILLE. Insulated system in an integrated motor compressor. 2010. Diss.

412. SADOVNIKOV, ALBERT. Computational evaluation of print unevenness according to human vision. 2010. Diss.

413. SJÖGREN, HELENA. Osingonjakopäätökset pienissä osakeyhtiöissä. Empiirinen tutkimus osakeyhtiölain varojenjakosäännösten toteutumisesta. 2010. Diss.

414. KAUPPI, TOMI. Eye fundus image analysis for automatic detection of diabetic retinopathy. 2010. Diss.

415. ZAKHVALINSKII, VASILII. Magnetic and transport properties of $LaMnO_{3+\delta}$, $La_{1-x}Ca_xMnO_3$, $La_{1-x}Ca_xMn_{1-y}Fe_yO_3$ and $La_{1-x}Sr_xMn_{1-y}Fe_yO_3$. 2010. Diss.

416. HATAKKA, HENRY. Effect of hydrodynamics on modelling, monitoring and control of crystallization. 2010. Diss.

417. SAMPO, JOUNI. On convergence of transforms based on parabolic scaling. 2010. Diss.

418. TURKU. IRINA. Adsorptive removal of harmful organic compounds from aqueous solutions. 2010. Diss.

419. TOURUNEN, ANTTI. A study of combustion phenomena in circulating fluidized beds by developing and applying experimental and modeling methods for laboratory-scale reactors. 2010. Diss.

420. CHIPOFYA, VICTOR. Training system for conceptual design and evaluation for wastewater treatment. 2010. Diss.

421. KORTELAINEN, SAMULI. Analysis of the sources of sustained competitive advantage: System dynamic approach. 2011. Diss.

422. KALJUNEN, LEENA. Johtamisopit kuntaorganisaatiossa – diskursiivinen tutkimus sosiaali- ja terveystoimesta 1980-luvulta 2000-luvulle. 2011. Diss.

423. PEKKARINEN, SATU. Innovations of ageing and societal transition. Dynamics of change of the socio-technical regime of ageing. 2011. Diss.

424. JUNTTILA, VIRPI. Automated, adapted methods for forest inventory. 2011. Diss.

425. VIRTA, MAARIT. Knowledge sharing between generations in an organization – Retention of the old or building the new 2011. Diss.

426. KUITTINEN, HANNA. Analysis on firm innovation boundaries. 2011. Diss.

427. AHONEN, TERO. Monitoring of centrifugal pump operation by a frequency converter. 2011. Diss.

428. MARKELOV, DENIS. Dynamical and structural properties of dendrimer macromolecules. 2011. Diss.

429. HÄMÄLÄINEN, SANNA. The effect of institutional settings on accounting conservatism – empirical evidence from the Nordic countries and the transitional economies of Europe. 2011. Diss.

430. ALAOUTINEN, SATU. Enabling constructive alignment in programming instruction. 2011. Diss.

431. ÅMAN, RAFAEL. Methods and models for accelerating dynamic simulation of fluid power circuits. 2011. Diss.

432. IMMONEN, MIKA. Public-private partnerships: managing organizational change for acquiring value creative capabilities. 2011. Diss.

433. EDELMANN, JAN. Experiences in using a structured method in finding and defining new innovations: the strategic options approach. 2011. Diss.

434. KAH, PAUL. Usability of laser - arc hybrid welding processes in industrial applications. 2011. Diss.

435. OLANDER, HEIDI. Formal and informal mechanisms for knowledge protection and sharing. 2011. Diss.

436. MINAV, TATIANA. Electric drive based control and electric energy regeneration in a hydraulic system. 2011. Diss.

437. REPO, EVELIINA. EDTA- and DTPA-functionalized silica gel and chitosan adsorbents for the removal of heavy metals from aqueous solutions. 2011. Diss.

438. PODMETINA, DARIA. Innovation and internationalization in Russian companies: challenges and opportunities of open innovation and cooperation. 2011. Diss.

439. SAVITSKAYA, IRINA. Environmental influences on the adoption of open innovation: analysis of structural, institutional and cultural impacts. 2011. Diss.

440. BALANDIN, SERGEY, KOUCHERYAVY, YEVGENI, JÄPPINEN, PEKKA, eds. Selected Papers from FRUCT 8 .2011.